Application of Optical Fiber Sensors for Quenching Temperature Measurement

Paul R. Hurley

Thesis submitted to the Faculty of the

Virginia Polytechnic Institute and State University

in partial fulfillment of the requirements for the degree of

Master of Science

in

Nuclear Engineering

Juliana P. Duarte, Chair

Yang Liu

John Palmore Jr

May 8, 2020

Blacksburg, Virginia

Keywords: film boiling, two-phase flow, fiber optics, quenching

Application of Optical Fiber Sensors for Quenching Temperature Measurement

Paul R. Hurley

(ABSTRACT)

The critical heat flux (CHF) point for a reactor core system is one of the most important factors to discuss in regards to reactor safety. If this point is reached, standard coolant systems are not enough to handle the temperature increase in the cladding, and the likelihood of meltdown greatly increases. While the nucleate boiling and film boiling regimes have been well-investigated, the transition boiling regime between the point of departure from nucleate boiling (DNB) and the minimum film boiling temperature (T_{min}) remains difficult to study. This is due to both the complexity of the phenomena, as well as limitations in measurement, where experiments typically utilize thermocouples for temperature data acquisition. As a result of technological advancement in the field of fiber optics, it is possible to measure the quenching temperature to a much higher degree of precision. Optical fiber sensors are capable of taking many more measurements along a fuel simulator length than thermocouples, which are restricted to discrete points. In this way, optical fibers can act as an almost continuous sensor, calculating data at a resolution of less than one millimeter where a thermocouple would only be able to measure at one point. In this thesis, the results of a series of quenching experiments performed on stainless steel, Monel k500, and Inconel 600 rods at atmospheric pressure, with different subcooling levels and surface roughnesses, will be discussed. The rewetting temperature measurement is performed to compare results between thermocouples and optical fiber sensors in a 30 cm rod. These results are further discussed with regard to future application in two-phase flow experiments.

Application of Optical Fiber Sensors for Quenching Temperature Measurement

Paul R. Hurley

(GENERAL AUDIENCE ABSTRACT)

There are multiple types of boiling that can occur depending on the heat transfer capabilities of the system and the power applied to the coolant. The most common is nucleate boiling, where vapor produced at the surface forms bubbles and move away from the surface due to buoyancy. At a high enough power, the bubbles can coalesce into a film and lead to a point at which the liquid coolant can no longer contact the surface. Since vapor is not as effective at transferring heat from the surface, the temperature will increase drastically. In nuclear reactors, this situation (known as departure from nucleate boiling), can quickly lead to a meltdown of the fuel rods. Another important safety parameter in nuclear reactors is the minimum temperature at which this vapor film can be maintained, $T_{\min}$. This parameter is a source of significant concern with regard to accident scenarios such as LOCA (loss of coolant accident), where reintroducing coolant to the rods efficiently is of top priority. While much research has been done on nucleate and film boiling, it has been difficult to study the transition period between the two regimes due to both its transient nature and the lack of continuous measurement capabilities. Typically, temperature is measured using thermocouples, which are point-source sensors that do not allow for high spatial resolution over a large area. This thesis deals with the utilization of optical fibers for temperature measurement, which are capable of calculating data at every millimeter, potentially a much more precise measurement system than with the thermocouples. The experiments performed in this paper are quenching experiments, where a rod embedded with thermocouples and an optical fiber is heated to well above T_{min} and quickly plunged into a volume of water, in order to view the transition from film to nucleate boiling.

Acknowledgments

I would like to first thank my advisor and mentor throughout my graduate studies, Professor Juliana Duarte. Her guidance and support have helped me to better realize my potential academically, and she has always been willing to put in the effort to assist me with any problems I might be having, while still allowing this paper to be my own work. I would like to thank Jeric Demasana, who assisted me in the lab with both experimental setup as well as data acquisition. Finally, I must express my profound gratitude to my parents and friends for providing me with unfailing support and encouragement. This accomplishment would not have been possible without them. Thank you.

Contents

List of Figures

List of Tables

List of Abbreviations

α	Thermal Diffusivity
ρ	Density
c_p	Specific Heat
k	Thermal Conductivity
q''	Heat Flux
T	Temperature
T_Q	Quenching Temperature
T_{min} , T_{MFB}	Minimum Film Boiling Temperature
T_{sat}	Saturation temperature
T_{wall}	Wall Temperature
x	Quality
ATF	Accident-Tolerant Fuel
BN	Boron Nitride
BWR	Boiling Water Reactor
C-OFDR	Coherent Optical Frequency Domain Reflectometry
CHF	Critical Heat Flux

DUT Device Under Test

LOCA Loss of Coolant Accident

LWR Light Water Reactor

OFDR Optical Frequency Domain Reflectometry

OTDR Optical Time Domain Reflectometry

PTFE Polytetrafluoroethylene

PWR Pressurized Water Reactor

SEM Scanning Electron Microscopy

SS Stainless Steel

Zr Zirconium

Chapter 1

Introduction

Before going through the experimental details, it is important to understand the reasons for studying quenching phenomena as well as the mechanisms by which the experiment intends to better understand them.

In the pressure vessels of pressurized water reactors (PWRs), convective heat transfer pulls heat energy from the reactor core (which produces said energy via fission of uranium-235) into the liquid water coolant surrounding it. This heated water is then used to heat a separate water channel to produce steam, which in turn is used to power the turbines outside the reactor. Thus, it is necessary for PWRs to have two separate water loops at different pressures to allow for steam generation without carrying excess radiation with it. In boiling water reactors (BWRs), there is only one coolant loop that produces vapor on contact with the core, which allows for greater simplicity at the cost of irradiating the turbine system. In both cases, boiling will occur at the core (subcooled boiling in the case of PWRs), so a key feature in reactor safety is maintaining this vapor production so as not to reach the point where the vapor keeps the liquid coolant from reaching the surface. When controlling the heat flux to a system, as in the case with a reactor core, the point at which this starts to take place is called the critical heat flux (CHF).

In nuclear reactors, the way that power is moderated is by using control rods to maintain a critical level of fission, which controls the heat flux through the surface of the rods. The temperature itself cannot be controlled, but it can be measured in an experimental laboratory

in order to determine how close to the CHF limit the system is at any point in time. Typical measurement in simulated conditions uses thermocouples to measure the rod temperatures. However, this can potentially be an issue if more active boiling occurs, since the void fraction along the rods will be changing dramatically. In order to deal with this, the use of optical fibers, which is able to make almost continuous measurements, has been brought up (Hurley and Duarte (2019)). The physics behind this will be discussed later on in the introduction.

1.1 Boiling Regimes and the Boiling Curve

Shiro Nukiyama (1934) was the first to develop a general plot of the different boiling regimes and how they relate to each other. As seen in Fig. 1.1, the heat transfer regimes follow a curve, which has commonly been called the Nukiyama pool boiling curve. At a subcooled state, where the bulk liquid temperature is less than the saturation temperature, the only heat transfer that occurs is in the form of single-phase natural convection. From this subcooled state, the heat flux increases to subcooled boiling at point A, then to saturated boiling at point B, until it finally reaches point C, regarded as the CHF value. At this point, the system will pass through a transient transition boiling regime and into a film boiling regime if it is temperature controlled. If, however, it is the power that is controlled, as in the case for reactor cores, then this causes the system to immediately transition into film boiling.

By following the boiling curve, one can see that this marks a transition from point C to C', and thus a large jump in wall temperature as the liquid is not longer able to pull heat directly out of the wall. After power to the heated surface is decreased and the temperature drops, it reaches the quenching temperature (marked D on the plot). After this point, the liquid will be able to make contact and stay in contact with the heated surface, rapidly decreasing the wall temperature and allowing the transition back into the nucleate boiling regime. By definition,

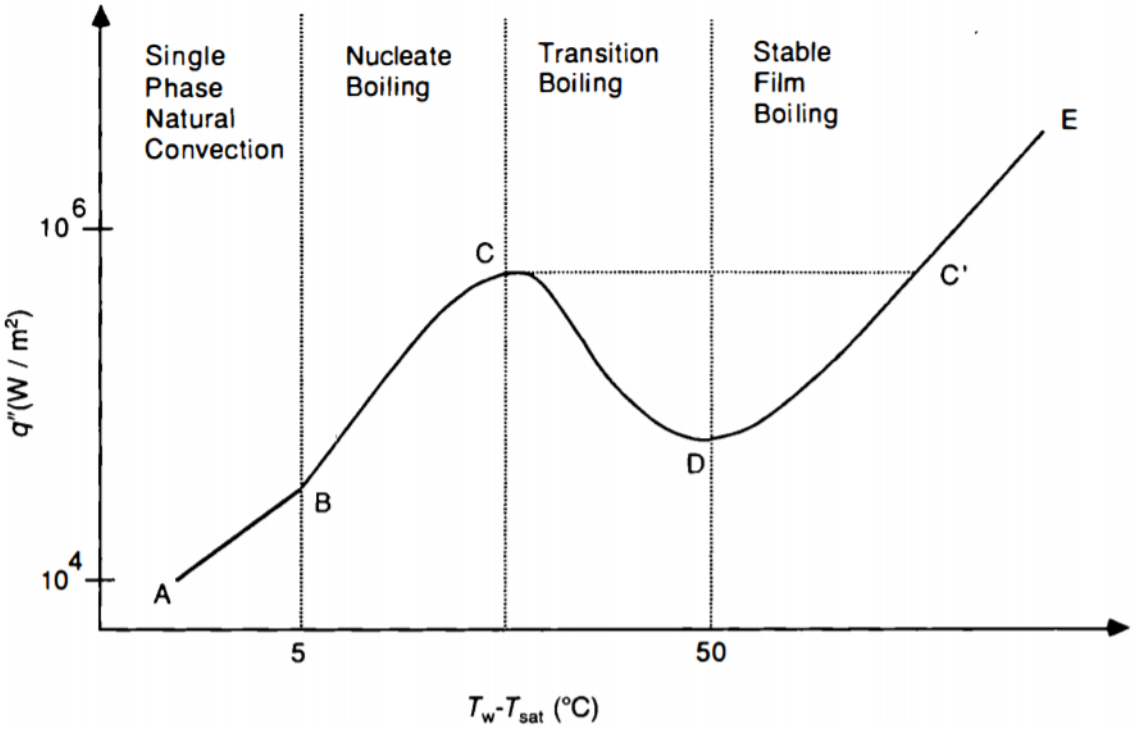

Figure 1.1: pool boiling curve, taken from *Nuclear Systems I* (Todreas and Kazimi 1990)

the minimum film boiling temperature (T_{min}) is the minimum temperature that this vapor film can be sustained, but it possible for the film to collapse at higher temperatures. In this case, the temperature at which this occurs would not be defined as T_{min}, but rather as the quenching temperature, or T_Q (Shumway 1985).

1.1.1 Nucleate Boiling

The first boiling regime that the system will undergo as the heat flux increases is subcooled nucleate boiling, where vapor produced at the wall nucleates into bubbles that leave the wall and eventually condense back to liquid form. This is the only type of boiling that occurs in routine PWR operation. After raising the heat flux, the bulk temperature of the coolant will reach the saturation point and bubbles can detach from the wall without collapsing. This

regime, known as saturated boiling, is what happens in BWRs. In this regime, there are not enough bubbles to coalesce into anything large enough to prevent liquid from contacting the wall. As the power is increased, more nucleation sites are activated, and the bubbles increase in size as well, where they can begin to coalesce into larger vapor bubbles.

1.1.2 Film Boiling

After reaching critical heat flux, the system will quickly reach a point where the liquid no longer contacts the surface due to the bubbles forming a single film of vapor. Since the heat transfer coefficient of vapor is much less than that of liquid, heat cannot be taken away from the core as quickly as in nucleate boiling. Therefore, the temperature of the wall will increase drastically in order to maintain the current heat flux. This can cause the rod temperatures to rise to well above 1000°C rapidly. To compare, the melting point of the Zircaloy cladding used in PWR fuel rods is around 1800°C. If film boiling begins to occurs on the surface of the fuel rods, then severe damage to the fuel is almost guaranteed.

1.1.3 Transition Boiling

The transition boiling regime is the transient regime between nucleate and film boiling. This regime is quite difficult to study due to its transient nature, as well as being unable to study using real reactor conditions since it requires the system to go past the CHF limit. Therefore, experimental findings under reactor-like conditions is the only way to study transition boiling. There are two main types of experiments used to study this regime: pool/flow boiling and quenching. Both require having the system go through all three primary boiling regimes, just in opposite directions. The beginning of the transition boiling regime is marked by the CHF point in the pool/flow boiling direction, and T_{min} in the quenching direction.

1.2 Optical Fiber Measurement Systems

Fiber optics are not a new technology, but the range of their application has been growing over the years. Application of optical fibers for stress measurements have recently been studied, with promising results, as demonstrated in Nixon (2019). Temperature measurement provides a similar benefit of having many more measurement points than standard instrumentation, though there are distinct hurdles to face, especially when testing using rod bundles. Since the radial location of the heat transfer cannot be determined when using a single fiber down the center of the test rod, testing with these fibers is most easily applicable on radially symmetric situations. In rod bundles, this is not necessarily going to be the case, and so more than one fiber would have to be used spaced in different radial locations of each rod (or, like in Nixon *et al.* (2019), the fibers could be wound around each rod and fitted into a light groove so that the location is maintained).

1.2.1 Optical Fiber Temperature Sensors and OFDR

Optical fibers can be used as measurement devices due to physical change in wavelength and phase that occurs due to variations in the temperature, strain, and pressure of the system. When light passes through the fibers, the light scatters due to minor variations along the fibers' length. This scattering, known as Raman scattering, changes depending on the lattice oscillations within the fiber (Ribeiro *et al.* (2008)). These oscillations become stronger as the temperature of the fibers changes. Therefore, changes in temperature are able to alter the physical characteristics of the fibers locally, thus altering the wavelength of the light passing through the fibers. By fitting this spectral shift to the temperature change in the system, the fibers can be used as continuous linear sensors.

The fibers are connected to a fiber optic interrogator system that translates the spectral

shift directly into a temperature change from nominal. The interrogator utilizes optical frequency domain reflectometry, or OFDR, which is described in detail in Yüksel *et al.* (2009). Coherent OFDR, or C-OFDR, is the specific method used by the optical fibers in these tests.

In C-OFDR, the probe signal, known as the frequency-modulated optical signal, is split into two parts. The first part is used as a reference signal, which reflects off of a mirror, whereas the second is used to probe the test system (called the DUT, or device under test). These two signals then return to the interrogator and coherently interfere, where the interference signal's beat frequencies are interpreted after a Fourier transform is done on the light-induced electrical current. This method allows for very high spatial resolution compared to other methods such as OTDR (optical time domain reflectometry), which suffers from "deadzones" where the interrogator is momentarily unable to detect the incoming light energy. The C-OFDR method is shown in Fig. 1.2.

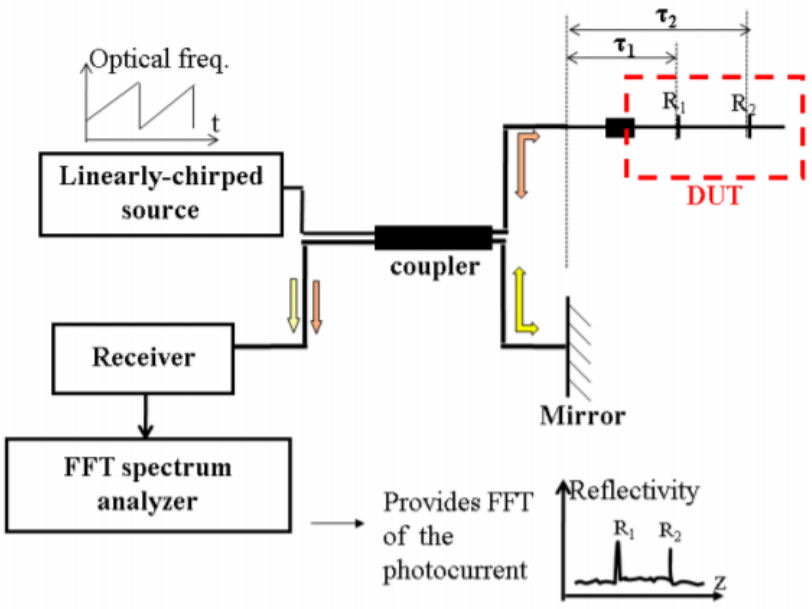

Figure 1.2: Coherent OFDR operation principle from Yuksel *et al.* (2009).

1.3 Brief Overview

This thesis covers a series of quenching experiments performed on 30 cm rods at atmospheric pressure under various liquid subcooling values and with varying degrees of surface roughness to determine their impact on the quenching temperature. The quenching temperature itself is measured in two ways: by using three standard thermocouples embedded in the rods, and by using optical fibers inserted into the rods to determine their effectiveness in recording the quenching temperature change axially. This thesis will first go through a review of the relevant literature needed to fully understand the current breadth of knowledge on this topic, and will then follow into a detailed outline of the experimental setup. The thesis will then discuss the results obtained by the data taken from the experiments, followed by data analysis and conclusions, where future work on this topic is discussed briefly. All data taken is given in multiple formats in the Appendices at the end of the thesis.

Chapter 2

Literature Review

Previous experimental work has been done with regards to the individual components involved in this work, namely the effects of subcooling, surface wettability, and cladding material on the minimum film boiling temperature as well as the utilization of optical fiber temperature sensors. Many of the papers discussed study T_{min} via quenching, where a fuel rod simulator heated well past the required temperature to be in the film boiling regime (typically in the range of 500°C) is immersed in a pool of subcooled water, where the vapor film collapse is observed and recorded. This method of studying T_{min} is not a novel approach, but the use of optical fibers as temperature sensors in such a setting has not yet been studied. To better understand the extent of our current knowledge, a breakdown of some of the more important experimental work over the past few decades is presented in this section. While this is not an intensive look at every work that has been put out into the academic and industrial breadth of study, it is enough to give an idea of the importance of the experimental efforts put forward in this thesis, as well as potential for future applications of optical fiber sensor technology.

2.1 Minimum Film Boiling Models

Over the past several decades, multiple physical models have been developed to try to understand post-CHF boiling regime properties and conditions. When it comes to quenching

application, it is necessary to look at all potentially relevant phenomena as well as experimental correlations in order to properly determine whether the predictive capabilities are in line with the physical qualities of the experiment (eg. dimensions, geometries, and so on). Quenching falls under the category of forced convection, wherein the coolant and the heated rod surface are moving opposite each other due to outside force such as a pump or gravity causing the rod to drop. According to R. A. Nelson (1982), this quenching location is influenced by what he terms as the "conductive-convective propagating quench front," meaning that the quenching of a given point is determined by both convective heat transfer as well as by the quenching front. Quenching at each point can be plotted along a roughly similar path, shown from point A to D in Fig. 2.1. As can be seen, this plot is similar to Nukiyama's plot in Fig. 1.1, but the difference between ΔT_{min} and ΔT_{CHF} is shown to decrease as the vapor quality of the coolant increases. Here, quality is defined to be the ratio of the mass of vapor to the mass of liquid in the system.

2.1.1 Hydrodynamic Instability Model

Berenson (1961) first proposed a model for the minimum film boiling temperature from a horizontal surface, developed using the idea of Taylor-Helmholtz instability, with the belief that it is this instability that causes the collapse of the vapor film. Using this, a model was formulated that is dependent on intrinsic properties of the system (shown in Eq. 2.1).

$$\Delta T_{min} = 0.127 \frac{\rho_{vf} \Delta h}{k_{vf}} \left[\frac{g(\rho_l - \rho_v)}{\rho_l + \rho_v} \right]^{2/3} \left[\frac{g\sigma}{g(\rho_l - \rho_v)} \right]^{1/2} \left[\frac{\mu_f}{g_0(\rho_l - \rho_v)} \right]^{1/3} \tag{2.1}$$

This model was then modified using experimental data by Henry (1974) to account for the effect of transient contacting of the liquid to the wall surface as well as microlayer evaporation (shown in Eq. 2.2). Here, ΔT_{Ber} is the original minimum film boiling temperature given by

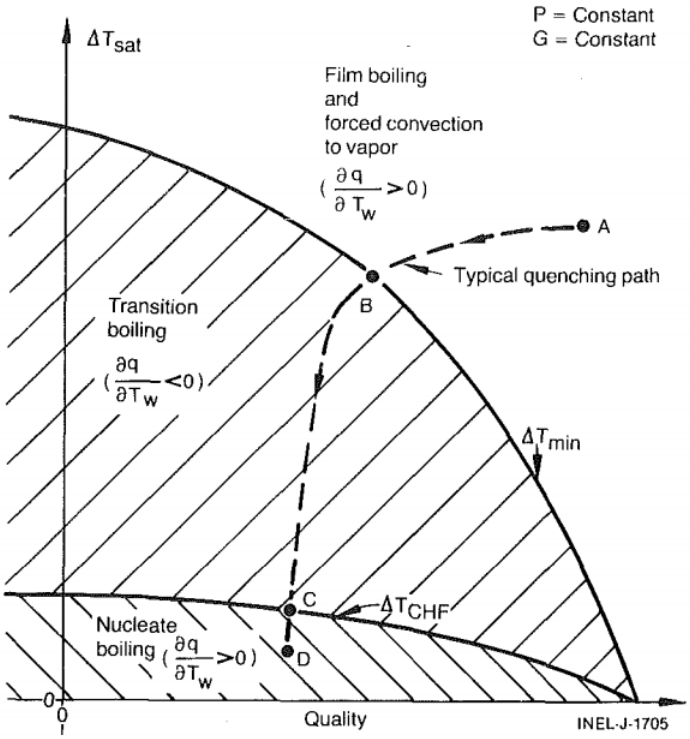

Figure 2.1: Plot of quality vs ΔT_{sat} showing typical quenching path from Nelson (1982).

Berenson.

$$\Delta T_{min} = \Delta T_{Ber} + 0.42(T_B - T_l) \cdot \left\{ \sqrt{\frac{(\rho k c_p)_l}{(\rho k c_p) w}} \left[\frac{h_{lv}}{c_{pw}(T_{Ber} - T_{sat}} \right] \right\}^{0.6} \tag{2.2}$$

2.1.2 Experimental Correlations on T_{min}

Most of the correlations that have been found to relate T_{min} to parameters such as subcooling, pressure, and surface wettability were developed from experimental data. Several of such correlations will be discussed here, as well as their individual range of application.

Three mechanisms that facilitate the controlled collapse of vapor film at T_{min}, impulse cooling collapse, axial conduction, and dispersed flow rewet, are described in Iloeje *et al.* (1972). Impulse cooling collapse states that while the vapor layer at any point in time will always

have a defined average thickness, the liquid/vapor interface is going to fluctuate around this average. If the vapor layer begins to decrease, for example if power to the heated surface was cut off, then eventually the fluctuating interface would be able to contact briefly with the surface, where it would immediately be pushed away due to vapor formation if the surface temperature is high enough above T_{min}. During quenching, this process would be repeated until the surface temperature lowers to the point that liquid contact with the wall will not be pushed away. The authors relate this to the equation correlated in Kalinin *et al.* (1969), which defines the quenching temperature directly to ratio between the liquid and wall thermal conductivities, densities, and specific heats (shown in Eq. 2.3).

$$\frac{T_{cr2} - T_{sat}}{T_c - T_L} = 1.65(0.16 + 2.4[(k\rho c)_L/(k\rho c)_w]^{0.25}) \tag{2.3}$$

In a system where a section has already been rewetted, axial conduction allows the quenching front to propagate downstream. The temperature at the traveling quench front is assumed by the authors to be equivalent to the wall temperature at T_{min}.

In dispersed flow rewet, heat transfer is broken down into two components: heat transfer of the vapor and heat transfer due to the droplets that are not touching the surface. This control mechanism is described in Fig. 2.2.

In Iloeje *et al.* (1975), a test loop was developed with components that allowed for steady-state and transient runs. The system was designed to facilitate forced convective heat transfer, with all tests being done at 6.89 MPa. The 10.16 cm long transient test section composed of Inconel with a 1.25 inner diameter (ID) and a 2.54 cm outer diameter (OD) was used to monitor vapor film collapse and rewetting once film boiling had been reached and the system's power had been shut off by measuring surface temperature from eight embedded thermocouples. From the data collected, a correlation was found that expanded upon

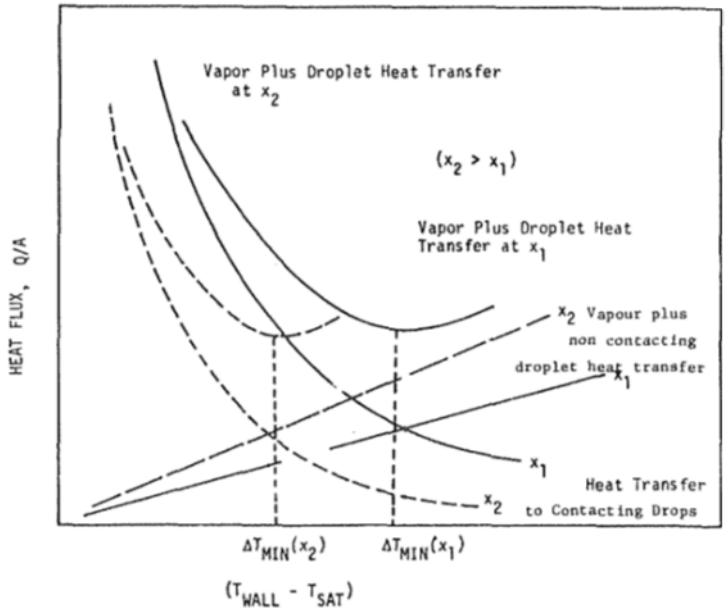

Figure 2.2: ΔT_{min} in the dispersed flow regime from Iloeje *et al.* (1972).

Berenson's model (seen in Eq. 2.4).

$$\Delta T_{min} = 0.29 \Delta T_{Ber}(1 - 0.295 X_E^{2.45})(1 + (G \times 10^{-4})^{0.49}) \tag{2.4}$$

The effect of axial conduction on the predicted values of ΔT_{min} is commented upon by the authors to be a significant factor, in addition to changes in wettability and other surface oxidation effects due to repeated testing. Due to the effect shown from axial conduction, the authors conclude that the collapse process cannot be described purely by $\rho k c_p$ ratio, as in Eq. 2.3. They also note that this effect would be the largest source of potential error in their own correlation, and that this error would depend on the quench front propagation speed.

Groeneveld and Stewart (1982) used the "hot patch technique" to allow film boiling to be maintained at heat flux levels below CHF. The test section where film boiling and collapse were to occur was composed of Inconel, with twenty thermocouples spot-welded to various

axial locations to measure temperature drop upon rewetting. The data collected from these tests were at pressures from 2000 to 9000 kPa, at qualities of -0.15 to 0.15, and with mass fluxes from 100 to 2700 kg/m^2·s. From this data, an empirical correlation was found that goes against Iloeje *et al.* (1975), due to the lack of dependence on mass flow (see Eq. 2.5).

$$T_{min} = \begin{cases} X \leq 0, P \leq 9000 \text{ kPa} & 284.7 + 0.0441P - 3.72 \times 10^{-6}P^2 - \frac{X \times 10^4}{2.82 + 0.00122P} \\ X > 0, P \leq 9000 \text{ kPa} & 284.7 + 0.0441P - 3.72 \times 10^{-6}P^2 \\ P > 9000 \text{ kPa} & (\Delta T_{min}, 9000 \text{ kPa}) \left(\frac{P_{crit} - P}{P_{crit} - 9000}\right) + T_{sat} \end{cases} \tag{2.5}$$

Shumway (1985) argues that T_{min} is actually a minimum value for the quenching temperature, which is defined by surface properties as well as the flow parameters. From this analysis, a new correlation was given (shown in Eq. 2.6).

$$T_Q = T_{sat} + 3.7 \frac{(\rho_l - \rho_v)}{\Delta\rho} \frac{h_{lv}\beta}{c_{pl}\text{Pr}_l} [1 + (1 - \alpha)^2](1 + 1.5 \times 10^{-5}\text{Re}_l)^{0.15} \left(1 - \frac{P}{P_{crit}}\right)^{0.1} \tag{2.6}$$

Here, T_Q is the quenching temperature and β is defined by Eq. 2.7. Note that β here is the transient contacting factor mentioned in Eq. 2.3.

$$\beta = \left[\frac{(k\rho c)_l}{(k\rho c)_w}\right]^{1/2} \tag{2.7}$$

2.2 Previous Quenching Experiments

Several experiments have been conducted by quenching fuel rod simulators under various conditions to determine their impact on temperature at which vapor film collapse occurs. Many of these experiments were performed in order to determine a more efficient method of transient heat transfer during fuel rod quenching, as in the cases of those experiments which studied accident-tolerant fuel (ATF) cladding materials. ATF is defined to be reactor fuel which is capable of handling significant design basis accidents, such as LOCA, by means such as more effective heat transfer capabilities or by being able to hold up to higher stresses. These experiments serve both as references and as bases for the framework of this experimental setup and procedure.

Ebrahim *et al.* (2016) performed quenching tests on a cylindrical stainless steel rodlet of similar diameter to both actual LWR fuel rods as well as the rods tested in this thesis (9.5 mm diameter). The rodlet had three thermocouples embedded inside at three axial locations, as shown in Fig. 2.3.

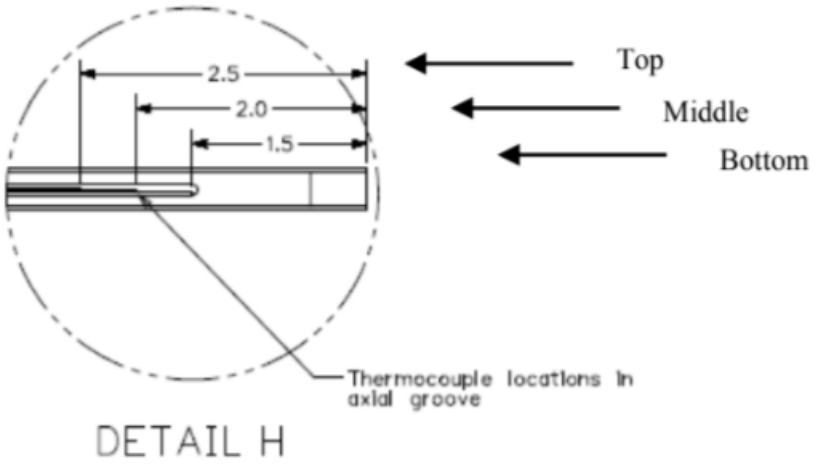

Figure 2.3: Thermocouple locations on test rodlet from Ebrahim *et al.* (2016).

The quenching experiments were performed at atmospheric pressure, and initial rod tem-

perature as well as liquid subcooling were varied to determine their effect on the quenching temperature. The range of these parameters was 2°C to 15°C subcooling, and 450°C to 650°C initial rod temperature. The results of these tests, as concluded by the authors, were that initial rod temperature has no significant effect on the temperature at which quenching occurs, whereas liquid subcooling temperature has an effect that can be defined by a correlation based on work done by Peterson and Bajorek (2002). This correlation is given in Eq. 2.8. Here, T^B_{min} is the predicted minimum film boiling temperature given by Berenson. Surface heat flux and temperature values were determined by utilizing the 1D inverse heat conduction code DATARH. This analysis is further described in Fudurich (2016).

$$T_{min} = T^B_{min} + 0.239(T^B_{min} - T_\infty)\left[\frac{k_f \rho_f c_f}{k_w \rho_w c_w}\right]^{0.25}\left[\frac{h_{fg}}{c_w(T^B_{min} - T_{sat})}\right]^{0.832} \tag{2.8}$$

Ebrahim *et al.* (2018) further experimented with various material properties to determine their effect on the quenching temperature. The authors, using the same experimental setup as in Ebrahim *et al.* (2016), tested rods composed of SS, zirconium (Zr), and Inconel-600 under atmospheric pressure at varying subcooling levels. The authors used various methods to characterize the surface properties, including surface roughness measurement, microscopic imagery, and water contact angle measurement.

Contact angle is defined to be the angle between the surface of the rod and the liquid/vapor interface, and is used to determine the wettability of a substance (shown in Fig. 2.4). Wettability is defined to be the ability of a liquid to maintain contact with a surface, and in this case, is inversely proportional to the contact angle. In allowing for the maximum rewetting temperature in a reactor core, high wettability is a primary goal. As in Ebrahim *et al.* (2016), a high-speed camera was used to record the quench front propagation speed. In this paper, the authors include another factor, $\rho k c_p$, a combination of the density, thermal

conductivity, and specific heat used to form the transient contacting factor mentioned in Eq. 2.7.

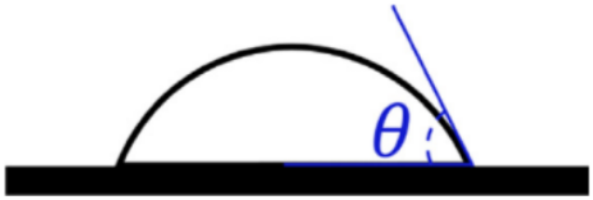

Figure 2.4: Water contact angle from Ebrahim *et al.* (2018).

From the results given in the paper, the authors concluded that as the liquid contact angle increases, the quenching temperature decreases. This follows logically from the idea that wettability decreases with increased contact angle. Additionally, the authors concluded that the effect of surface roughness on the quenching temperature could not be determined since the roughness values were of the same order of magnitude. Aligning with their previous paper (Ebrahim *et al.*, 2016), the authors concluded that an increase in the liquid subcooling (and thus a decrease in the liquid temperature) led to an increase in the quenching temperature.

Ebrahim *et al.* (2019) conducted tests using SS and Zr rods to determine the effect of surface conditions on the rods on the quenching temperature. Surface characteristics were determined via x-ray diffraction, scanning electron microscopy (SEM), and energy dispersive x-ray spectroscopy. Again, a high-speed camera was used to observe vapor film production and quench front propagation. Visual analysis of vapor film thickness was used to gauge heat transfer enhancement based on change in liquid subcooling. Based on the data found, the authors concluded that the Zr rod was much more susceptible to surface oxidation than the SS sample due to the noticeably higher quenching temperature measured from the oxidized Zr rod compared to the bare rod, whereas the oxidized SS sample had similar quenching results to the bare sample across all subcoolings tested. Additionally, the bare Zr rod was

determined to have a quenching temperature of between 30°C and 60°C higher than the SS rod depending on the liquid subcooling temperature. The authors also determined that a higher liquid subcooling resulted in a smaller vapor film thickness, which contributed highly to heat transfer enhancement and a higher quenching temperature.

Yeom *et al.* (2018) performed quenching experiments on Zircaloy-4 rods, testing under various pressures and liquid subcoolings, as well as testing for various surface roughnesses, made either by oxidation or by intentionally roughening the surface of the rod via grit blasting. SEM images of the bare, oxidized, and roughened surfaces, as well as their respective contact angle measurements, are given in Fig. 2.5. As seen in this figure, the oxidized surface has higher wettability than the bare rod, and the roughened surface has a higher wettability than both of the other surfaces. Experiments were conducted from atmospheric pressure to 0.5 MPa, and from saturation temperature to 15°C subcooled.

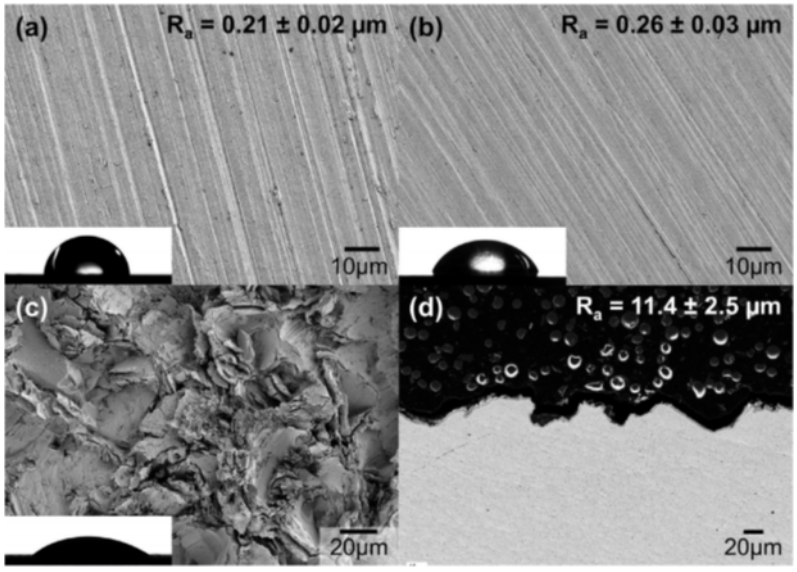

Figure 2.5: SEM images and contact angle images for (a) bare rods, (b) pre-oxidized rods, and (c) rods with a roughened surface from Yeom *et al.* (2018).

From the data collected, the authors determined that both the surface oxidation and the roughening allowed for enhanced quenching performance under all conditions tested. As

written by the authors, “vapor film dynamics were strongly affected by rough surfaces”, as indicated by the film behavior from experiments with the roughened rod being more violent than with the bare rod. The authors concluded that the results obtained suggest that surface properties as well as liquid-solid contact parameters are “dominant factors” in controlling transient heat transfer behavior during quenching.

In Seshadri and Shirvan (2018), candidate ATF cladding materials were studied to determine their heat transfer capabilities during quenching. The authors used 5 cm Zircaloy-4 rods with coatings of Chromium, FeCrAl, and Molybdenum, as well as bare Zirc-4 rods, both bare and with pre-oxidized surface layers, heated to 600°C and 1000°C. A single type K thermocouple was embedded in the center of the rods, and the boiling regimes during quenching were recorded using a high-speed camera. The results from these experiments indicated that among both the non-oxidized and oxidized coatings, FeCrAl showed the best heat transfer capabilities, having the highest quenching temperature. However, after oxidization, the Chromium coated rod was shown to have the highest percentage increase in quenching temperature, as well as the highest overall quenching front propagation speed, allowing the entirety of the rod to quench the fastest. Using SEM, the authors determined that the surface of the FeCrAl coated rod had the highest porosity, which they concluded was the primary cause of enhancing the nucleate boiling cooling rate via capillary wicking, as well as increasing what they determined to be the Leidenfrost temperature.

Kang *et al.* (2017) also studied the effect of various ATF candidate materials during quenching, testing FeCrAl as well as SiC-CVD compared to the commercially used Zirc-4 cladding. The authors also tested both the bare and oxidized surfaces to study heat transfer enhancement due to oxidization. As seen in Fig. 2.6, the Zircaloy rod was found to have the best heat transfer capabilities to allow it to quench at the highest temperature and with the fastest quenching speed, with both the Zircaloy and SiC-CVD rods gaining substantial

quenching enhancement after oxidization compared to FeCrAl. After studying the surfaces of these materials before and after oxidation and quenching, the authors concluded that this enhancement was due to the high porosity of the oxide layer formed on these two surfaces, as well as the formation of micro-scale pits and cracks that were formed after quenching in the SiC-CVD rod. The formation of these fissures and pits were believed to be caused by thermal shock fracture, which is defined in Lee *et al.* (2013). These two factors, the authors claim, cause the surface wettability of these materials to increase greatly, allowing for better heat transfer during quenching.

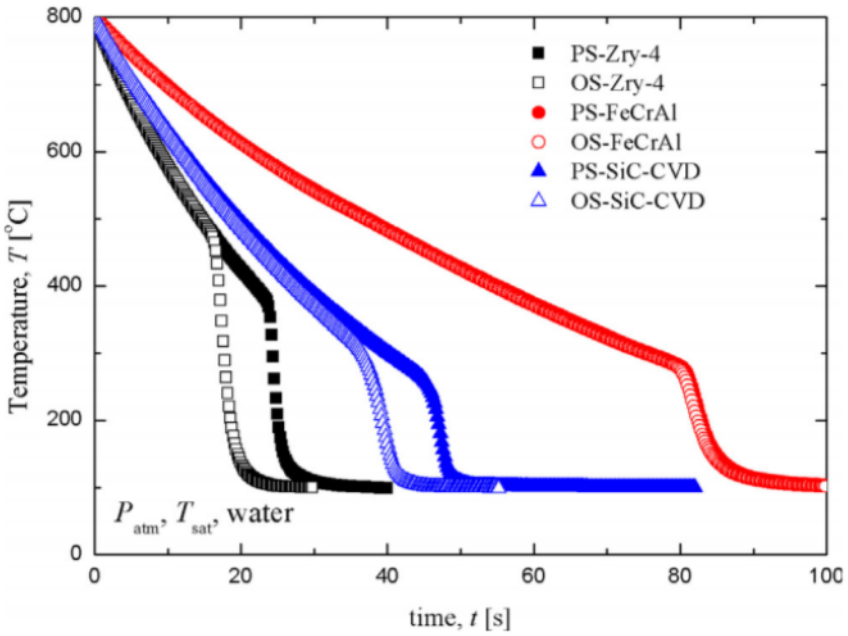

Figure 2.6: Quenching Plot for bare and oxidized Zirc-4, FeCrAl, and SiC-CVD rods from Kang *et al.* (2017).

Kang *et al.* (2019) expanded the previous experiment by studying the impact of subcooling, pressure, and flooding rate using both laboratory-scale testing on Zirc-4, FeCrAl, and SiC-CVD rods as well as calculations done using data from the FLECHT-SEASET 161 rod bundle experiment and the thermal hydraulic code MARS 3D-VESSEL. Fig. 2.7 shows a cross-sectional view of the FLECHT-SEASET experiment from which the data was taken.

The authors determined that a higher subcooling value contributed to greater quenching heat transfer capabilities in the form of increased quenching temperature as well as increased quenching speed. From the calculations done using MARS 3D-VESSEL, the authors determined that there was a direct relation between pressure and quenching temperature. They also found that an increased flooding rate led to a greatly decreased quenching time, and that a decreased liquid subcooling led to a decrease in the quenching rate (defined at dT/dt, not to be confused with quench front propagation speed). These conclusions, the authors remarked, need to be verified via a systematic study involving experimental quenching with flow before they can be confirmed.

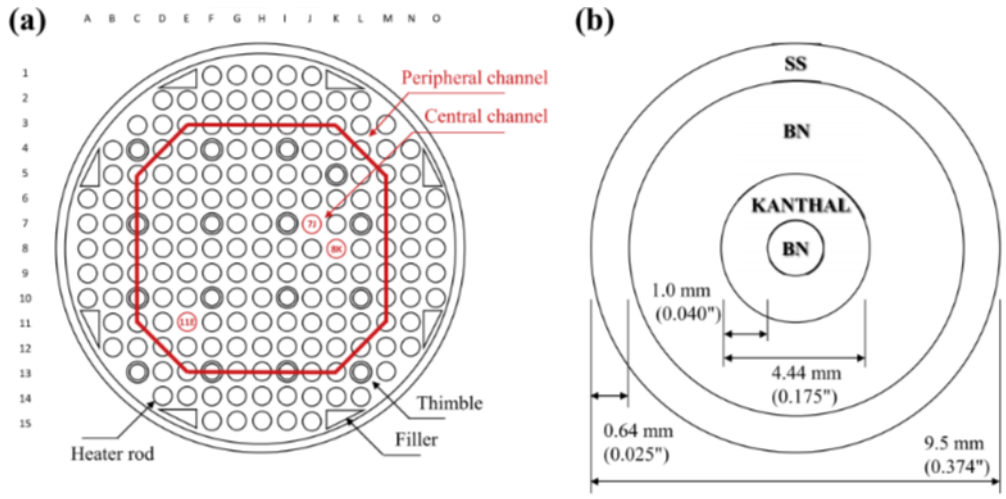

Figure 2.7: Cross-sectional view of (a) the entire 161 rod bundle and (b) a single heated rod from FLECHT-SEASET experiment, defined in Kang *et al.* (2019).

These quenching experiments have all shown various relations between liquid subcooling, pressure, material properties, and surface conditions and the quenching temperature. However, these experiments all used thermocouples to determine the quenching temperature, and many only used one measurement location to determine this temperature. In doing so, the authors neglected any potential axial conduction effect, which would be seen as a variation in quenching temperature depending on the measurement location axially. With the

utilization of optical fiber sensors, the axial conduction effect will be visible. Such measurement, if found to be accurate, would indicate the measured temperature of film collapse to be simply a quenching temperature rather than necessarily being the minimum film boiling temperature.

2.3 Optical Fiber Applications in Previous Works

Fiber optic sensors have been found to have an increasing utility in engineering application. In Wood, *et al.* (2014), the thermal capabilities for optical fibers were tested using two separate experiments. Temperature measurement was paired with spectral shift measurement for the fiber sensors, in order to determine the degradation point of the fibers. In the first, a non-coated fiber was placed in a furnace that was gradually brought up to 1000°C in steps of 200, 400, 600, 800, 900 and 1000°C. The furnace would be brought down to room temperature after every step. In the second experiment, two fibers, one bare and one with all but its innermost acrylate coating stripped, were placed in a furnace. The furnace was then brought up, in increments of 100°C from room temperature to 700°C, then in increments of 50°C to 800°C. The results of the first experiment showed that the fiber degraded past all usability after 800°C, approximately 33 hours into the experiment. The results of the second experiment showed that the spectral shift measurements for both fibers started to fail after 700°C, and failed entirely after 750°C.

Following along with the previous paper, in Weathered and Anderson (2015), several other factors were also tested in addition to the thermal limits of the optical fibers. Primarily, the integrities of polyimide and acrylate coatings were tested, as well as the use of helium instead of normal air surrounding the fiber. The acrylate and polyimide coatings had a temperature rating of 85°C and 300°C, respectively, which showed that neither would be of much use in

stopping the degradation of the fiber core past these temperatures. The polyimide coated fibers were also tested in air versus helium in order to test degradation in an inert gas. The results showed that, with a helium surrounding, the polyimide managed to survive in 450°C with little degradation, compared to over 60% degradation over 800 minutes in air. This showed that the backfilling of a capillary with inert gas is potentially viable to preventing the coating form degrading at higher temperatures.

Petrie and Blue (2015) further experimented with this idea, testing sapphire optical fibers in reactor settings (1000°C under gamma radiation). Using fibers of various wavelengths (650 nm, 850 nm, 1300 nm, and 1550 nm), it was shown that the slopes of added attenuation during irradiation at 600°C and 1000°C were lower than those at 59°C and 300°C. This, the authors claim, is in line with the idea that the formation of defects in the optical fibers can be reduced by annealing said point defects if the temperature is high enough. All increasing attenuation was found to have a linear slope. For the 650 nm fiber, it was found that the added attenuation of the irradiated fibers at 600 and 1000°C were consistent with the approximated attenuation at room temperature. This leads to the idea that the heating of the 650 nm fiber past 600°C caused a significant drop in the rate of added attenuation. For the 850, 1300, and 1550 nm fibers, added attenuation was limited by defect centers induced by the radiation, located in the ultra-violet to visible spectrum. Therefore, the added attenuation is less at 1300 and 1550 nm than at 850 nm, and is less at 850 nm than at 650 nm.

These experimental studies have shown the current testable range that these optical fibers are capable of operating before degradation prevents usability. Based off of these tests, it should be possible to conduct quenching experiments wherein heated rods are brought to above 500°C with optical fibers inserted without the fibers degrading. While these fibers have been shown to be brittle and can break easily if bent to too high an angle, an experimental setup

can be designed that minimizes the angle that the fibers need to bend at, thus minimizing the stress to the fibers. The experimental design in the following section is designed explicitly to reduce potential stresses to the optical fibers, while still allowing for the proper heating and quenching necessary.

Overall, the general understanding of T_{min}, as well as current voids in knowledge, can be well understood from these papers. While the effects of various substrate properties and system parameters (thermal properties, surface wettability, liquid subcooling, *etc.*) are well known and have been studied, the effect of axial conduction still provides a significant gap in the correlations given from the actual quenching temperature at a specific location. This effect can be better understood by using optical fiber temperature sensors to measure the quenching temperature at a much higher spatial resolution than before. In addition, the papers discussed in this section of the literature review indicate that optical fibers are capable of withstanding the various stresses that accompany quenching experimentation.

Chapter 3

Experimental Procedure

3.1 Design and Setup

The design of the experimental setup is fairly simple. A 30 cm rodlet with a cladding made of either stainless steel 304 (SS), Monel k500, or Inconel 600 is placed into a cylindrical ceramic heater where it is indirectly heated to over 500°C. The heater is wrapped with and on top of a layer of fiber insulation to minimize heat leakage. After the rod has become as uniform a temperature as possible inside the heater, it is then quenched using a pneumatic piston into a tank of deionized water. The water subcooling is maintained by an immersion heater prior to quenching, and a high-speed camera is set to record the film boiling and subsequent film collapse. Fig. 3.1 shows a 3D rendering of the setup, including the framework needed to keep the piston in place. In this figure, the heater has been made translucent to allow the rodlet to be seen. A layer of insulation is placed above the ceramic heater, with a space in the middle to allow the rod to pass through.

The rodlets are specially designed to be the same radial dimensions as standard PWR fuel rods. The rods are 30 cm long, with a diameter of 0.95 cm, and only the lower 20 cm are being measured during quenching. A cladding made of one of the three previously mentioned materials surrounds a layer of boron nitride (BN), which also surrounds a stainless steel hypodermic tube with a bore hole large enough to allow the optical fiber to fit inside the center. In addition, three thermocouples are placed under the cladding at different axial

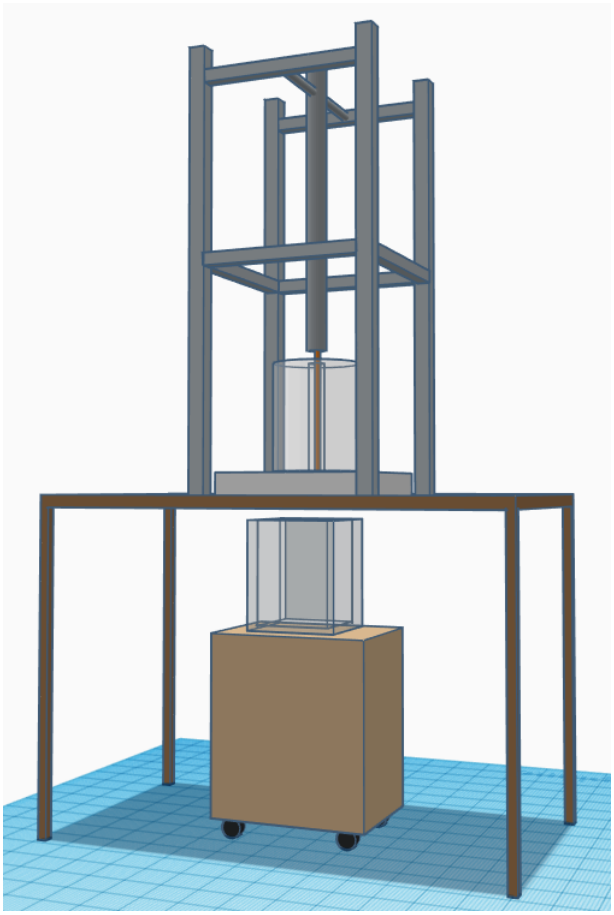

Figure 3.1: CAD rendering of quenching setup (to scale).

locations (5, 10, and 15 cm from the closed bottom of the rodlet). Fig. 3.2 shows the cross-section of the rods, with the location of each thermocouple and the bore hole where the optical fiber is inserted. While the rod is closed off at one end, the fiber is able to be placed within 2 mm of the bottom, so that precise measurement comparison can be made between the fiber and the thermocouples. The material properties of the rods are listed in Table 3.1. The properties for BN are taken from thermal properties given in TRACE, a thermal hydraulic code (*TRACE*). The properties for the remaining materials are taken from Special Metals (specialmetals.com).

In order to further compare with data from previous experiments, the surface roughnesses

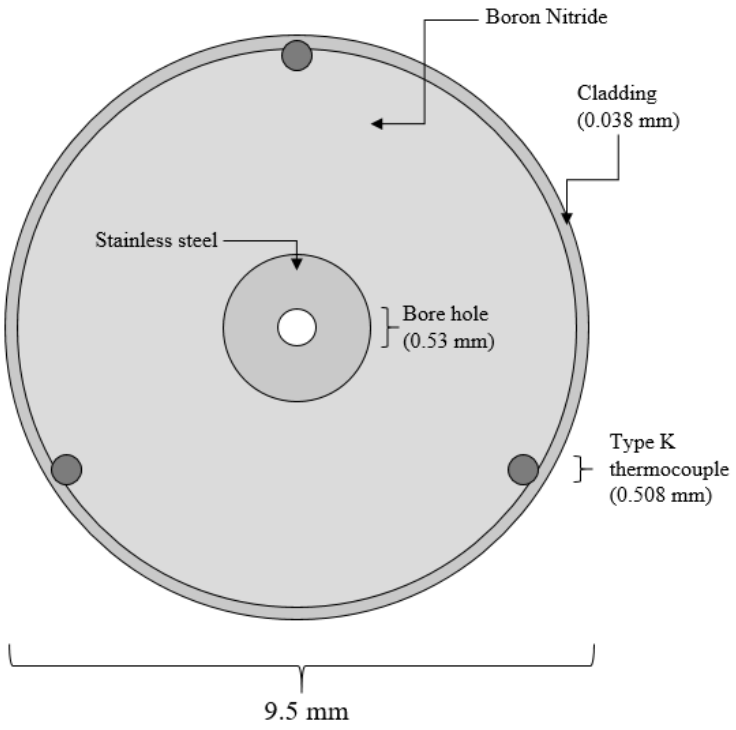

Figure 3.2: Blueprint of test rod cross-section (not to scale).

of each rodlet are taken before and after each quenching test. The roughness values, given in micrometers, are measured using a surface profilometer by taking three measurements at 5 cm from the bottom of the rod and averaging them. The rods are also quenched at various subcooling values, ranging from 2°C to 12°C, to determine its effect on the quenching temperature.

The optical fiber sensor system is composed of the fibers themselves, which are connected to an interrogator system. Both the interrogator and the optical fibers are provided by Luna Inc. The optical fibers are composed of a test length, a flexible lead, and a connector which connects to the port on the fiber interrogator. The test length is made up of a bare length of fiber with a silica sheath that allows the fiber to withstand temperatures up to 600°C. A strain relief connector holds the test length and the flexible lead together. The lead is composed of a standard fiber with a polytetrafluoroethylene (PTFE) coating, which

is not designed for high temperatures but is able to flex more than the test length. Fig. 3.3 shows these components and their dimensions. Note that due to the experimental setup, the test length of the fiber is needed to be much longer than the actual length of the rodlets, since during quenching an additional 40-50 cm of fiber must be able to withstand the high temperatures from the ceramic heater. The optical fiber interrogator, which is the ODiSI 6000 model, is capable of recording from up to 8 fiber sensors simultaneously.

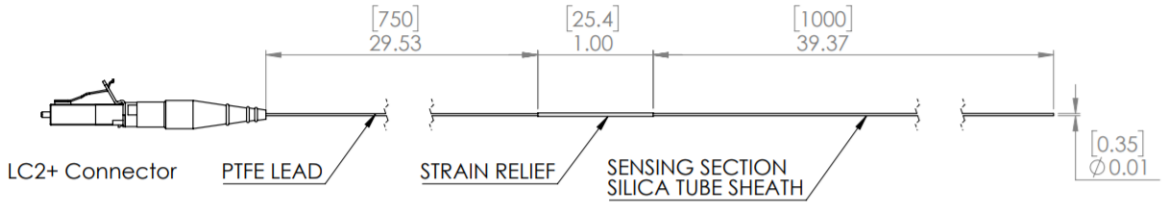

Figure 3.3: Optical fiber components and dimensions

3.2 Temperature Calibration for Fiber Measurements

While the thermocouple temperature data has well-known accuracy (with an error reported at ±0.4%) the initial optical fiber measurements require additional fine tuning. This is because the software that the fiber interrogator uses to convert spectral shift to temperature is scaled to a range of -20°C to approximately 200°C. Within this range, the spectral shift follows a linear relation to the temperature, and so a single coefficient (called the scaling factor) is used to convert between the two. Since the spectral shift does not change linearly with temperature outside of this range, measurements must first be converted back to spectral shift by dividing measurements by the scaling factor (given as -0.68 for this particular optical fiber interrogator), followed by scaling the spectral shift to a new function. For the purposes of this experiment, a fourth-order polynomial was required to allow for accuracy within 1°C of the thermocouple measurements (further error data provided in Analysis chapter). This

scaling function is given in Eq. 3.1, where T is the corrected temperature value, and s is the spectral shift.

$$T(s) = 24.00454 - 0.7938159s - 0.0005181s^2 - (4.70095\times10^{-7})s^3 - (1.84239\times10^{-10})s^4 \quad (3.1)$$

The coefficients for this polynomial are found by heating up a rod with a fiber inside to varying temperatures and allowing the rod to sit at each temperature until no increase was recorded. By comparing the measured fiber temperatures at the same axial locations as the thermocouples to the thermocouple temperature data, a curve fit can be produced from which the coefficients can be derived. The polynomial shown above uses data from all three thermocouples to maintain accuracy across as many axial locations as possible.

Material	T (°C)	k (W/cm°C)	c_p (J/kg°C)	ρ (kg/cm^3)
Boron Nitride	80.3	0.2503	900	2.002×10^{-3}
Boron Nitride	200.0	0.2473	1088	2.002×10^{-3}
Boron Nitride	400.0	0.2424	1350	2.002×10^{-3}
Boron Nitride	600.0	0.2375	1560	2.002×10^{-3}
Stainless Steel 304	80.3	0.1562	486	7.92×10^{-3}
Stainless Steel 304	200.0	0.1714	528	7.88×10^{-3}
Stainless Steel 304	400.0	0.1968	560	7.80×10^{-3}
Stainless Steel 304	600.0	0.2222	580	7.71×10^{-3}
Monel k500	93.3	0.1961	448	8.453×10^{-3}
Monel k500	204.4	0.2250	477	8.453×10^{-3}
Monel k500	426.7	0.2856	502	8.453×10^{-3}
Monel k500	648.9	0.3461	553	8.453×10^{-3}
Inconel 600	20.0	0.149	444	8.47×10^{-3}
Inconel 600	200.0	0.173	486	8.47×10^{-3}
Inconel 600	400.0	0.205	519	8.47×10^{-3}
Inconel 600	600.0	0.239	578	8.47×10^{-3}

Table 3.1: Thermal properties and densities of rod materials

3.3 Inverse Heat Transfer Analysis – INTEMP

In order to determine the effect of axial heat conduction in the rod, the surface heat fluxes need to be analyzed. Normally, heat transfer problems involve being given known heat flux values in a region, and solving for the temperature over time. Such a problem is typically solved using the heat conduction equation (given in Eq. 3.2). The inverse heat transfer problem, where known temperature data is given within the region of interest and the unknown heat fluxes are to be calculated, is the opposite situation. This problem is defined to be ill-posed, since the solution to this problem is not stable under small perturbations in the temperature data given. As is the case in any real-world data measurement, the temperature data taken is bound to have uncertainties and minor fluctuations in data. As a result, any analysis done to solve these problems typically involve the inclusion of some form of smoothing parameter to account for any perturbations in the data deemed minute enough to be measurement error.

$$k\nabla^2 T + q''' = \rho c_p \frac{dT}{dt} \tag{3.2}$$

To conduct this analysis, the inverse heat transfer software INTEMP was used (Trujillo 2003). Inverse heat transfer is the method of determining, from known temperature data and boundary conditions, the heat flux through the system. In this case, the known temperature data from the thermocouples and optical fibers, along with the assumption of axial symmetry, allows INTEMP to solve for the unknown heat flux values between the rod surface and the water. In the input file for INTEMP, one can define the geometry of the system, such as the length, diameter, and nodal locations, as well as the material data for each defined element. By plugging the temperature data into the input files for INTEMP, the software then uses Crank-Nicolson finite element approximation to determine the unknown heat fluxes and

temperatures. The Crank-Nicolson method is defined using Eq. 3.3, where C_i is a heat capacitance matrix, K_i is a heat conductance matrix, T is a vector that represents the nodal temperature data being input, q_i is a vector of the known heat fluxes in the system, f_i represents the unknown heat fluxes in the system, P is a participation matrix defining how the fluxes are applied, and h is the step size.

$$\left(C_i + \frac{K_i h}{2}\right) T_{i+1} = \left(C_i - \frac{K_i h}{2}\right) T_i + h q_i + h P f_i \tag{3.3}$$

In addition to this method, further analysis can be done to smooth out the results, the number of iterations can be increased until the data matches the calculated temperature at the measurement locations, and first-order regularization can be implemented. An example of the input .DAT file used by INTEMP is given in Appendix G. For the analysis of surface flux values, temperature data between 0 and 20 cm with a data point separation of 0.5 cm are used, for a total of 40 data points per test. While the optical fiber measurement system collects data every 0.65 mm, a 0.5 cm measurement resolution is deemed acceptable for determining the relevant factors discussed. This is further discussed in the Analysis chapter.

After calculating the corrected temperature data, it is then used in the input file for INTEMP (described in the following section), where the resulting surface heat flux can be determined. Since the quenching point, T_Q, is followed by a sharp decrease in temperature, the temperature at which this occurs can be determined by finding the point of highest flux increase (*i.e.* the maximum point of the first derivative of flux). A more detailed explanation for the processes that INTEMP uses can be given in the user's manual (Trujillo (2003)).

Chapter 4

Results

4.1 Vapor Film Collapse and Propagation

While most of the data that is found must first be analyzed using INTEMP before concrete, quantitative results can be determined, some qualitative results can be seen from initial observation of the temperature data from the optical fibers and thermocouples. Fig. 4.1 shows four still images from the high-speed camera footage, taken from quenching of the Monel k500 rod with liquid temperature of 98°C. A vapor film can be seen above the surface of the rod, with ripples along the surface of the film increasing to the point of film collapse. The quenching front begins below the frame and propagates upward, resulting in full liquid contact with the rod surface.

The vapor film that is produced before the rod quenches is much more violent than at higher subcoolings. Fig. 4.2 shows the behavior of the vapor films at water temperatures of 88, 92, and 95°C. These images are taken at approximately the same rod surface temperature of 430-460°C. At higher subcoolings, the vapor film is seen to be much smoother and thinner. This is due to the low vapor production at high subcoolings, since the bulk temperature of the water is much lower than the saturation temperature (T_{sat}). Film thickness is seen to be noticeably different between 92 and 95°C, and film production is so rapid in the 95 and 98°C cases that a standard film thickness is difficult to determine, although it has a clearly higher overall thickness than at lower subcooling temperatures.

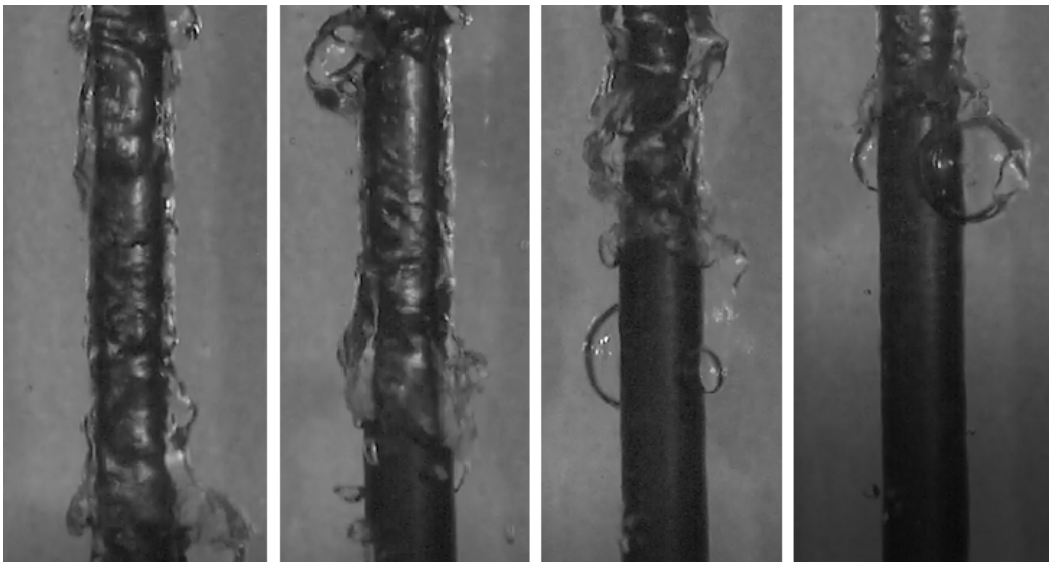

Figure 4.1: Quenching images of Monel rod at 98°C subcooling taken from high-speed camera

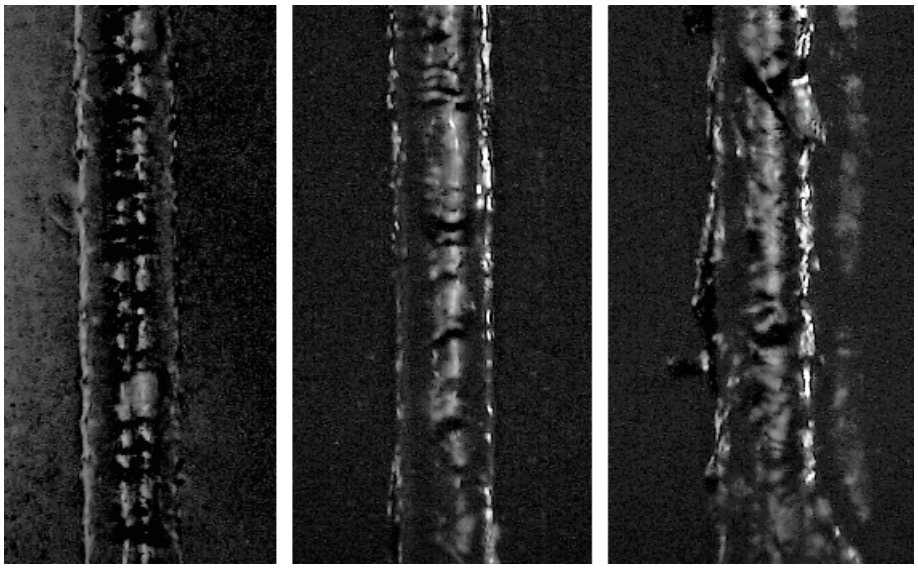

Figure 4.2: Vapor film during quenching of Monel rod at 88°C (left), 92°C (middle), and 95°C (right) subcooling

4.2 Quenching Temperature Results

In quenching experiments, the surface of the rod begins well above T_{min} and enters immediately into the film boiling regime. While in this regime, the surface temperature decreases

steadily until it reaches T_Q, where a sudden drop in temperature can be recorded via the thermocouples/optical fibers. This drop in temperature due to liquid/wall contact, where the liquid coolant is able to pull heat away much more effectively than the vapor was. Eventually, the slope of this temperature curve begins to level out as the wall temperature approaches the temperature of the coolant. This process is shown in Fig. 4.3, where the film and nucleate boiling regimes, as well as the location where quenching occurs, have been labeled.

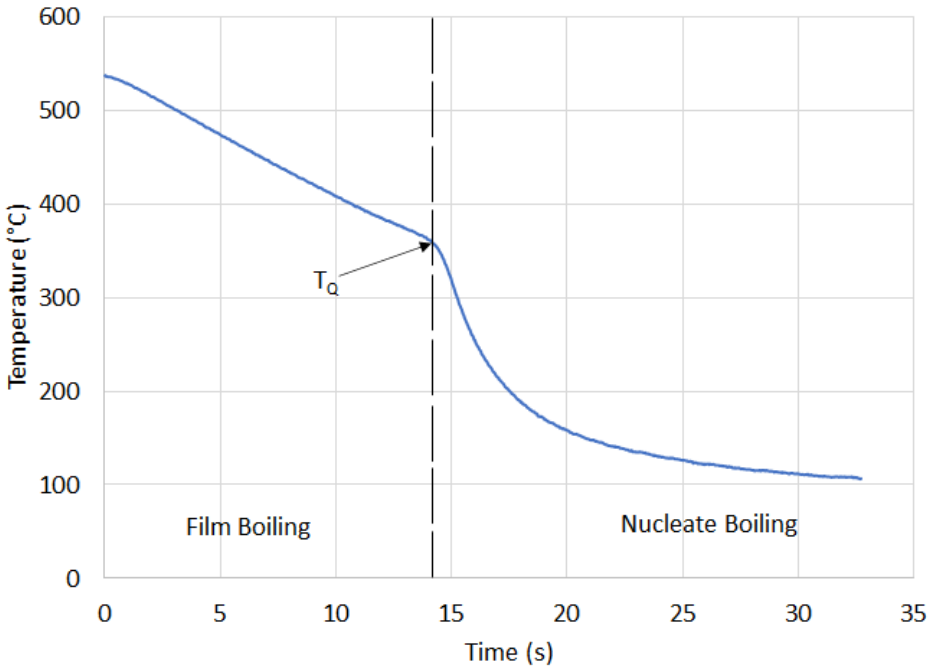

Figure 4.3: Quenching plot taken from a single fiber measurement from SS Test 4, with boiling regimes and T_Q labeled

From the initial data that has been taken from the optical fiber measurements, a temperature curve can be taken for each axial measurement location. All of the initial fiber temperature results are located in Appendix B, and all of the initial thermocouple results are in Appendix C. Fig. 4.4 shows an example from 40 measurements taken along the rod length, every 0.5 cm. This visualization is not the easiest to take data from, but it allows individual

quenching temperature to be determined with relative ease from temperature measurements alone. However, in order to determine the actual quenching temperature, a more accurate result would come from calculating the point when the surface flux increases rapidly, and determining the surface temperature at that point. This analysis is conducted in the following chapter. To compare, the plot on the right of Fig. 4.4 shows the temperature data taken from the thermocouples alone. As can be seen, the significant increase in axial measurement resolution allows for a much better understanding of the quenching front propagation and the quenching temperature axially.

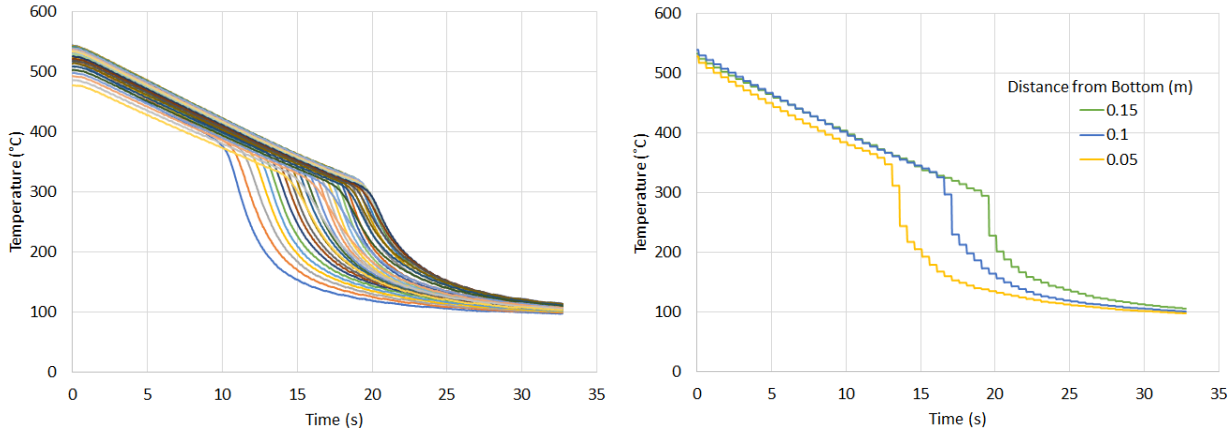

Figure 4.4: Original optical fiber temperature data (left) and thermocouple temperature data (right) from SS Test 4 (88°C subcooling)

It is clear from Fig. 4.4 that the quenching process is a much more complex process when using multiple axial measurement locations. Primarily, the optical fiber data indicates a large range of temperatures at which the rod is quenching, approximately 80°C between the maximum and minimum quenching temperature.

Looking specifically at the measured quenching temperature comparison between the optical fibers and the thermocouples, a minor difference in the time of quenching is expected. This is because the two measurement devices are at different locations from the center, and thermal inertia will cause the fiber measurements to appear to lag behind the thermocouple

measurements. Fig. 4.5 shows the temperature measurements taken from the fibers and thermocouples at the same axial location. From these measurements, a quenching time difference of less than 1 second and a temperature difference throughout the test of between 3-5°C agrees with the expected results.

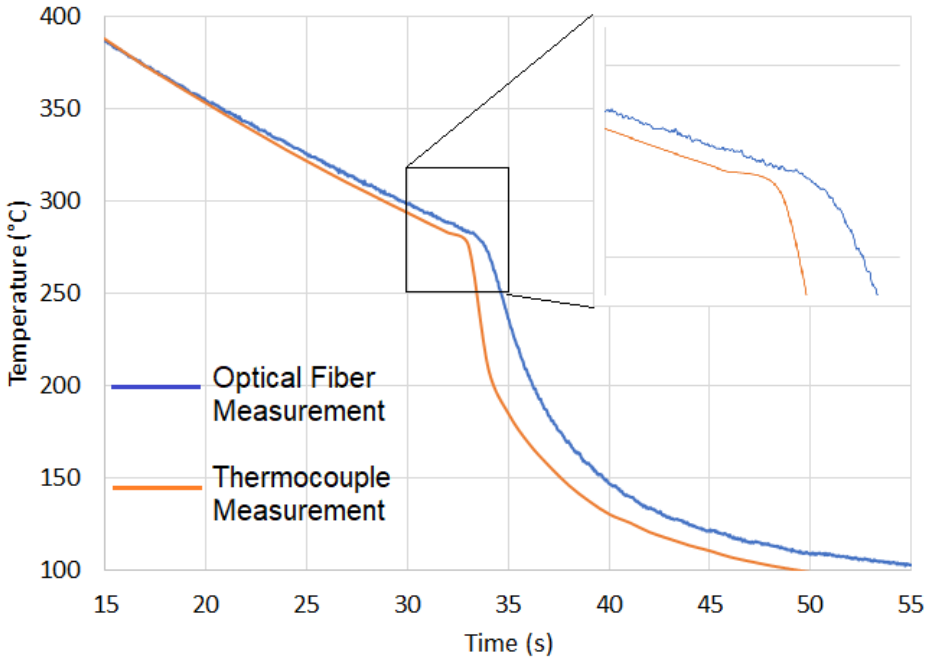

Figure 4.5: Quenching curves from optical fiber measurements vs thermocouple measurements, taken at the same axial location from Monel test at 98°C subcooling

4.3 Surface Temperature Comparisons

Fig. 4.6 shows a comparison between the recorded centerline temperature of the rod, measured using the optical fibers, and the surface temperature calculated using INTEMP. This data was taken from the Monel 98°C test measurements located 5 cm from the bottom of the rod. As is expected, there is a minor separation in temperature (approximately 2-5°C) as well as time of recorded quenching due to thermal inertia.

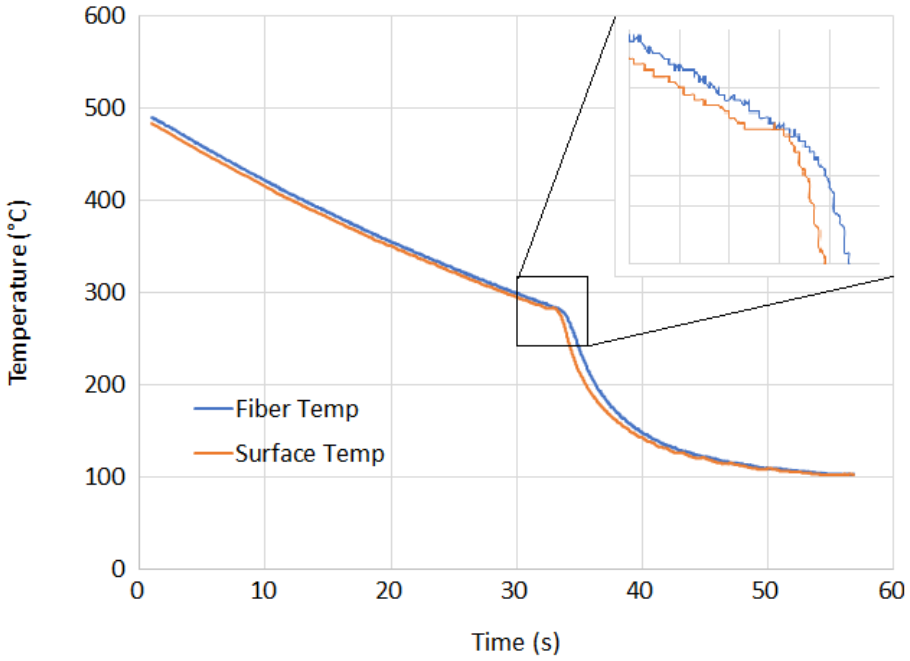

Figure 4.6: Comparison of fiber-recorded centerline temperature to INTEMP calculated surface temperature from Monel quenching at 98°C

In order to determine if there is a strong enough accuracy in the optical fiber data and the INTEMP calculations, a comparison to the measured surface data must be made. Fig. 4.7 shows a comparison between the temperature recorded by the thermocouples and the surface temperature calculated by INTEMP at that same location. Again, this data was taken from the Monel 98°C test measurements at the 5 cm location. As can be seen, the quenching temperature measured at this location is indeed close enough to determine accuracy of the calculations done by INTEMP. One should notice, however, that while the surface temperatures line up remarkably well before and during quenching, the temperatures begin to diverge once the quenching front has passed through that location. There are a few potential reasons for this, one of which is that the low spatial resolution of the thermocouples results in discretization of the surface heat flux calculations that cause these results to differ from the fiber results. This potential cause is tested in Appendix A. However, further studying

will need to be done to determine what the primary cause is.

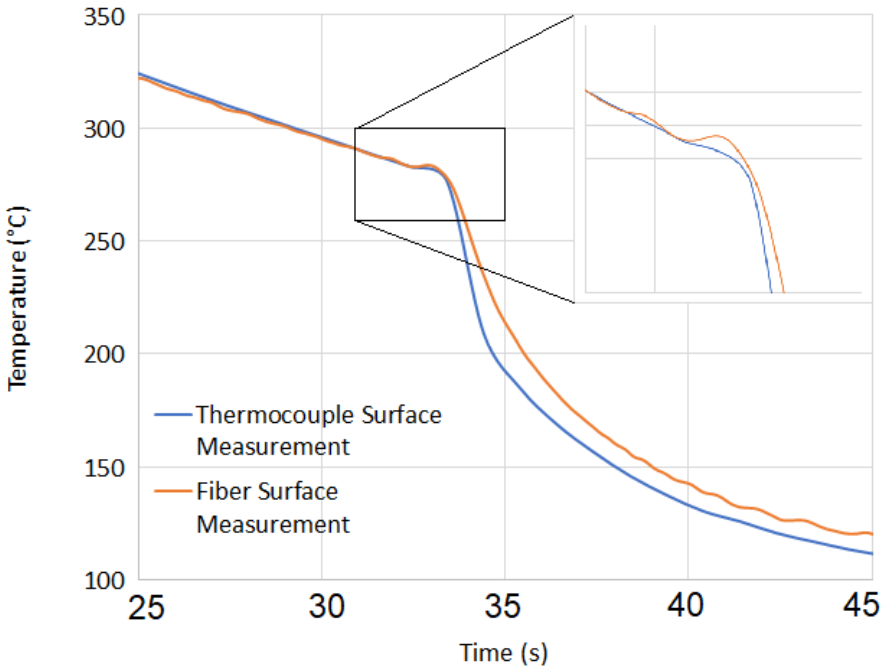

Figure 4.7: Comparison of thermocouple-recorded near-surface temperature to fiber-recorded INTEMP calculated surface temperature from Monel quenching at 98°C

4.4 Surface Heat Flux Values

Fig. 4.8 shows an example surface plot of the calculated surface temperature during quenching, as well as the calculated surface flux temperature. The surface heat flux along the rod increases significantly at the point where quenching occurs. From these two plots, the quench front propagation can easily be seen, and the quench front propagation speed can be determined and compared with the high-speed camera recording. All of the surface temperature plots from the fiber data are located in Appendix E, while the surface flux plots are located in Appendix D.

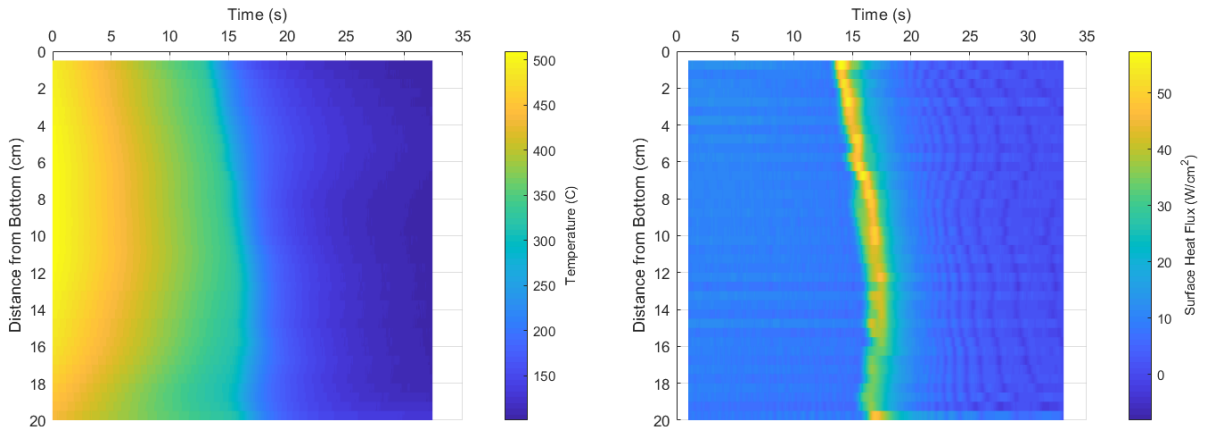

Figure 4.8: Example plot of surface heat flux vs time (left) and surface temperature vs time (right) from SS test at 88°C subcooling

4.5 Boiling Curves

A comparison between the surface temperature and the surface heat flux at various locations axially can give a good recreation of the "boiling curve", indicating a notable transition from film boiling, through transition boiling, into nucleate boiling. All of the boiling curves obtained from each test are given in Appendix F. Fig. 4.9 compares the boiling curves obtained from optical fiber measurements to the boiling curves obtained from thermocouple measurements 5 cm from the bottom of the rod. Note that, while boiling curves can be produced from both of the data collected, the fiber data has much higher resolution than the thermocouple data, potentially due to the low spatial resolution in the flux calculations from the thermocouples measurements.

Overall, these data indicate that the optical fibers are capable of recording data with a similar degree of accuracy to thermocouples, while also being able to take these measurements across a much wider range of locations. This highly improves the spatial resolution for measurement during quenching, and can allow for greater precision in measurement and heat flux calculations. As a result, the following analysis chapter takes data solely from the

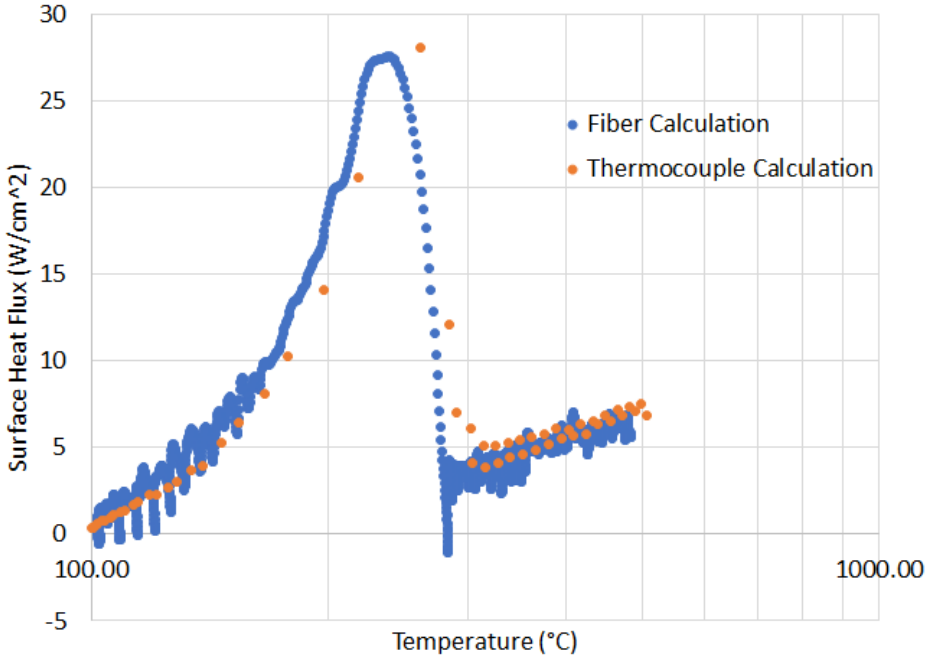

Figure 4.9: Comparison between boiling curves from optical fiber measurements and thermocouple measurements from Monel quenching at 98°C subcooling

optical fiber measurements in order to highlight the applicability of this technology.

Chapter 5

Analysis

5.1 Effect of Cladding Material

Quenching values are taken by finding the temperature values from the 40 measured axial locations that correspond to the beginning of the sharp increase in surface heat flux. This point is determined to be the most accurate measure of T_Q as it also corresponds to the sharp increase in the heat transfer coefficient at that point. This relation is shown in Fig. 5.1, where h is given by Eq. 5.1.

$$h = q''_{wall}/(T_{wall} - T_{sat}) \tag{5.1}$$

Outliers are shown as x's on the plot, defined as $\pm 2.7\sigma$ from the mean of the set.

Fig. 5.2 shows the quenching temperature ranges from the stainless steel, Monel, and Inconel rods at the same subcooling and at approximately the same surface roughness values. As can be seen, the median quenching temperature of the Monel and Inconel rods under these conditions is quite similar, at 337.61°C and 337.13°C, respectively. This result is expected, since Monel and Inconel are both nickel-based alloys that have similar material and thermal properties. The stainless steel rod is shown to have a much lower range of quenching temperatures under the same conditions.

It should also be noted that for both the Monel and Inconel rods, quenching is shown to

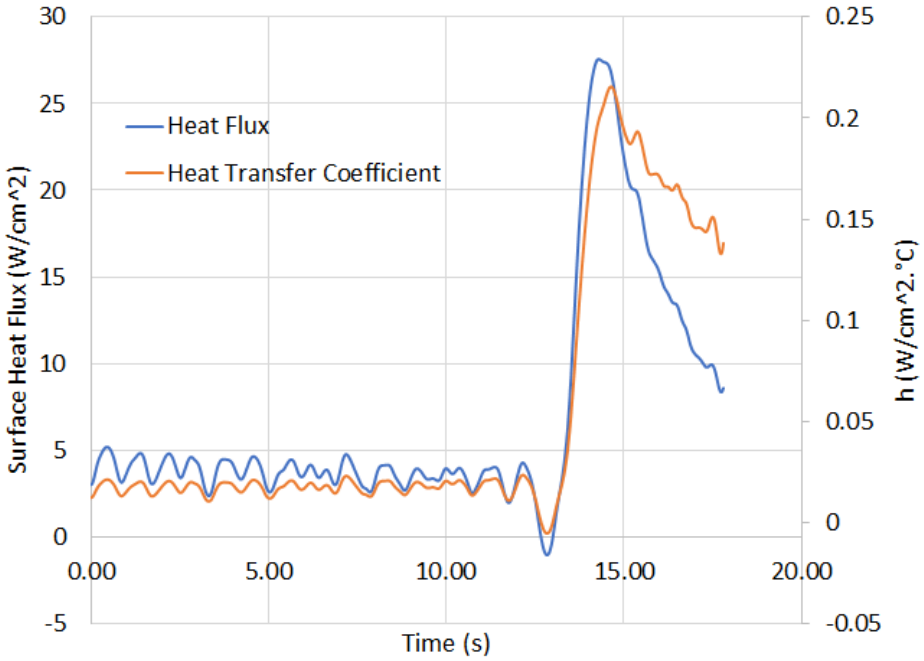

Figure 5.1: Surface heat flux and heat transfer coefficient during quenching, taken at 5 cm axial location from Monel test at 98°C subcooling

have occurred at very high surface temperature, always originating from the bottom of the rods. This is believed to be likely due to the geometry of these rods in particular, since the welding on the bottom of these rods produced a sharp edge that could possibly allow for rewetting at higher temperatures due to higher wettability. Fig. 5.3 shows the three rod ends to better visualize this difference.

5.2 Effect of Surface Roughness

Previous quenching experiments have often looked at the effect of surface wettability on quenching temperature (Seshadri and Shirvan (2018), Kang *et al.* (2017), Yeom *et al.* (2017)). This is often due to the noted impact of surface oxidization on the wettability of the substrate being tested after repeated experiments. The oxide layer builds up over suc-

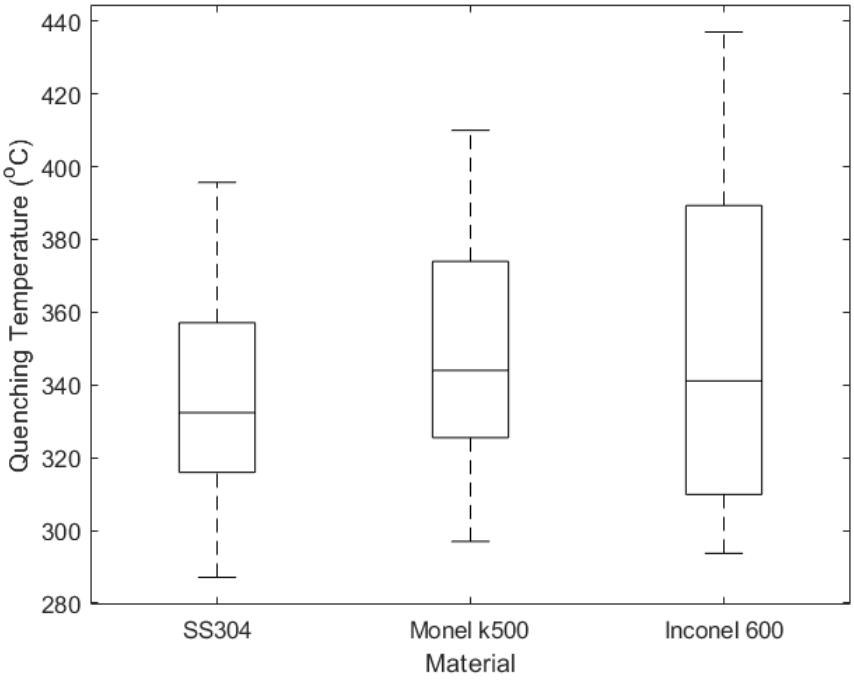

Figure 5.2: Quenching temperature comparison for SS304, Monel k500, and Inconel 600

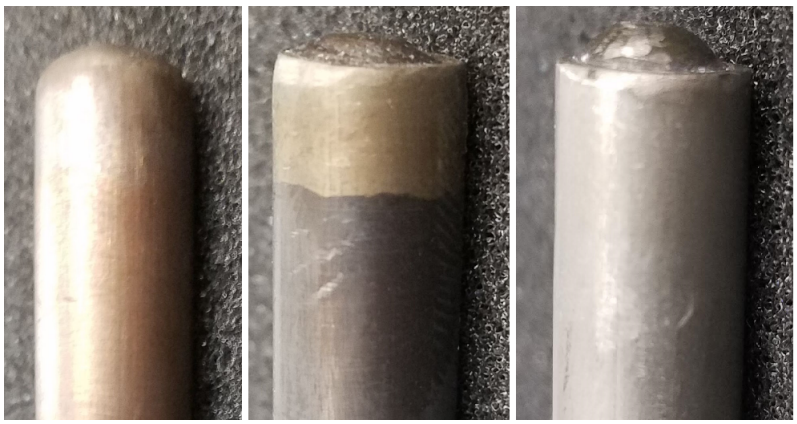

Figure 5.3: Comparison of welding at the end of each rod, with SS304 (left), Monel k500 (middle), and Inconel 600 (right)

cessive heating and quenching of the rod, enhancing the surface roughness of the material and potentially adding microscopic pores and fissures which act as nucleation sites. As seen in Fig. 5.4, the surface of the Monel rod has oxidized after quenching, due to its significantly darker color.

Figure 5.4: Monel rodlet before (top) and after (bottom) multiple quenchings

Surface roughness, in addition to liquid contact angle, is typically used to characterize the surface. As stated before, a surface profilometer is used to determine the surface roughness values before each quenching experiment. Fig. 5.5 shows the quenching temperature ranges from five tests, with the surface roughness measurement before each test located on the x-axis. Note that the surface roughness after each test increases, which is assumed to be due to the oxide layer being built up on the surface of the rod with each subsequent quenching. This plot is using data from Monel quenching at 88°C subcooling.

As shown in this figure, there appears to exist a definite increase in the overall quenching temperature along the rod, with the exception of a few outliers, notably on the second quenching test. From this, the data seem to show a trend of increasing overall quenching temperature that is directly related to the increase in surface oxidation. This trend falls in line with the conclusions presented in earlier works that noted a similar effect

Fig. 5.6 shows the quenching temperature ranges from the surface roughness tests on the SS304 rod. These experiments were conducted in the same fashion, where tests were repeatedly conducted at 88°C subcooling without removal of the oxide layer that forms from each test. Again, an increase in the overall average quenching temperature can be seen. However, the quenching temperature range also is seen to be increasing with increasing sur-

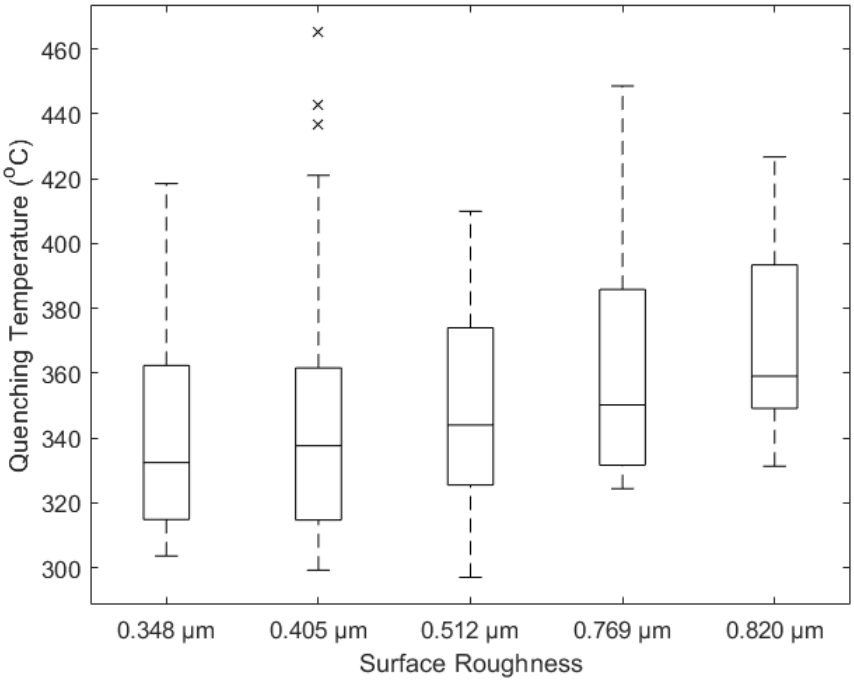

Figure 5.5: Effect of surface roughness on Monel quenching temperature

face roughness. Therefore, while the median and mean quenching temperature is shown to increase with an increase in the surface roughness value, there are locations on the rod that are actually measured to have quenched at *lower* temperatures than the same location from previous tests at lower surface roughnesses. Therefore, it is difficult to conclude a definite increase in T_Q resulting from an increase in the surface roughness, though there does appear to be a marked trend. One potential draw from this information may be that the surface of the rods does not oxidize at the same rate across the entire axial span. Since surface roughness values from these tests are only measured at one axial location, the results may not account for this variation.

Fig. 5.7 shows a comparison between the boiling curves for Monel based on the surface roughness measured before each test. These boiling curves are from data taken 5 cm from the bottom of the rod. While the increase in quenching temperature can be seen from this

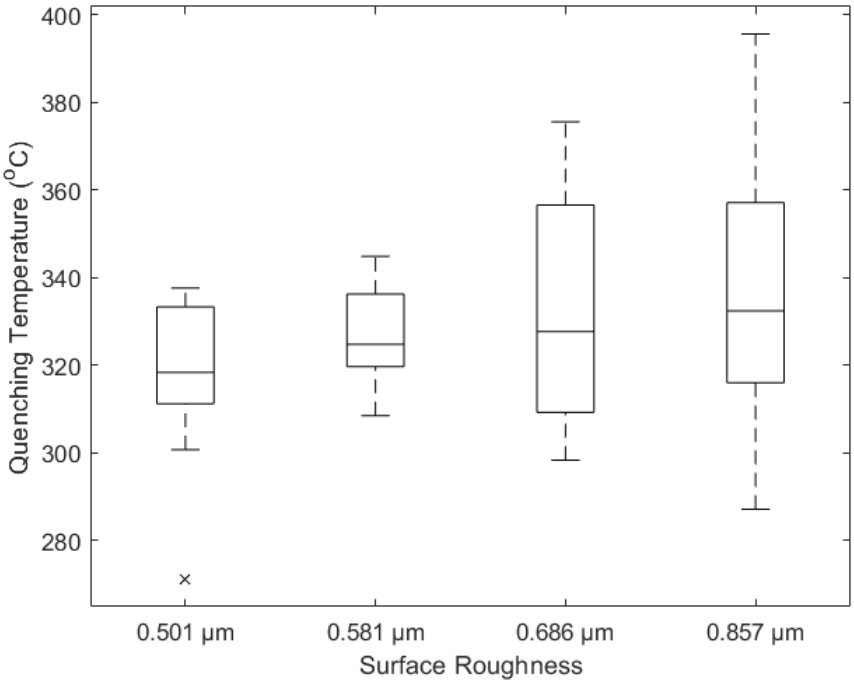

Figure 5.6: Effect of surface roughness on stainless steel quenching temperature

plot, there does not seem to be a noticeable trend in the magnitude of the surface heat flux that is dependent on the surface roughness value.

5.3 Effect of Liquid Subcooling

The temperature of the subcooled liquid being used to quench the rods has also been tested to have a strong impact on the quenching temperature. As noted in earlier papers, a decrease in the liquid temperature (*i.e.* an increase in the liquid subcooling) has been determined to cause an increase in the quenching temperature by every researcher noted in this literature review (Ebrahim *et al.* (2016), Kang *et al.* (2019)).

The effect of liquid subcooling on the quenching temperature of the Monel rod is given in Fig. 5.8. As can be seen, there exists a clear trend that follows the conclusions of previous

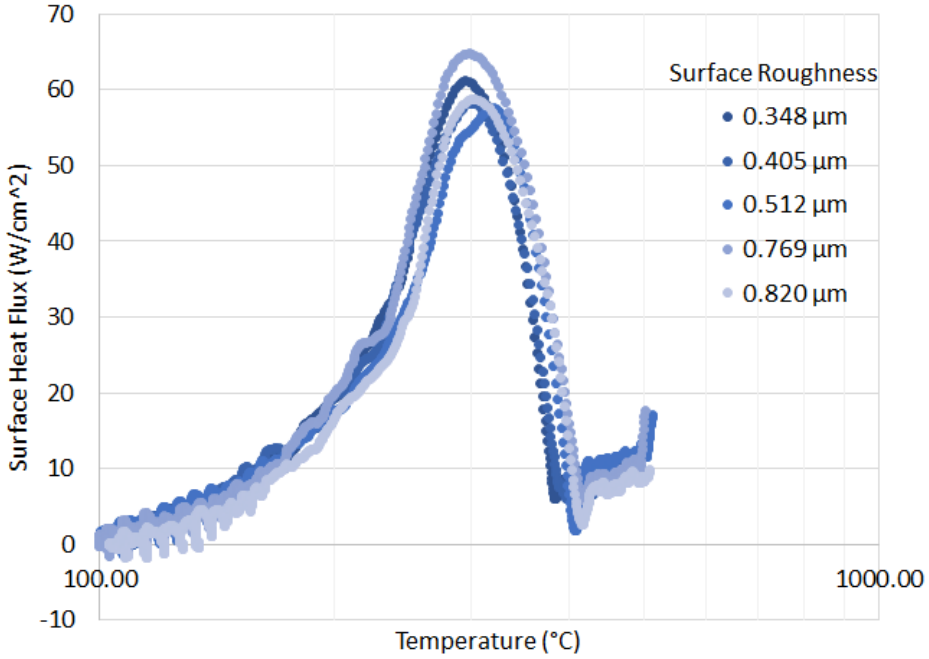

Figure 5.7: Boiling curve comparison for Monel at various surface roughness values

authors. Note that before each of these tests, the surface of the rod is sanded down using a fine grit sanding sponge such that the surface roughness of the rod is similar enough that any changes in quenching temperature can be assumed to be almost entirely due to the change in liquid subcooling.

Fig. 5.9 shows the boiling curves for Monel taken 5 cm from the bottom of the rod at various subcoolings. As seen, both the quenching temperature and the surface heat flux maximum during quenching increase with higher subcooling. Something interesting to note is that the quenching phenomenon between 95 and 98°C overall seems to be remarkably similar, with quenching temperatures that are separated by a few degrees, surface flux values that are almost equal, as well as similar vapor film behavior. From this, one may conclude that the effect of liquid subcooling on quenching is most apparent below liquid temperatures of 95°C. This behavior is similar to that in Fudurich *et al.* (2016), where the boiling curves from 5°C and 2°C subcooling are significantly closer to each other than to the other subcooling tests.

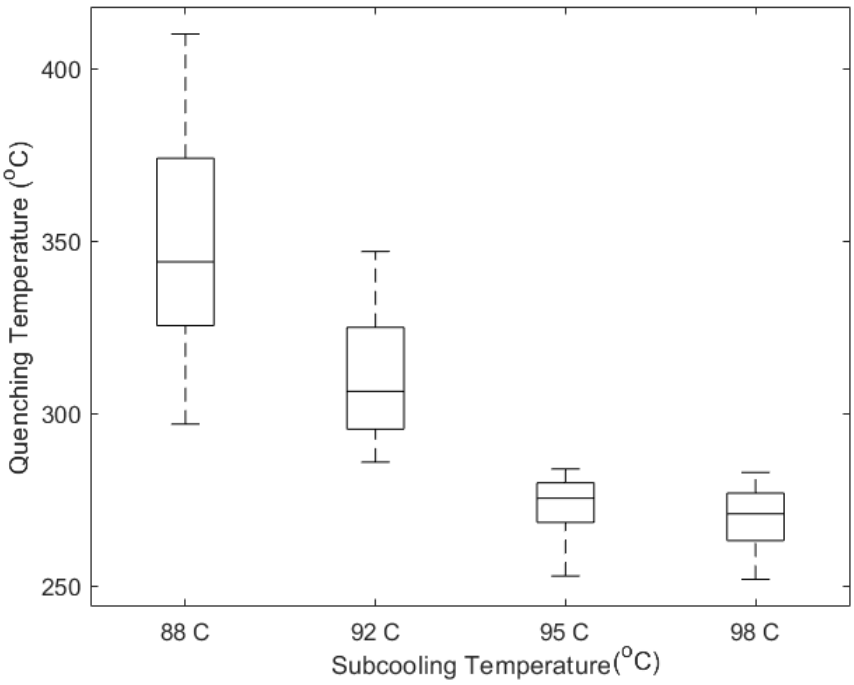

Figure 5.8: Effect of liquid subcooling on Monel k500 quenching temperature

5.4 Effect of Axial Heat Conduction

A primary source of error in previous correlations for quenching temperature is the effect of axial heat conduction, which has proven difficult to quantify due to low spatial measurement resolution. Fig. 5.10 shows a comparison between the axial conduction measured (defined using $-k\frac{dT}{dz}$) and the time it takes for the next location to quench. The axial conduction term is calculated using the temperature measurement on the surface of the rod during quenching at that location, divided by the temperature of the location that is about to be quenched, multiplied by the thermal conductivity. The time difference between quenching points, defined to be the time between the quenching of one axial location and the quenching of the following location, can be further used to approximate the quench front propagation speed, given that the distance between measured temperatures is constant at 0.5 cm.

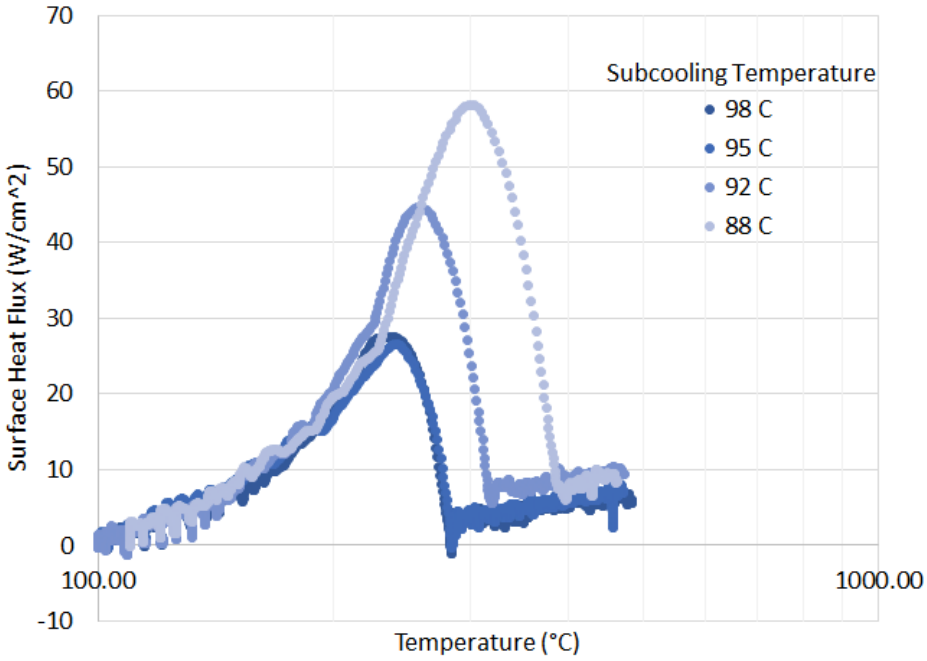

Figure 5.9: Boiling curve comparison for Monel at various subcooling temperatures

During quenching, there is a large temperature gradient axially due to some sections of the rod having liquid contact and others not, as well as due to those currently going through the transient. Because of this, the heat flux occurring between these axial locations is being affected, and the heat transfer increases during quenching. Fig. 5.11 shows the axial heat flux between three points 0.5 cm apart from each other during quenching. The axial heat flux here is calculated using Eq. 5.2. Since the rod is quenching from the bottom in this case, the 4.5 cm node (marked as node 18 on the INTEMP mesh) registers quenching first. This causes a sharp increase in the heat flux between nodes 18 and 20. At point B, node 20 measures quenching, which results in the heat flux decreasing between nodes 18 and 20, and the heat flux then increasing in the opposite direction between nodes 20 and 22 (shown on the blue curve). By comparing the magnitude of flux values to the boiling curve for 98°C test from Fig. 5.9, it is clear that these heat fluxes are quite significant, as they are of equal order of magnitude to the film boiling heat flux between the heated surface and the coolant.

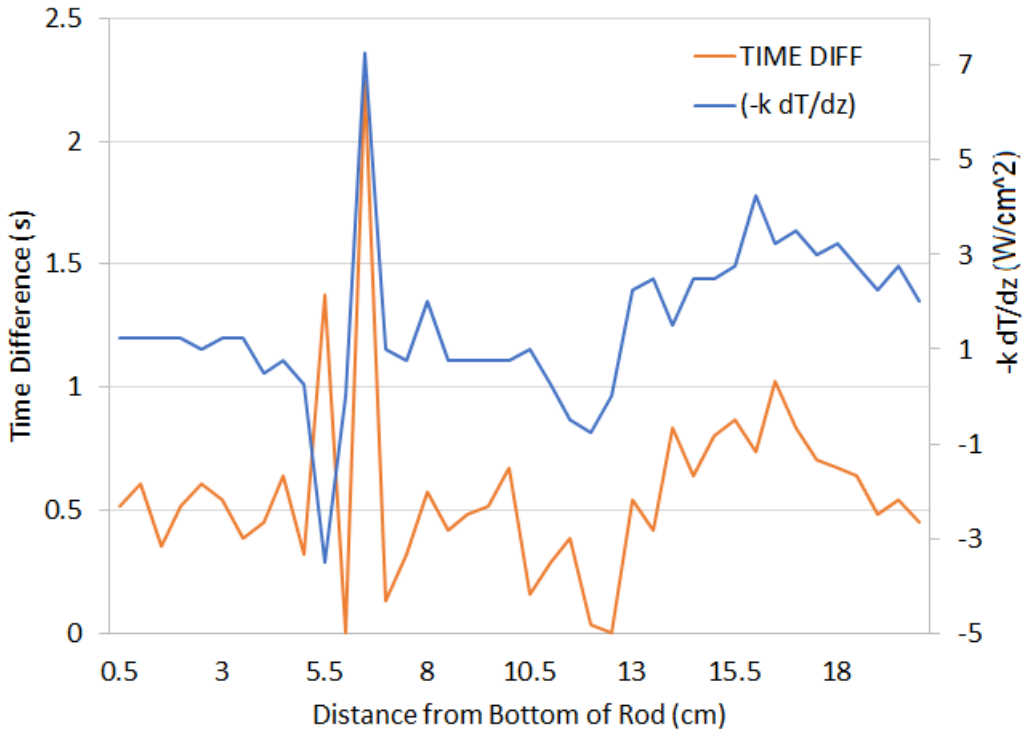

Figure 5.10: Comparison of axial conduction $-k\frac{dT}{dz}$ vs time between quenching of current axial location and quenching of following axial location, from Monel 95°C test

$$q''_z = -k\frac{dT}{dz} \tag{5.2}$$

5.5 Comparison to Previous Experimental Work

Fig. 5.12 shows the effect of liquid subcooling that was found in Fudurich (2016). As can be seen, the quenching temperature measured on the stainless steel rod used increased with increasing subcooling, in agreement with the results obtained in this thesis. Additionally, the boiling curves obtained from the Fudurich thesis follow a similar trend of increasing maximum surface heat flux with increasing subcooling.

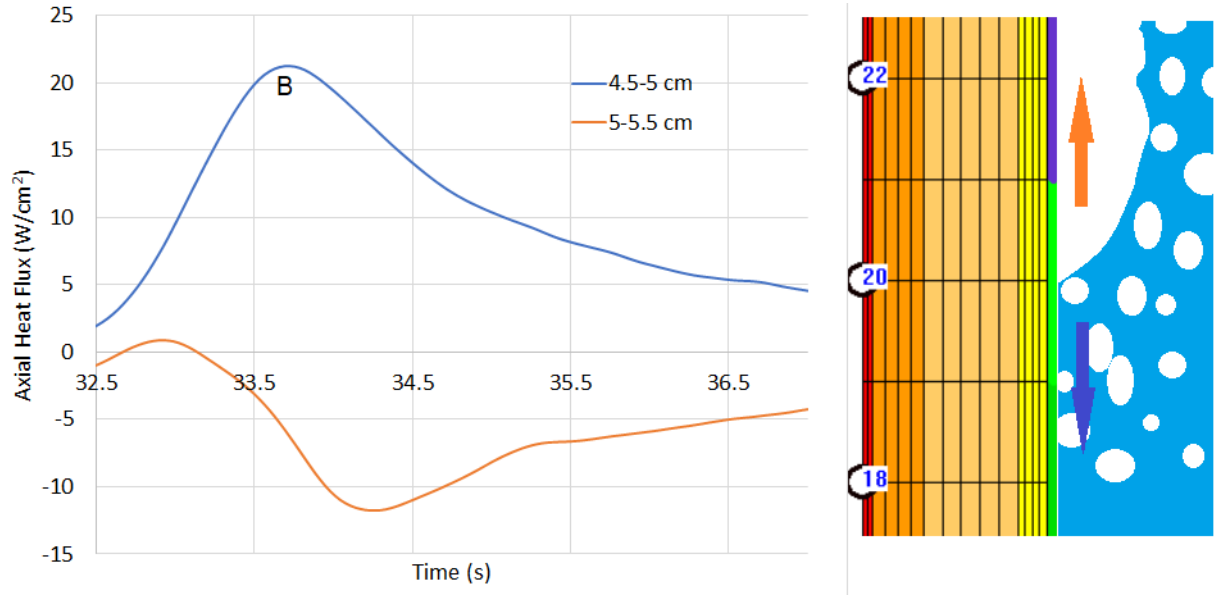

Figure 5.11: Axial heat conduction from Monel quenching test at 98°C subcooling

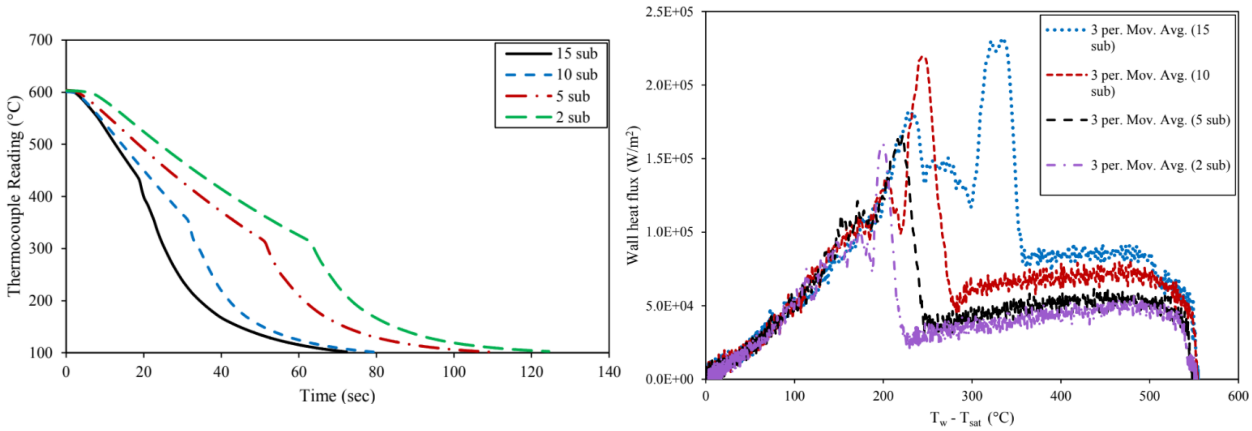

Figure 5.12: Quenching plots and boiling curves at various subcooling values from Fudurich (2016)

Data from Monel testing is compared to two of the T_{min} correlations described in the literature review, by Peterson and Bajorek (2002) (which was the correlation that was compared to in Fudurich (2016)) and by Groeneveld and Stewart (1982). Fig. 5.13 shows this comparison, with the data points taken from the experimental quenching results discussed in the previous section. While the Peterson and Bajorek correlation is able to make predictions within the range of quenching measurements from the experimental data, there are several

quenching temperatures measured to be well below what the correlation calls T_{min}. This significant difference in temperature between the correlation's predictions and the measured values likely comes primarily from the limited measurement resolution that was used for these correlations, as both utilized thermocouples.

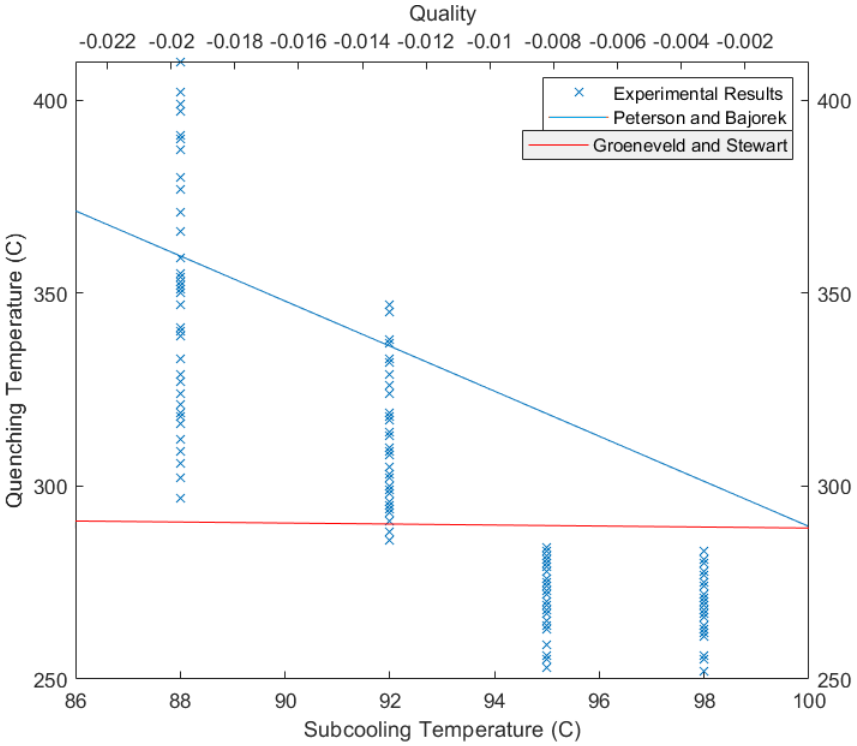

Figure 5.13: Comparison of Monel quenching data to correlation predictions at various subcoolings/qualities

5.6 Uncertainty in Analysis

As with all experimental measurements, there is a certain degree of uncertainty that must be taken into account. The primary source of error in these experiments comes from the temperature measurements from the optical fibers. The optical fiber sensors measure the spectral shift at that axial location, which the interrogator then converts to a temperature

measurement. As stated earlier, this temperature conversion has to be rewritten in order to allow for the proper measurements to be recorded over the entire temperature range. Fig. 5.14 shows both the spectral shift measurements taken at various temperatures within the testing range as well as the calculated polynomial curve.

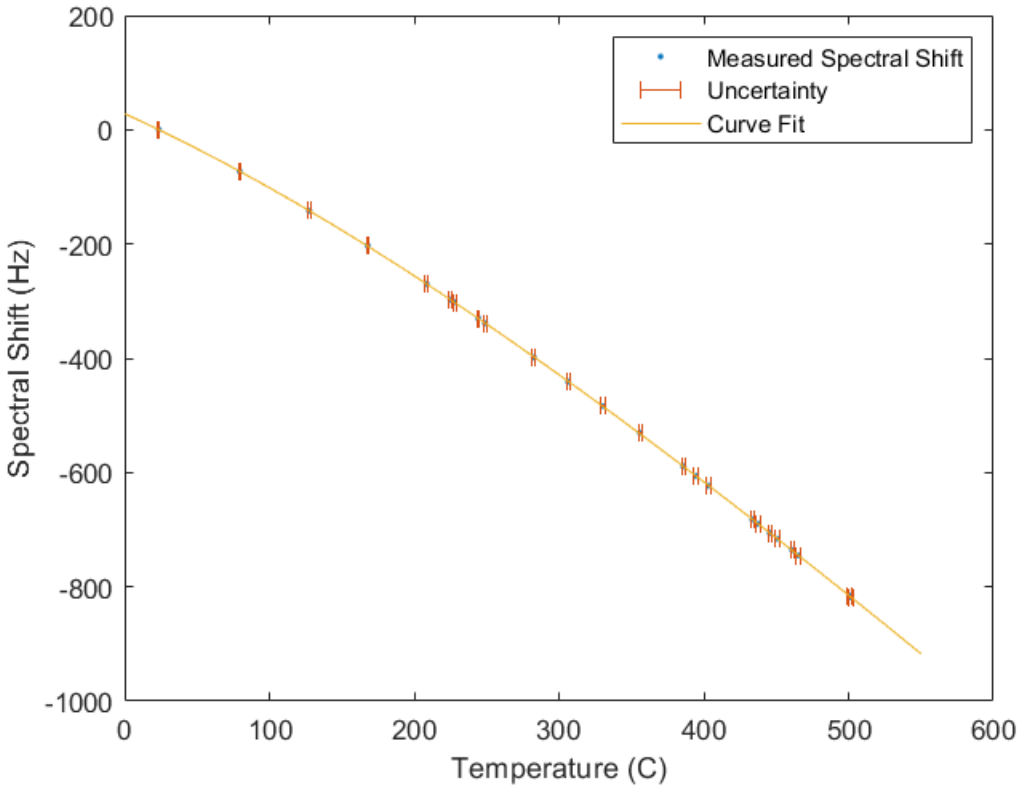

Figure 5.14: Comparison of spectral shift measurement plotted against thermocouple temperature with polynomial curve fit

For this curve fit, a fourth-order polynomial was determined to have high enough accuracy to the real spectral shift measurement. Table 5.1 shows a breakdown of the original measured temperatures and spectral shifts, as well as the respective fitted temperature that aligns with that spectral shift. From this, the polynomial fit exists within an error margin of $\pm 1.33\%$, with an average error of 0.032%. The thermocouples themselves have an uncertainty of the higher of 0.4% or 1.1°C, and the data logger has an additional uncertainty of $0.2\% \pm 0.5$°C.

This corresponds to a total uncertainty of the thermocouple measurements to be within 2.504°C. Since the optical fiber measurements are now tied to the measured thermocouple readings, they take on that same uncertainty. This leads to a combined uncertainty in optical fiber measurement of within 3.02°C, with an average error margin within 1.89°C.

Spectral Shift (Hz)	Measured Temp (C)	Fitted Temp (C)	Fit Error (%)
0	23.69	24.00454	-1.327737
-72.4	79.44	78.93442	0.6364377
-142	127.58	127.5506	0.0230365
-203.5	168	167.7363	0.1569943
-297.4	225.13	225.1856	-0.0246902
-398.5	282.69	283.168	-0.1690964
-483.6	330.33	329.8176	0.155107
-589	385.9	385.7072	0.04996611
-682	433.5	433.6705	-0.03933336
-690	437.42	437.7405	-0.0732735
-736	461.1	460.9615	0.03004343
-745.3	465.5	465.6167	-0.02507868
-815.5	500.5	500.2728	0.04539285
-818.2	501.65	501.587	0.01255962
-716	450.75	450.9043	-0.0342311
-706	445.6	445.853	-0.05677929
-623	403.19	403.3801	-0.04714325
-606	394.55	394.5637	-0.00347398
-530.5	356	354.9082	0.30669
-441	306.45	306.6672	-0.0708852
-339	249.05	249.4488	-0.16014
-330	244.25	244.252	-0.00080622
-302	227.8	227.9001	-0.04392602
-270	208.6	208.8394	-0.1147495

Table 5.1: Spectral shift curve fitting, with errors as a percent of the actual temperature

Further uncertainty in analysis can be checked using INTEMP. While the smoothing option is not used in the calculations from these data sets, INTEMP runs a check on the smoothness of the data nonetheless. Table 5.2 shows the root sum square for each data point (marked

as sigma), as well as the maximum difference between the smoothed data (if it were used instead) and the actual data for each axial location, as well as the step where this maximum difference occurs. Estimates for INTEMP converge after four iterations, as determined by the output file of each test. As seen, the sigma values do not vary by more than 0.2, indicating that the measured data likely does not contain any significant errors that would cause convergence to fail. This is further highlighted by the relatively low maximum temperature differences, with the highest calculated difference being less than 2°C. From this, it is deemed unnecessary to apply the smoothing parametrization on the data.

Location (cm)	Sigma	Max Diff	Step	Location (cm)	Sigma	Max Diff	Step
0.5	0.2737	1.365E+00	873	10.5	0.3244	1.925E+00	5
1.0	0.2985	1.235E+00	834	11.0	0.3201	1.125E+00	858
1.5	0.2877	1.288E+00	2	11.5	0.3325	1.322E+00	1127
2.0	0.344	1.693E+00	4	12.0	0.3075	1.135E+00	1247
2.5	0.2709	1.033E+00	1127	12.5	0.2817	1.040E+00	1007
3.0	0.2975	1.161E+00	1010	13.0	0.2913	9.805E-01	1250
3.5	0.3123	1.258E+00	904	13.5	0.3476	1.396E+00	853
4.0	0.2894	1.001E+00	908	14.0	0.3128	1.378E+00	904
4.5	0.365	1.207E+00	1049	14.5	0.3062	1.038E+00	10
5.0	0.3333	1.517E+00	873	15.0	0.3117	1.287E+00	1619
5.5	0.2775	1.153E+00	883	15.5	0.3261	1.205E+00	964
6.0	0.3161	1.443E+00	4	16.0	0.328	1.309E+00	1
6.5	0.3181	1.326E+00	924	16.5	0.3142	1.190E+00	981
7.0	0.2671	9.009E-01	1172	17.0	0.2715	1.085E+00	1068
7.5	0.3054	1.204E+00	1191	17.5	0.3232	1.387E+00	986
8.0	0.2877	1.959E+00	873	18.0	0.2834	1.185E+00	981
8.5	0.3033	1.026E+00	890	18.5	0.314	1.291E+00	870
9.0	0.2982	1.173E+00	490	19.0	0.3453	1.558E+00	184
9.5	0.3048	1.450E+00	1339	19.5	0.3249	1.629E+00	11
10.0	0.352	1.350E+00	233	20.0	0.3167	1.010E+00	964

Table 5.2: Square root sum values and data smoothing deviation from measured data taken from INTEMP output

Finally, while the data collected from the optical fibers is of a much higher resolution, for the sake of saving computational time a resolution of 0.5 cm was chosen for the measurement

input. To verify that this does not lose any valuable data, a comparison is made with a 0.25 cm measurement resolution. Fig. 5.15 compares the surface heat flux values computed in INTEMP. As seen, the surface heat flux calculations at the same axial location are shown to behave very similarly at the onset of quenching, both in timing and in magnitude of maximum heat flux value. Given that these are the two components that are used most heavily in studying quenching, the given mesh is determined to give accurate results. Additionally, the temperature values during quenching from both of these mesh resolutions are found to be nearly the same, with an average difference in the T_Q values at the same axial locations being less than 0.5°C, less than the uncertainty in the temperature measurements themselves. Because of this, the mesh used as well as the measurement resolution is found to be accurate enough to give conclusive results.

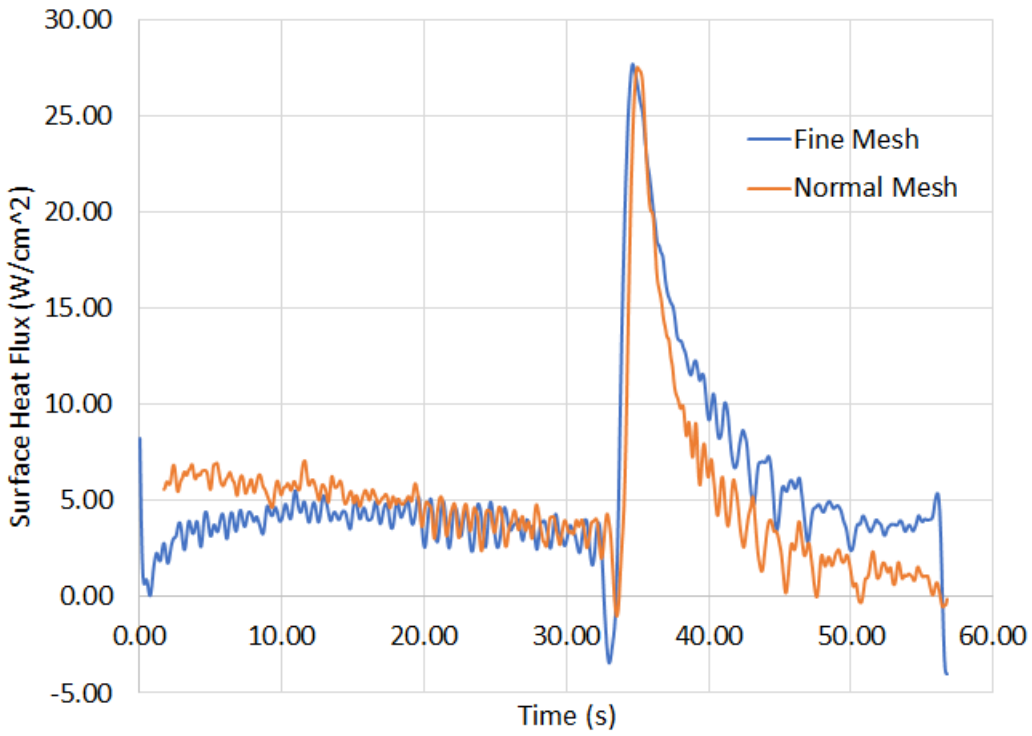

Figure 5.15: Comparison of surface heat flux values given different mesh sizes in INTEMP (taken at 5 cm axial location from Monel test at 98°C subcooling)

5.7 Final Results

The testing shows a marked trend in both the liquid subcooling and surface roughness and their effect on T_Q, where an increase in coolant temperature results in a decrease in the quenching temperature and an increase in the surface roughness results in an increase in the quenching temperature. The data from these experiments shows that the effect of the former appears to be of higher consequence on T_Q than the latter. Furthermore, a significant axial effect is reported with a magnitude similar to that of the surface heat flux during film boiling. Uncertainty analysis shows an error margin for measurement within an acceptable threshold, and smoothing analysis shows that the minor fluctuations in the measurement data are low enough to not require smoothing parametrization.

Chapter 6

Conclusions and Future Work

In this thesis, a series of quenching experiments is conducted at atmospheric pressure using 30 cm rods with a diameter of 9.5 mm. Three thermocouples are embedded into the rods at 5, 10, and 15 cm from the bottom of the rods, and optical fibers connected to temperature interrogator systems are inserted into the center of each rod before beginning each test. The purpose of these tests is to determine the effectiveness and applicability of these optical fibers in such experiments, as well as to determine the effect of axial heat conduction on the quenching temperature.

Performing the quenching tests with optical fibers inserted into the rods proved to initially be a challenge, as the fibers are quite fragile and prone to breaking if bent at too large an angle. However, the setup that is eventually designed allows for the fibers to measure temperature within the rods without fracturing. Thermal damage is shown to occur only after the fibers reach above 550°C, well above the required temperature for running a quenching experiment. This demonstrates the applicability of optical fibers under high physical and thermal stress environments such as those necessary for studying CHF and T_Q. These results, combined with the fibers giving a significant measurement resolution enhancement, allow for the sole use of optical fiber data for quenching analysis.

The data obtained, as well as the inverse heat transfer analysis done afterwards using INTEMP, indicate and highlight the effects of several factors that are influential to the quenching temperature of any axial point on the rods. Both the Monel and Inconel rods are found

to have better heat transfer capabilities during quenching than stainless steel, since they are found to quench at higher temperatures. A decrease in the temperature of the quenching liquid is found to cause an increase in the quenching temperatures of the rods. An increase in the surface roughness values measured before each test, due to the buildup of an oxide layer over the surface of the rods, also causes an increase in the quenching temperature. Both of these results agree with previous quenching studies performed on a number of different rod materials and under various pressures. In addition, a significant variation in the quenching temperature axially during all tests highlights the existence of an axial conduction effect that had not been determined in previous experiments due to limitations in measurement. This likely indicates that many of the measured "minimum film boiling temperatures" in previous experiments is not in fact the minimum temperature at which a vapor film can hold for all axial locations.

Further testing is expected to be done in the future, with the design for a high-pressure facility in progress. This facility will allow for a wider testing range to compare to a larger set of previous works, as well as allow for the expansion of our current understanding of the quenching temperature to include pressure and coolant mass flow rate as factors. Additionally, further testing with Zircaloy cladding is expected to provide more data with higher applicability to the fuel rods in nuclear reactors.

Bibliography

Fiber Optic Test & Measurement. https://lunainc.com/technology/.

Special Metals. https://specialmetals.com/.

P. J. Berenson. Film-Boiling Heat Transfer from a Horizontal Surface. *Journal of Heat Transfer*, pages 351-356, 1961.

S. A. Ebrahim, V. Fudurich, F. Beck, F. Cheung, S. Bajorek, K. Tien, and C. Hoxie. Effects of Liquid Subcooling and Initial Rod Temperature on the Minimum Film Boiling Temperature. 2016.

S. A. Ebrahim, S. Chang, F. Cheung, and S. Bajorek. Parametric Investigation of Film Boiling Heat Transfer on the Quenching of Vertical Rods in Water Pool. *Applied Thermal Engineering 140*, pages 139-146, 2018.

S. A. Ebrahim, E. Alat, F. A. Sohag, V. Fudurich, S. Chang, F. Cheung, S. Bajorek, K. Tien, and C. L. Hoxie. Effects of Substrate Materials and Surface Conditions on the Minimum Film-Boiling Temperature. *Nuclear Technology 205*, pages 226-238, 2019.

V. Fudurich. Effect of Liquid Subcooling, Initial Surface Temperature, and Surface Properties on the Minimum Film Boiling Temperature. Master's thesis, Pennsylvania State University, 2016.

D. C. Groeneveld and J. C. Stewart. The Minimum Film Boiling Temperature for Water during Film Boiling Collapse. *Proceedings, 7th International Heat Transfer Conference*, pages 393-398, 1982.

R. E. Henry. A Correlation for the Minimum Film Boiling Temperature. *Heat Transfer* -

Research and Design, pages 81-90, 1974.

P. Hurley and J. P. Duarte. Fiber Optic Sensing Application in Quenching Temperature Measurement. *ANS Winter Meeting*, pages 1804-1807, 2019.

O. C. Iloeje, D. N. Plummer, W. M. Rohsenow, and P. Griffith. An Investigation of the Collapse and Surface Rewet in Film Boiling in Forced Vertical Flow. *Transactions of the ASME*, pages 166-172, 1975.

O. C. Iloeje, D. N. Plummer, and W. M. Rohsenow. Transition from Film Boiling to Nucleate Boiling in Forced Convection Vertical Flow, Report No. DSR 72718-78, Engineering Projects Laboratory, Dept of Mechanical Engineering, Massachusetts Institute of Technology.

E. K. Kalinin, S. A. Yarko, V. Yskochelaev, and I. I. Berlin. Investigation of the Crisis in Film Boiling in Channels. *ASME Winter Annual Meeting*, 1969.

J. Kang, T. K. Kim, G. C. Lee, M. H. Kim, and H. S. Park. Quenching of Candidate Materials for Accident Tolerant Fuel-Cladding in LWRs. *Annals of Nuclear Energy 112*, pages 794-807, 2017.

J. Kang, T. K. Kim, G. C. Lee, H. Jo, M. H. Kim, and H. S. Park. Impact of System Parameters on Quenching Heat Transfer in the Candidate Materials for Accident Tolerant Fuel-Cladding in LWRs. *Annals of Nuclear Energy 129*, pages 375-389, 2019.

Y. Lee, T. J. Mckrell, and M. S. Kazimi. Thermal Shock Fracture of Silicon Carbide and its Application to LWR Fuel Cladding Performance During Reflood. *Nuclear Engineering and Technology 45*, pages 811-820, 2013.

R. A. Nelson. Forced-Convective Post-CHF Heat Transfer and Quenching. *Journal of Heat Transfer*, pages 48-54, 1982.

C. A. Nixon, W. R. Marcum, A. W. Weiss, K. M. Steer, R. B. Jackson, M. G. Martin, and

C. Yeager. An Approach to Instrumenting a Full-Scale 61-Pin Hexagonal Fuel Bundle for Flow-Induced Vibration Testing. *NURETH-18*, pages 4926-4933, 2019.

S. Nukiyama. The Maximum and Minimum Values of the Heat Q Transmitted from Metal to Boiling Water Under Atmospheric Pressure. *International Journal of Heat and Mass Transfer*, 1934.

L. J. Peterson and S. M. Bajorek. Experimental Investigation of Minimum Film Boiling Temperature for Vertical Cylinders at Elevated Pressure. *10th International Conference on Nuclear Engineering*. American Society of Medical Engineers, 2002

C. M. Petrie and T. E. Blue. In Situ Reactor Radiation-induced Attenuation in Sapphire Optical Fibers Heated up to 1000°C. *Nuclear Instruments and Methods in Physics Research B*, pages 91-97, 2015.

L. A. Ribeiro, S. F. Quirino, A. O. Toledo, C. L. Barbosa, O. Lisboa, and J. U. Arruda. Spontaneous Raman Scattering in Optical Fiber: Experimental Measurement. *AIP Conference Proceedings*, pages 159-162, 2008.

A. Seshadri and K. Shirvan. Quenching Heat Transfer Analysis of Accident Tolerant Coated Fuel Cladding. *Nuclear Engineering and Design 338*, pages 5-15, 2018.

R. W. Shumway. TRAC-BWR Heat Transfer: Assessment of Tmin. Idaho National Engineering Laboratory, EGG-RST-6781, 1985.

N. E. Todreas and M. S. Kazimi. *Nuclear Systems I Thermal Hydraulic Fundamentals.* Hemisphere Publishing Corporation. 1990.

TRACE V5.840 Theory Manual - Field Equations, Solution Methods, and Physical Models. 2013.

D. Trujillo. *INTEMP - Inverse Heat Transfer Analysis - User's Manual.* TRUCOMP CO.

April 2003.

T. William Wood Jr., B. Blake, T. E. Blue, C. M. Petrie, and D. Hawn. Evaluation of the Performance of Distributed Temperature Measurements with Single-Mode Optical Fiber Using Rayleigh Backscatter up to 1000°C. *IEEE Sensors Journal*, pages 124-128, 2014.

M. Weathered and M. Anderson. Development of Optical Fiber Instrumentation for Use in Sodium Cooled Fast Reactors. *NURETH-16*, pages 1050-1059, 2015.

H. Yeom, H. Jo, G. Johnson, K. Sridharan, and M. Corradini. Transient Pool Boiling Heat Transfer of Oxidized and Roughened Zircaloy-4 Surfaces during Water Quenching. *International Journal of Heat and Mass Transfer 120*, pages 435-446, 2018.

K. Yüksel, M. Wuilpart, V. Moeyaert, and P. Megret. Optical Frequency Domain Reflectometry: A Review. *ICTON 2009: 11th International Conference on Transparent Optical Networks*, 06 2009. doi: 10.1109/ICTON.2009.5185111.

Appendices

Appendix A

Sensitivity Analysis

Due to variation in the surface temperature calculations from the optical fiber and thermocouple measurements during quenching, a simulation was performed where only three optical fiber data locations were used to calculate for three unknown surface heat fluxes. The results of the simulation are shown below. As can be seen, the limited optical fiber data gives similar results to the full-resolution data, which suggests that the difference in results between the thermocouple and fiber calculations are not only explained by the two-dimensional heat conduction. Because of this temperature discrepancy, further analysis will be required before a conclusive statement can be made. It is worthy to mention that this temperature discrepancy only appears after the beginning of the quenching as can be seen in Fig. A.1.

Further analysis also has been done to account for the fiber shifting locations radially, making it closer to one side of the capillary tube inner wall. By performing INTEMP calculations with the fiber data shifted and comparing to the original results, the sensitivity of the results to the location of the fiber can be determined. The results of this test are shown below. The maximum difference in temperature between the original results and the results from the fiber being shifted fully to the inner wall is less than 0.2°C (Fig. A.2). This is due to both the inner radius being very small (0.53 mm) and the thermal resistance of air, which was estimated in this case to be approximately 0.082 $cm^2 \cdot °C/W$.

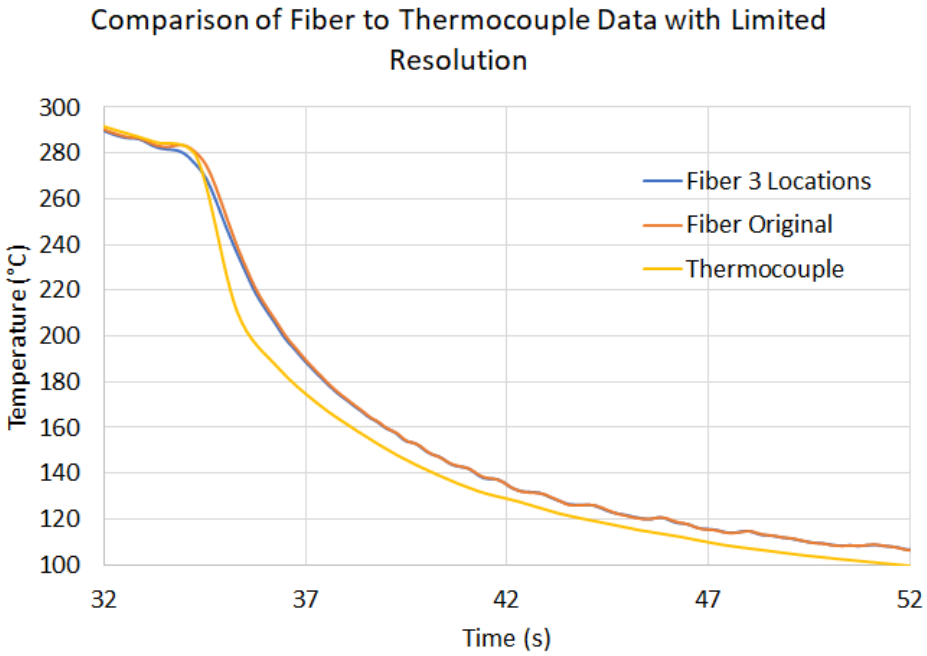

Figure A.1

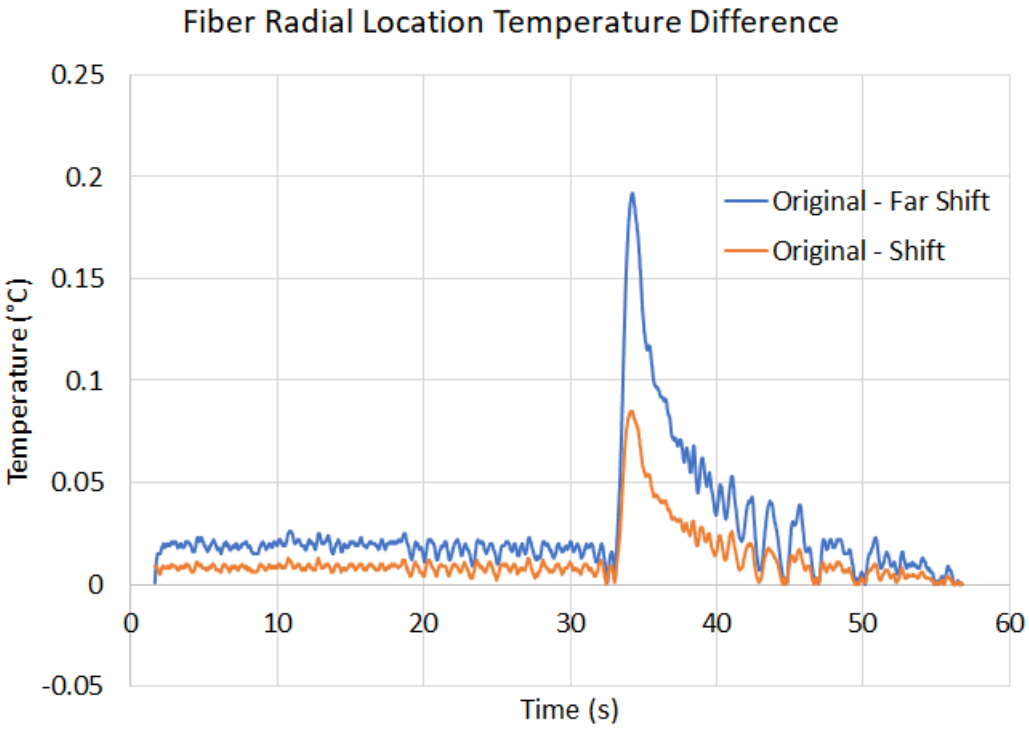

Figure A.2

Appendix B

Original Optical Fiber Temperature Plots for All Tests

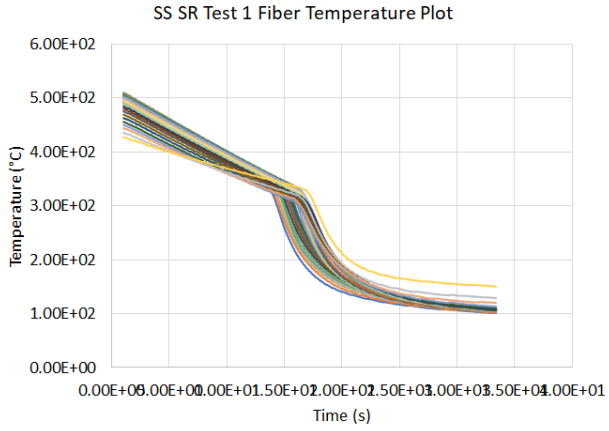

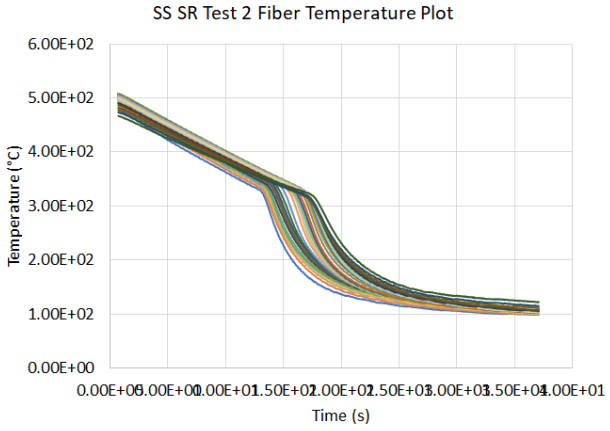

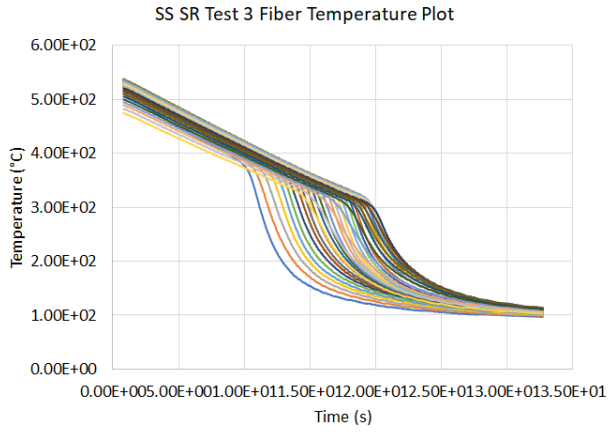

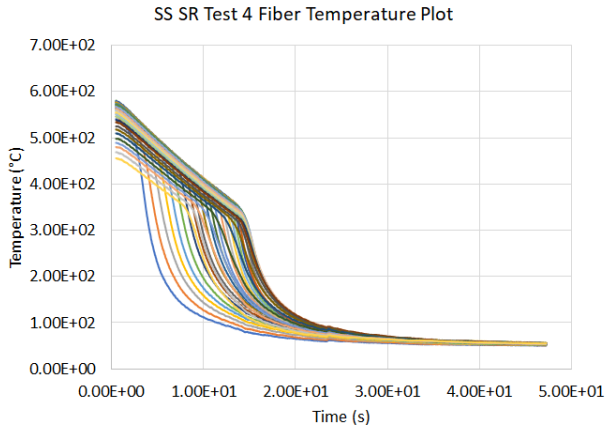

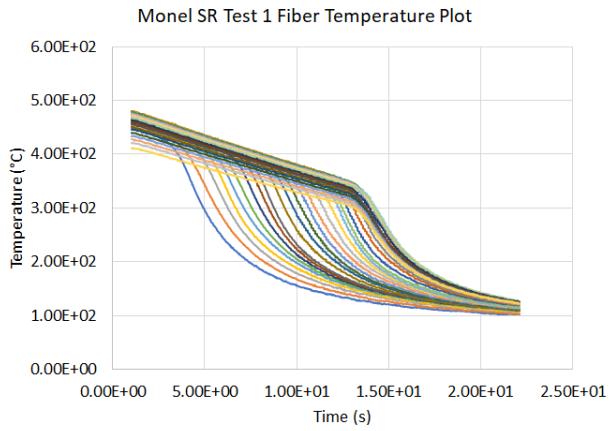
Monel SR Test 1 Fiber Temperature Plot
Temperature (°C)
6.00E+02
5.00E+02
4.00E+02
3.00E+02
2.00E+02
1.00E+02
0.00E+00
0.00E+00
5.00E+00
1.00E+01
1.50E+01
2.00E+01
2.50E+01
Time (s)

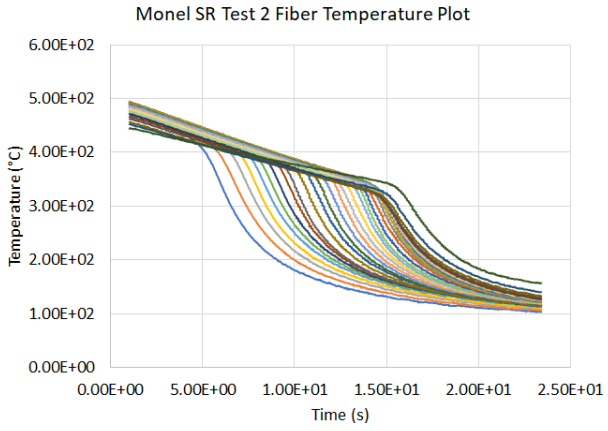
Monel SR Test 2 Fiber Temperature Plot
Temperature (°C)
6.00E+02
5.00E+02
4.00E+02
3.00E+02
2.00E+02
1.00E+02
0.00E+00
0.00E+00
5.00E+00
1.00E+01
1.50E+01
2.00E+01
2.50E+01
Time (s)

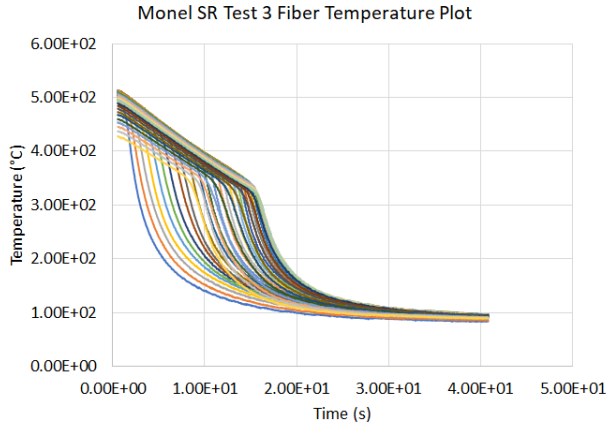
Monel SR Test 3 Fiber Temperature Plot
Temperature (°C)
6.00E+02
5.00E+02
4.00E+02
3.00E+02
2.00E+02
1.00E+02
0.00E+00
0.00E+00
1.00E+01
2.00E+01
3.00E+01
4.00E+01
5.00E+01
Time (s)

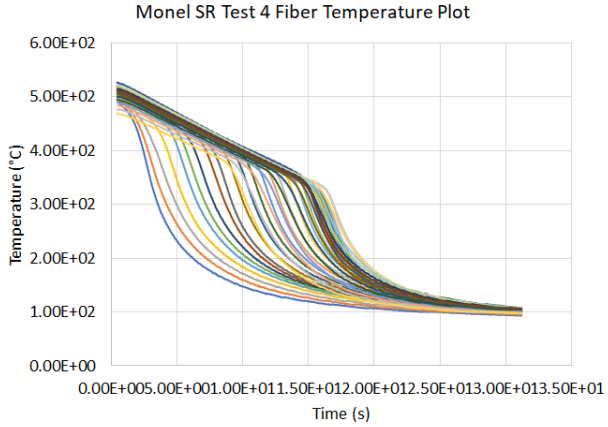
Monel SR Test 4 Fiber Temperature Plot
Temperature (°C)
6.00E+02
5.00E+02
4.00E+02
3.00E+02
2.00E+02
1.00E+02
0.00E+00
0.00E+005.00E+001.00E+011.50E+012.00E+012.50E+013.00E+013.50E+01
Time (s)

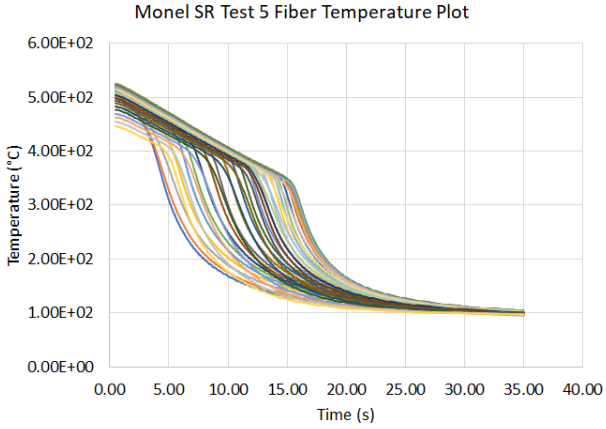
Monel SR Test 5 Fiber Temperature Plot
Temperature (°C)
6.00E+02
5.00E+02
4.00E+02
3.00E+02
2.00E+02
1.00E+02
0.00E+00
0.00
5.00
10.00
15.00
20.00
25.00
30.00
35.00
40.00
Time (s)

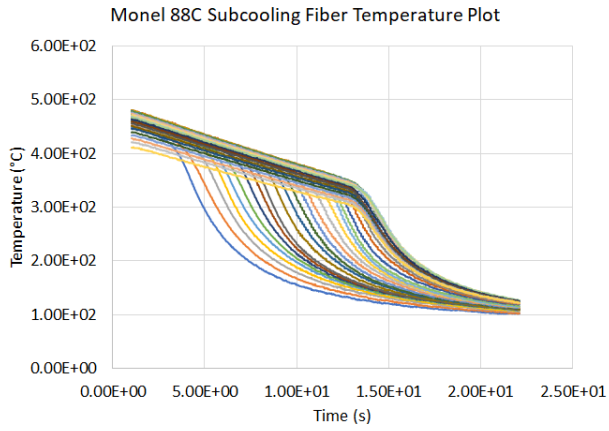
Monel 88C Subcooling Fiber Temperature Plot
Temperature (°C)
6.00E+02
5.00E+02
4.00E+02
3.00E+02
2.00E+02
1.00E+02
0.00E+00
0.00E+00 5.00E+00 1.00E+01 1.50E+01 2.00E+01 2.50E+01
Time (s)

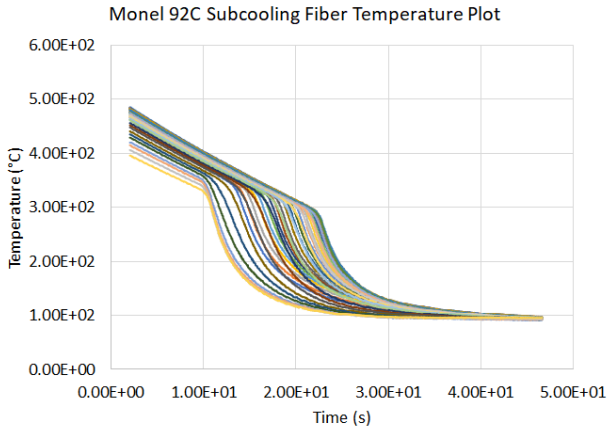
Monel 92C Subcooling Fiber Temperature Plot
Temperature (°C)
6.00E+02
5.00E+02
4.00E+02
3.00E+02
2.00E+02
1.00E+02
0.00E+00
0.00E+00 1.00E+01 2.00E+01 3.00E+01 4.00E+01 5.00E+01
Time (s)

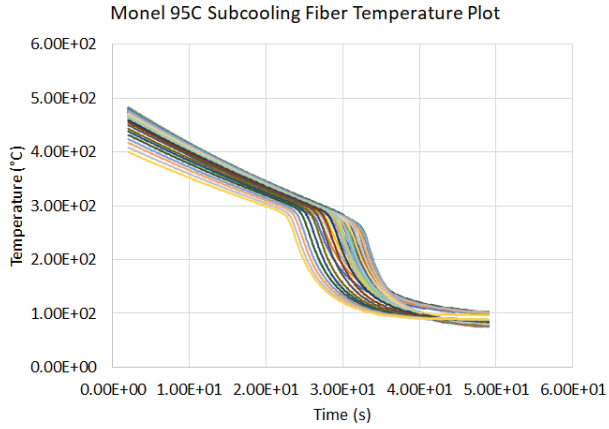
Monel 95C Subcooling Fiber Temperature Plot
Temperature (°C)
6.00E+02
5.00E+02
4.00E+02
3.00E+02
2.00E+02
1.00E+02
0.00E+00
0.00E+00 1.00E+01 2.00E+01 3.00E+01 4.00E+01 5.00E+01 6.00E+01
Time (s)

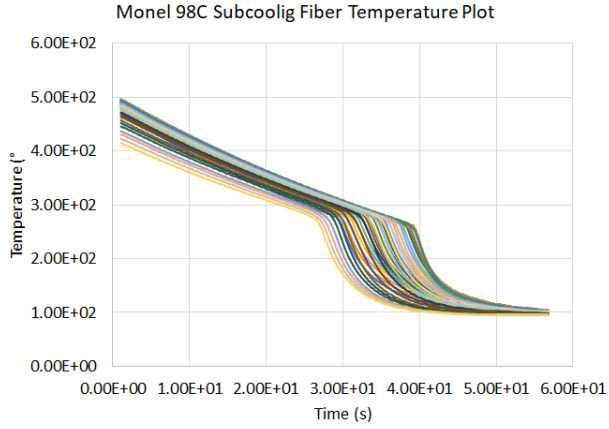
Monel 98C Subcoolig Fiber Temperature Plot
Temperature (°
6.00E+02
5.00E+02
4.00E+02
3.00E+02
2.00E+02
1.00E+02
0.00E+00
0.00E+00 1.00E+01 2.00E+01 3.00E+01 4.00E+01 5.00E+01 6.00E+01
Time (s)

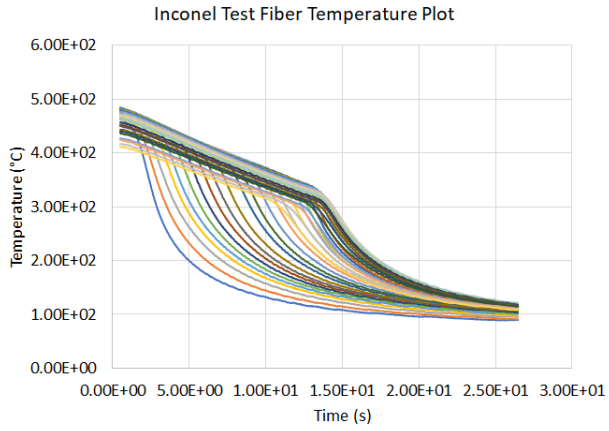
Inconel Test Fiber Temperature Plot
Temperature (°C)
6.00E+02
5.00E+02
4.00E+02
3.00E+02
2.00E+02
1.00E+02
0.00E+00
0.00E+00 5.00E+00 1.00E+01 1.50E+01 2.00E+01 2.50E+01 3.00E+01
Time (s)

Appendix C

Thermocouple Temperature Plots for All Tests

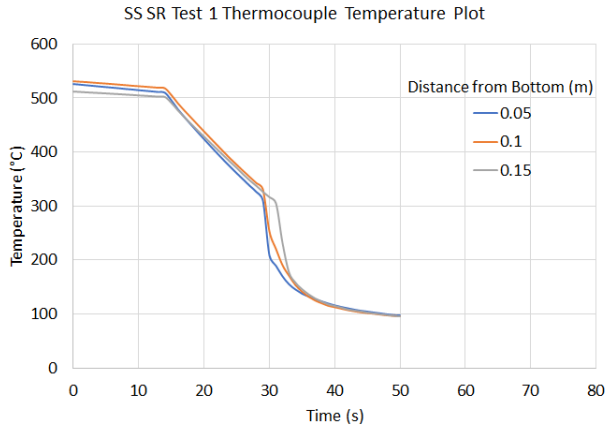

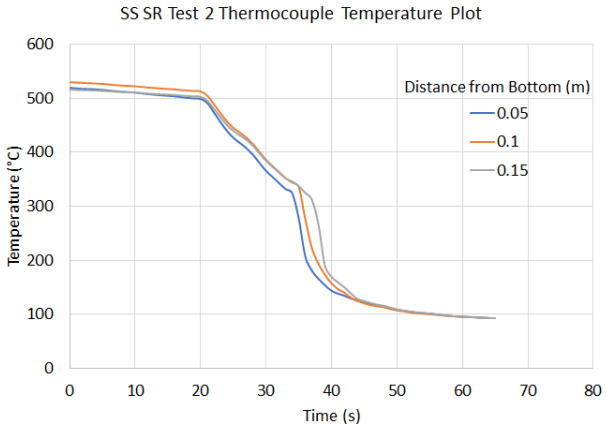

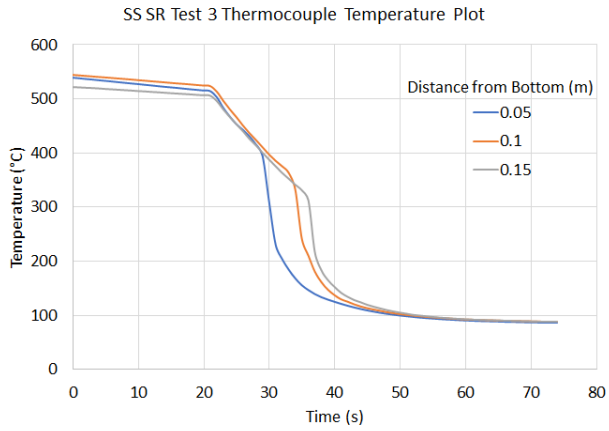

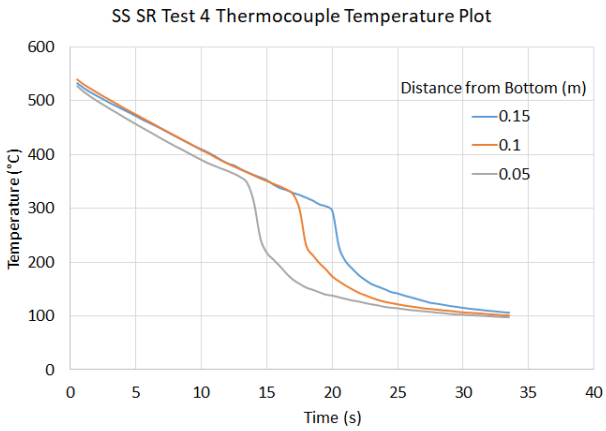

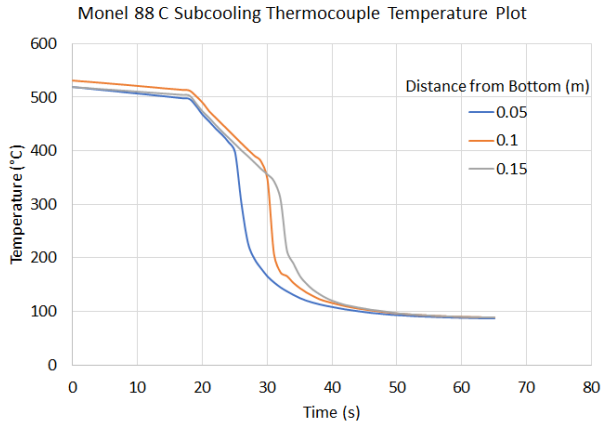
Monel 88 C Subcooling Thermocouple Temperature Plot
Distance from Bottom (m)
0.05
0.1
0.15
Temperature (°C)
Time (s)

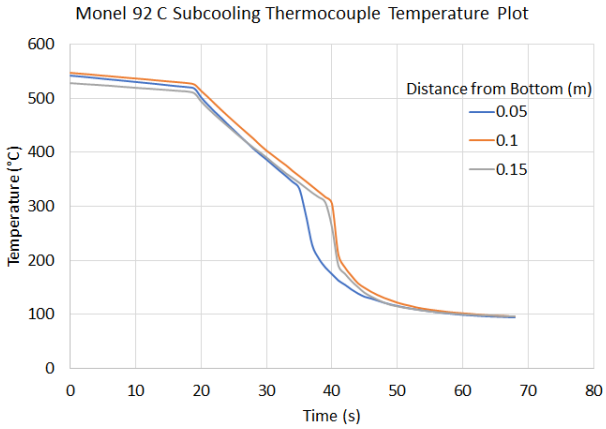
Monel 92 C Subcooling Thermocouple Temperature Plot
Distance from Bottom (m)
0.05
0.1
0.15
Temperature (°C)
Time (s)

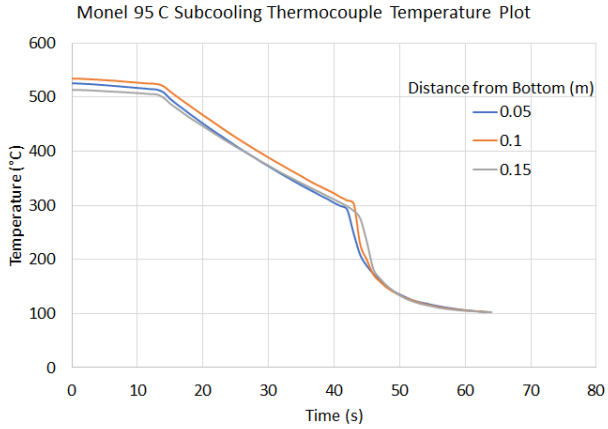
Monel 95 C Subcooling Thermocouple Temperature Plot
Distance from Bottom (m)
0.05
0.1
0.15
Temperature (°C)
Time (s)

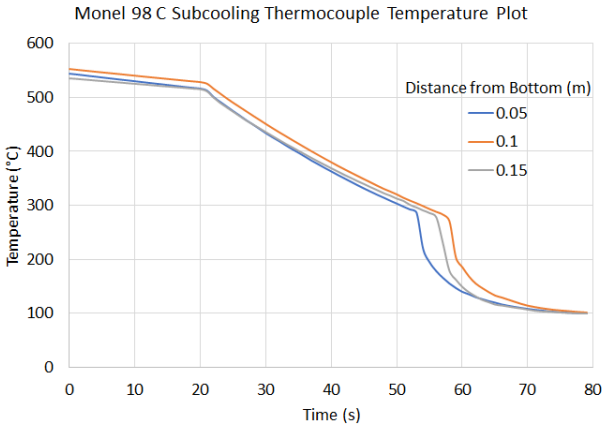
Monel 98 C Subcooling Thermocouple Temperature Plot
Distance from Bottom (m)
0.05
0.1
0.15
Temperature (°C)
Time (s)

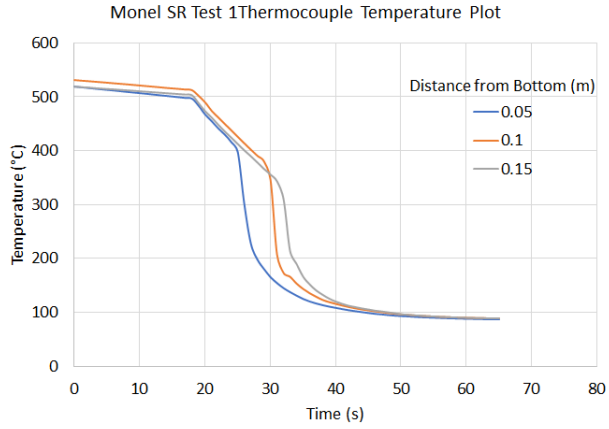
Monel SR Test 1Thermocouple Temperature Plot
Distance from Bottom (m)
0.05
0.1
0.15
Temperature (°C)
Time (s)

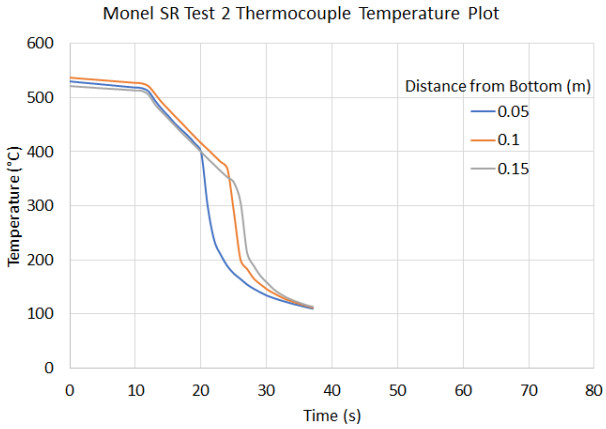
Monel SR Test 2 Thermocouple Temperature Plot
Distance from Bottom (m)
0.05
0.1
0.15
Temperature (°C)
Time (s)

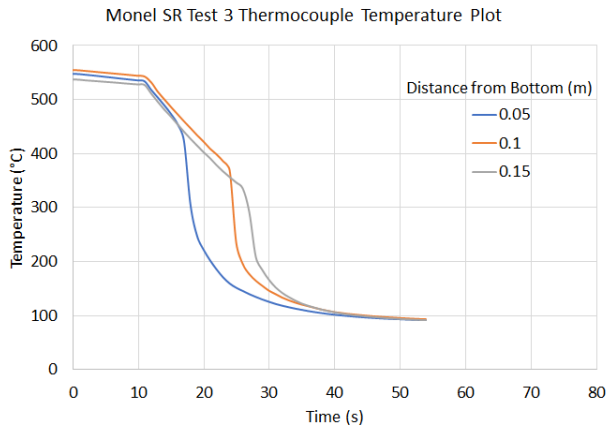
Monel SR Test 3 Thermocouple Temperature Plot
Temperature (°C)
Time (s)
Distance from Bottom (m)
0.05
0.1
0.15

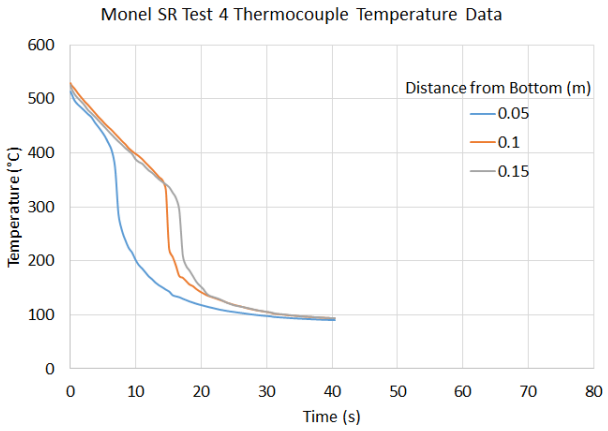
Monel SR Test 4 Thermocouple Temperature Data
Temperature (°C)
Time (s)
Distance from Bottom (m)
0.05
0.1
0.15

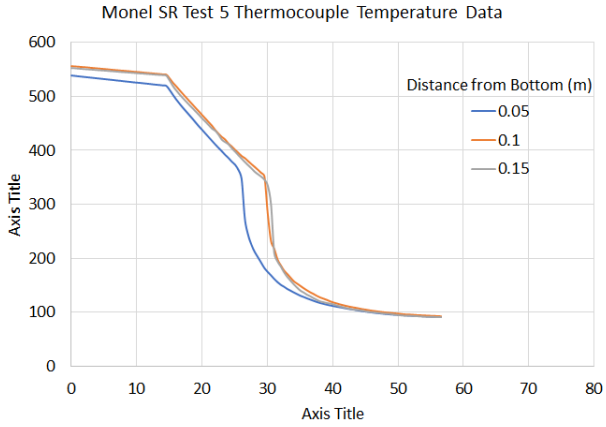
Monel SR Test 5 Thermocouple Temperature Data
Axis Title
Axis Title
Distance from Bottom (m)
0.05
0.1
0.15

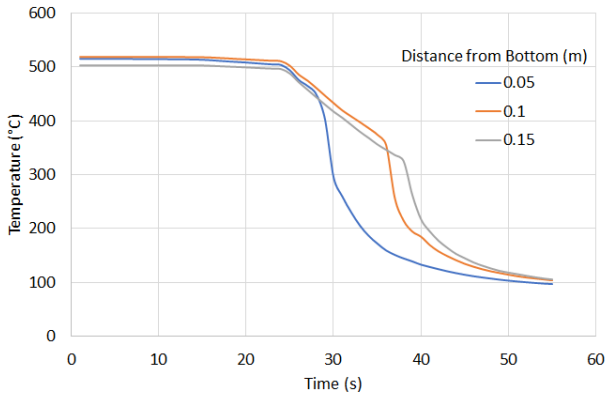
Inconel Test Thermocouple Temperature Plot
Temperature (°C)
Time (s)
Distance from Bottom (m)
0.05
0.1
0.15

Appendix D

Surface Flux Plots for All Tests

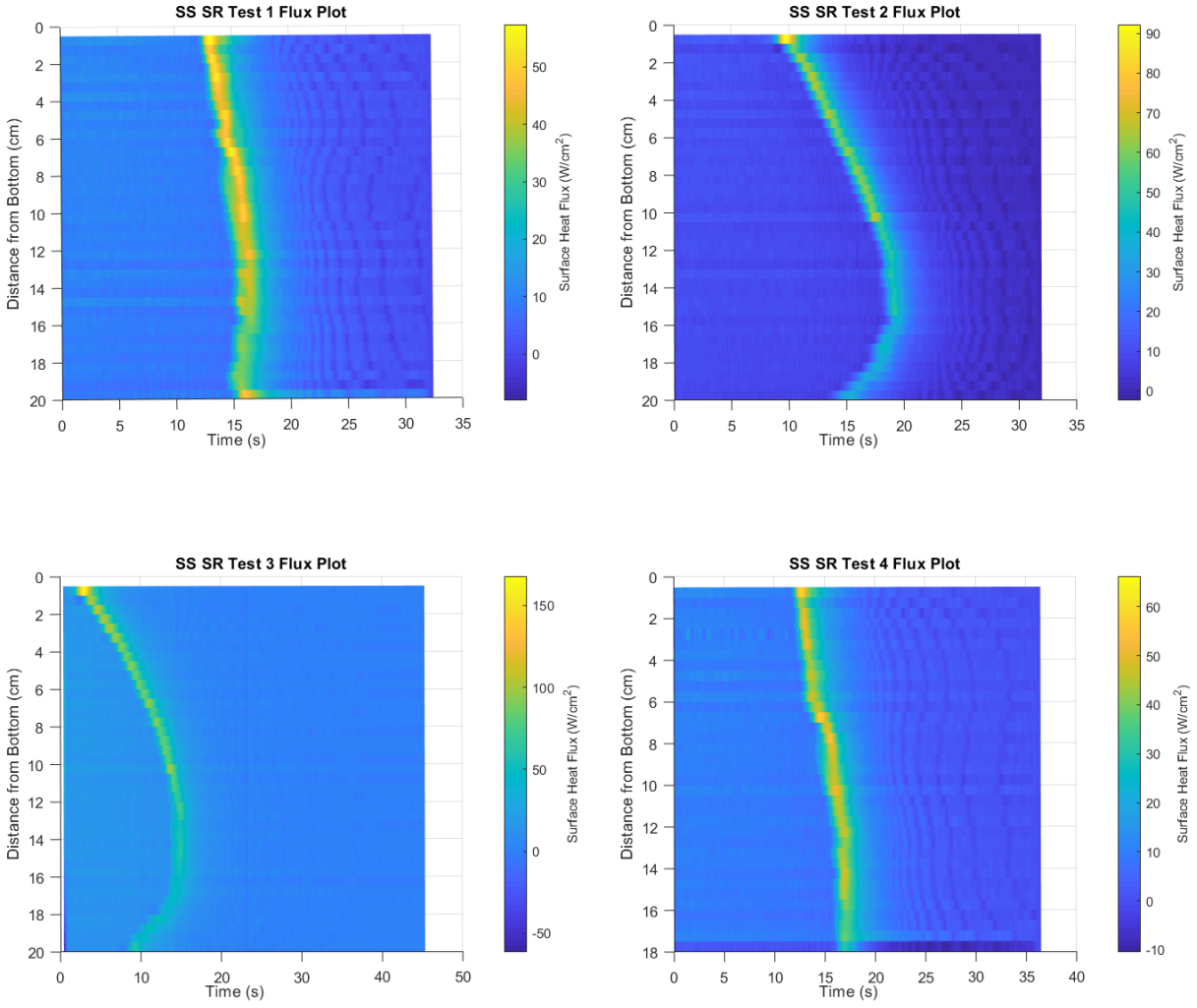

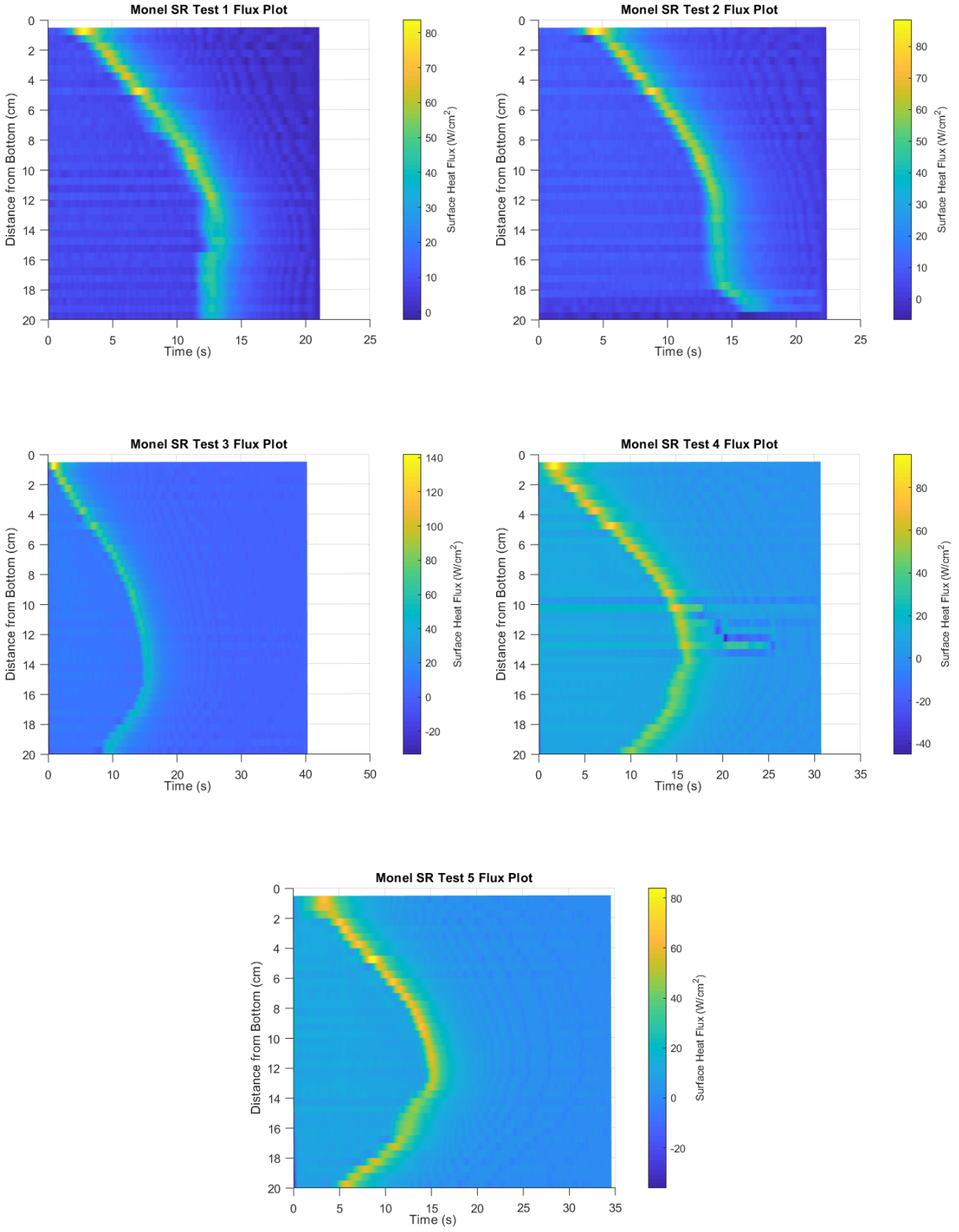
Monel SR Test 1 Flux Plot
Distance from Bottom (cm)
Time (s)
Surface Heat Flux (W/cm^2)
Monel SR Test 2 Flux Plot
Distance from Bottom (cm)
Time (s)
Surface Heat Flux (W/cm^2)
Monel SR Test 3 Flux Plot
Distance from Bottom (cm)
Time (s)
Surface Heat Flux (W/cm^2)
Monel SR Test 4 Flux Plot
Distance from Bottom (cm)
Time (s)
Surface Heat Flux (W/cm^2)
Monel SR Test 5 Flux Plot
Distance from Bottom (cm)
Time (s)
Surface Heat Flux (W/cm^2)

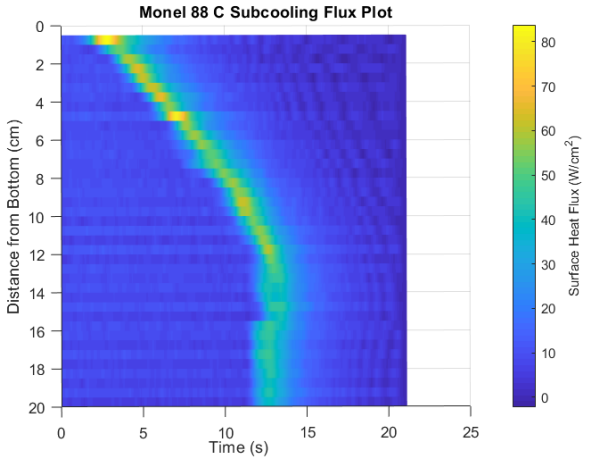
Monel 88 C Subcooling Flux Plot
Distance from Bottom (cm)
Time (s)
Surface Heat Flux (W/cm^2)

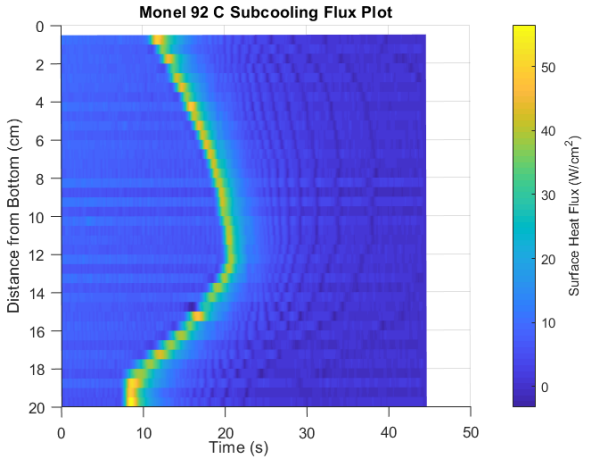
Monel 92 C Subcooling Flux Plot
Distance from Bottom (cm)
Time (s)
Surface Heat Flux (W/cm^2)

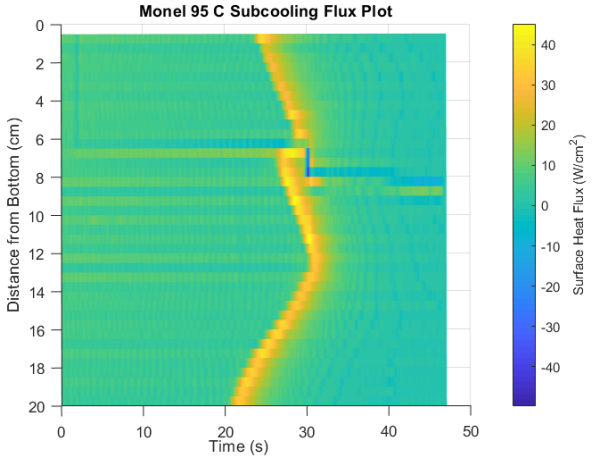
Monel 95 C Subcooling Flux Plot
Distance from Bottom (cm)
Time (s)
Surface Heat Flux (W/cm^2)

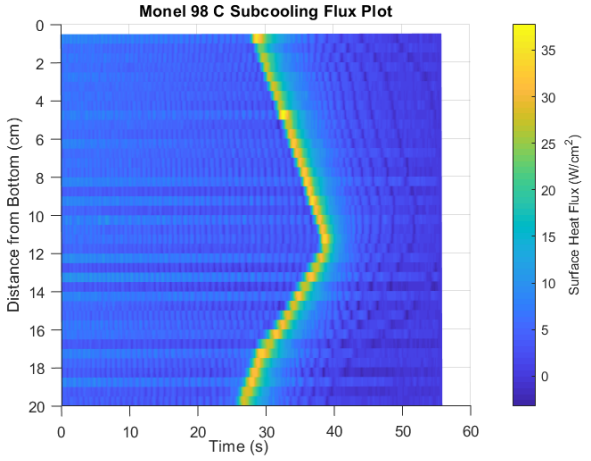
Monel 98 C Subcooling Flux Plot
Distance from Bottom (cm)
Time (s)
Surface Heat Flux (W/cm^2)

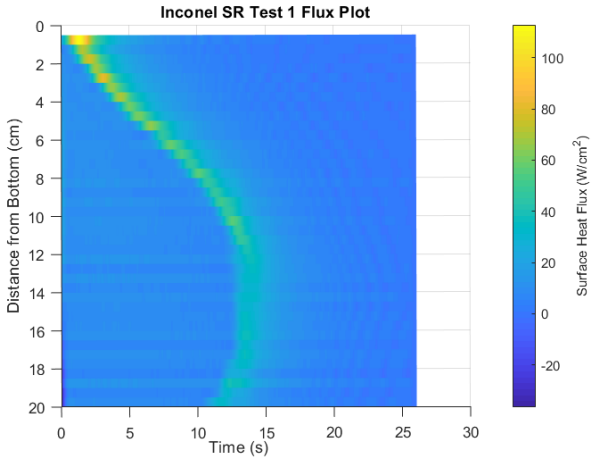
Inconel SR Test 1 Flux Plot
Distance from Bottom (cm)
Time (s)
Surface Heat Flux (W/cm^2)

Appendix E

Surface Temperature Plots for All Tests

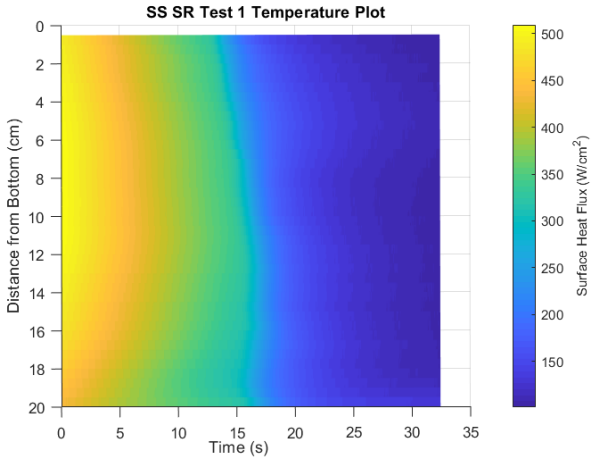

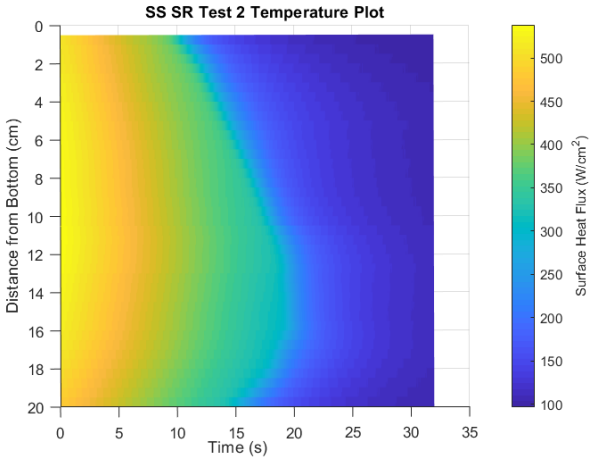

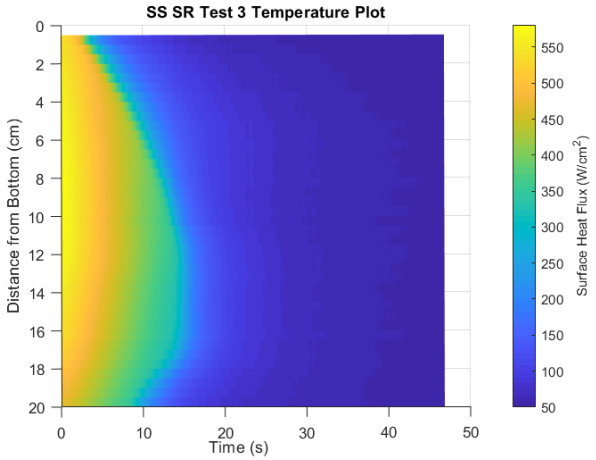

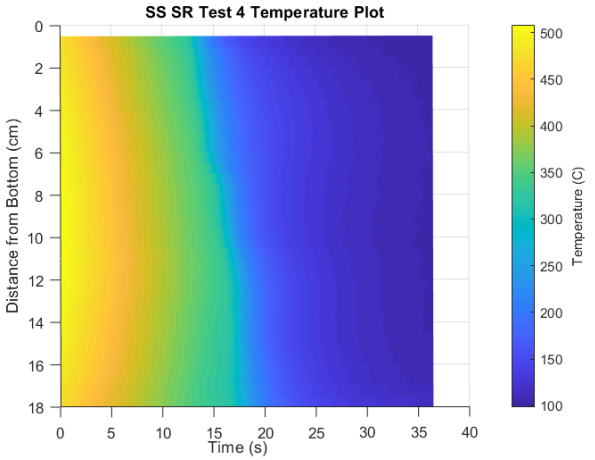

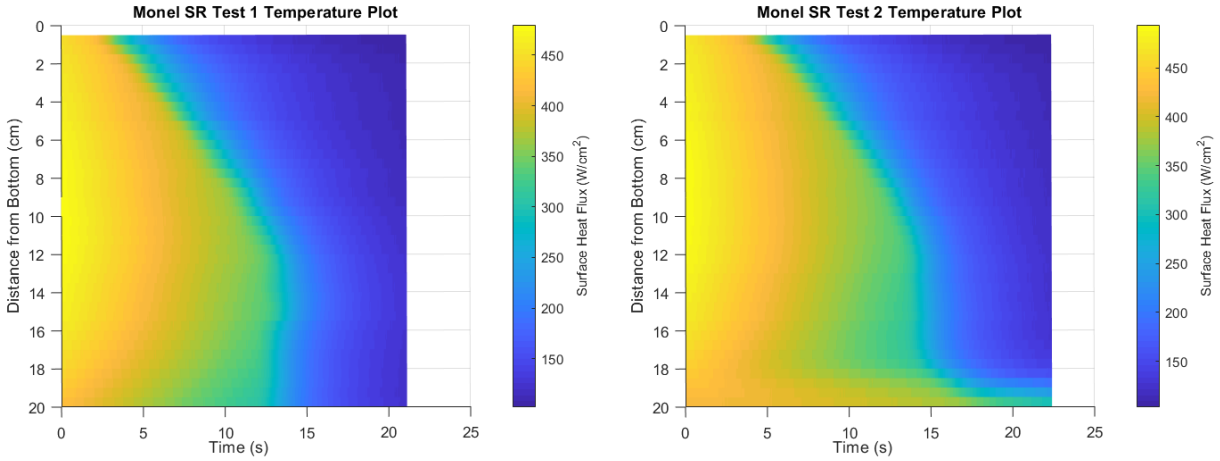
Monel SR Test 1 Temperature Plot
Distance from Bottom (cm)
Time (s)
Surface Heat Flux (W/cm^2)

Monel SR Test 2 Temperature Plot
Distance from Bottom (cm)
Time (s)
Surface Heat Flux (W/cm^2)

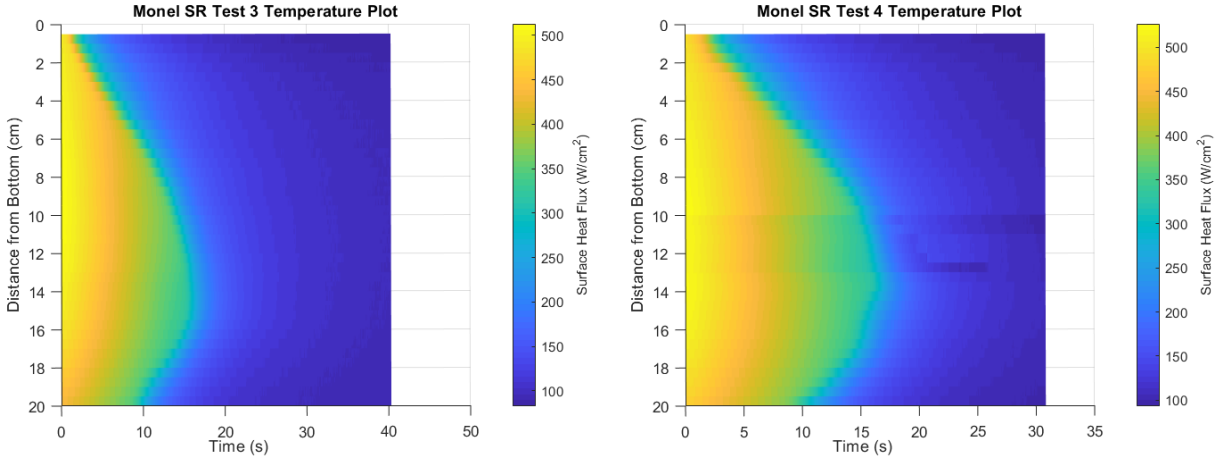
Monel SR Test 3 Temperature Plot
Distance from Bottom (cm)
Time (s)
Surface Heat Flux (W/cm^2)

Monel SR Test 4 Temperature Plot
Distance from Bottom (cm)
Time (s)
Surface Heat Flux (W/cm^2)

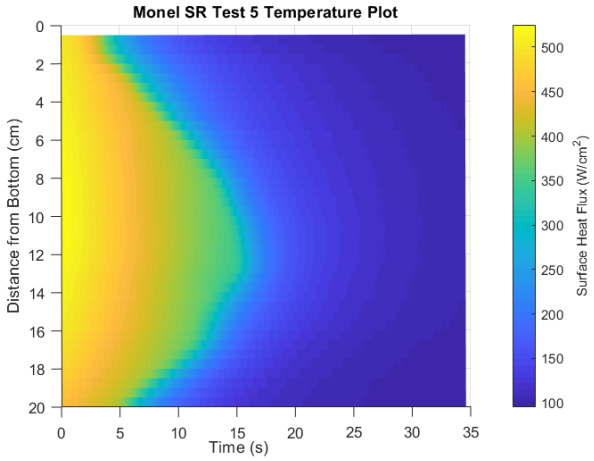
Monel SR Test 5 Temperature Plot
Distance from Bottom (cm)
Time (s)
Surface Heat Flux (W/cm^2)

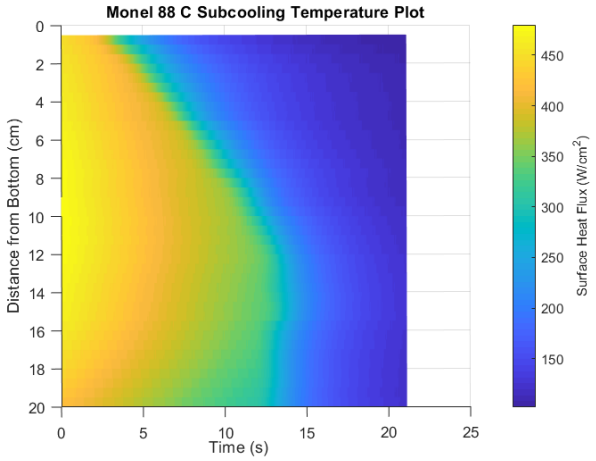
Monel 88 C Subcooling Temperature Plot
Distance from Bottom (cm)
Time (s)
Surface Heat Flux (W/cm^2)

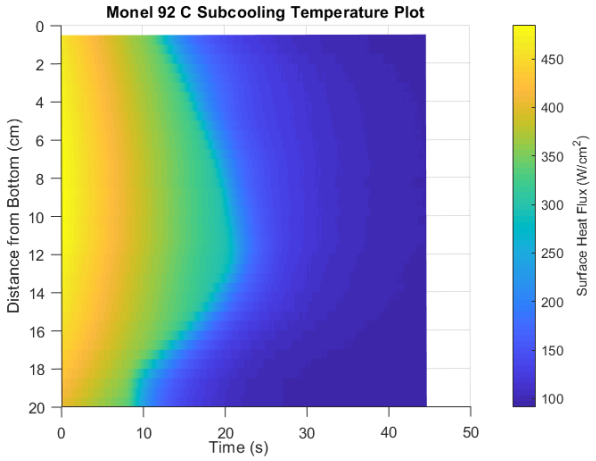
Monel 92 C Subcooling Temperature Plot
Distance from Bottom (cm)
Time (s)
Surface Heat Flux (W/cm^2)

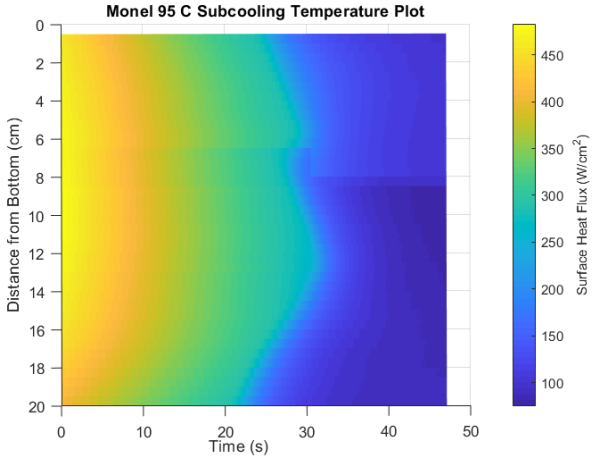
Monel 95 C Subcooling Temperature Plot
Distance from Bottom (cm)
Time (s)
Surface Heat Flux (W/cm^2)

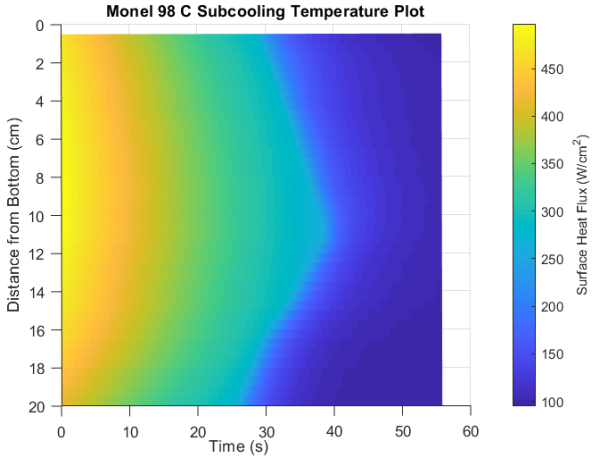
Monel 98 C Subcooling Temperature Plot
Distance from Bottom (cm)
Time (s)
Surface Heat Flux (W/cm^2)

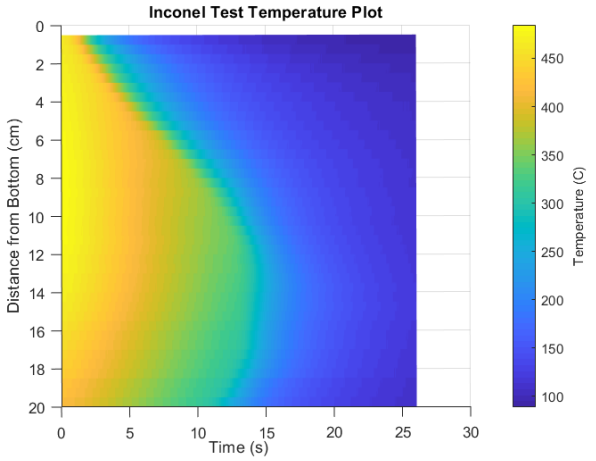
Inconel Test Temperature Plot
Distance from Bottom (cm)
Time (s)
Temperature (C)

Appendix F

Boiling Curves for All Tests

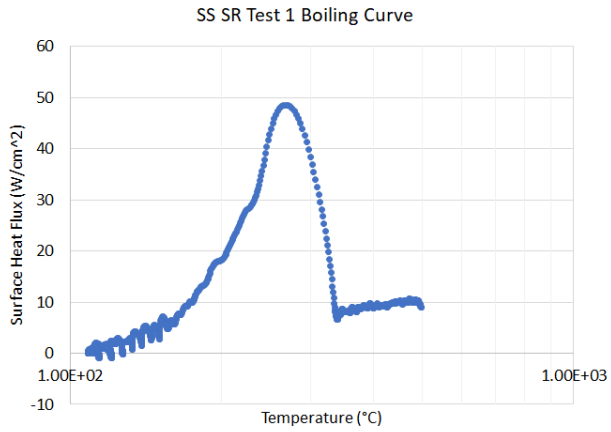

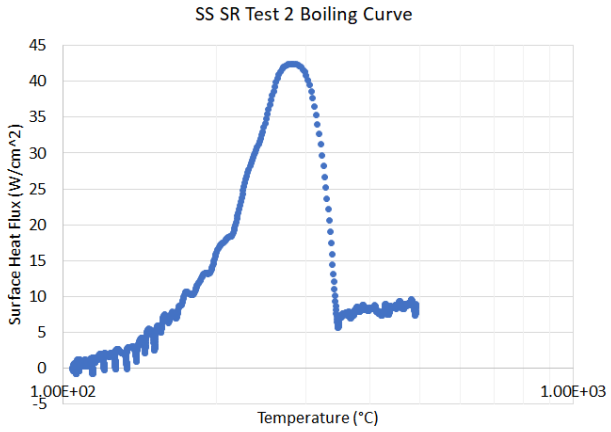

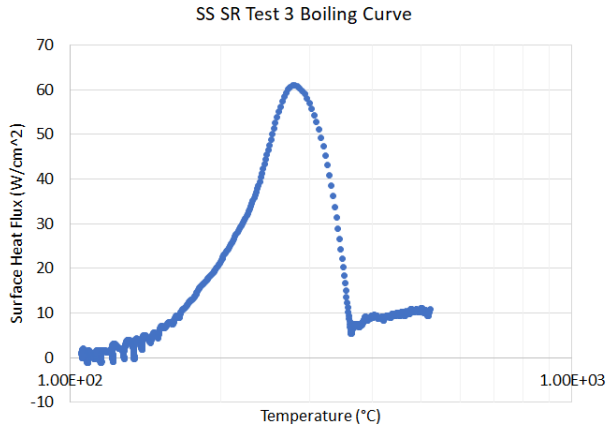

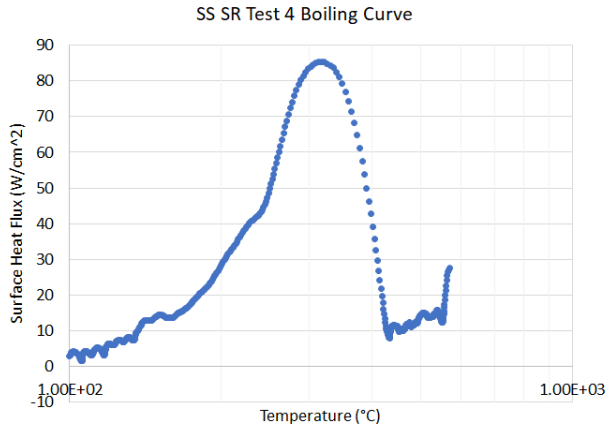

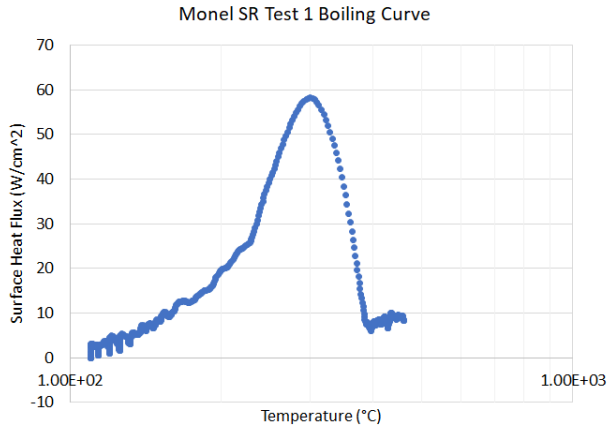
Monel SR Test 1 Boiling Curve
Surface Heat Flux (W/cm^2)
70
60
50
40
30
20
10
0
-10
1.00E+02
1.00E+03
Temperature (°C)

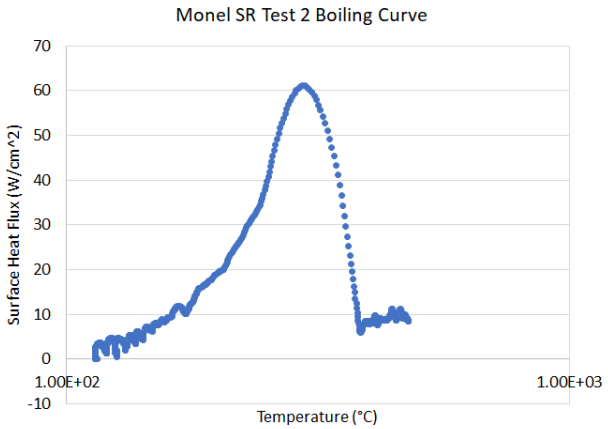
Monel SR Test 2 Boiling Curve
Surface Heat Flux (W/cm^2)
70
60
50
40
30
20
10
0
-10
1.00E+02
1.00E+03
Temperature (°C)

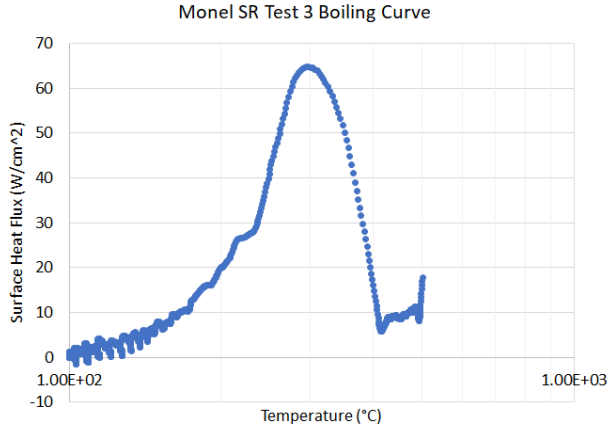
Monel SR Test 3 Boiling Curve
Surface Heat Flux (W/cm^2)
70
60
50
40
30
20
10
0
-10
1.00E+02
1.00E+03
Temperature (°C)

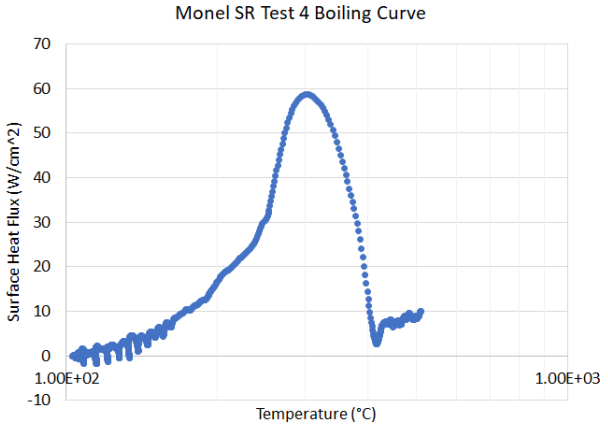
Monel SR Test 4 Boiling Curve
Surface Heat Flux (W/cm^2)
70
60
50
40
30
20
10
0
-10
1.00E+02
1.00E+03
Temperature (°C)

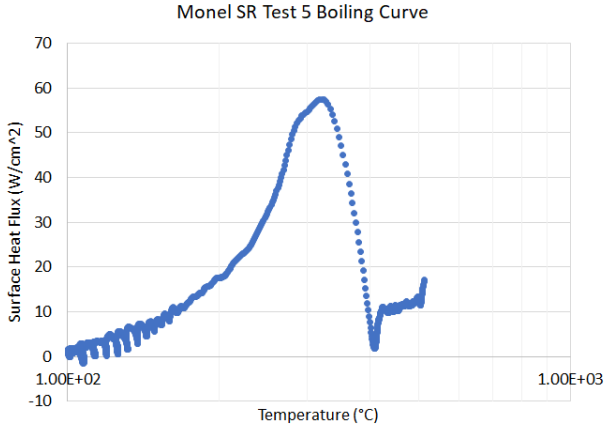
Monel SR Test 5 Boiling Curve
Surface Heat Flux (W/cm^2)
70
60
50
40
30
20
10
0
-10
1.00E+02
1.00E+03
Temperature (°C)

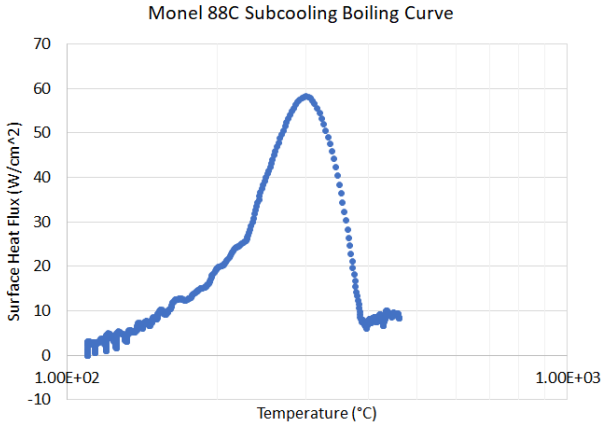
Monel 88C Subcooling Boiling Curve
Surface Heat Flux (W/cm^2)
70
60
50
40
30
20
10
0
-10
1.00E+02
1.00E+03
Temperature (°C)

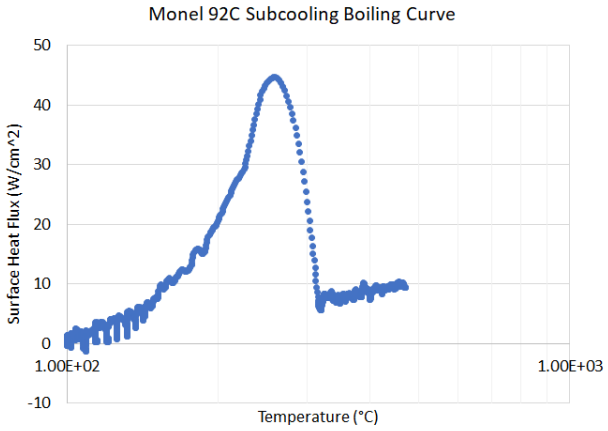
Monel 92C Subcooling Boiling Curve
Surface Heat Flux (W/cm^2)
50
40
30
20
10
0
-10
1.00E+02
1.00E+03
Temperature (°C)

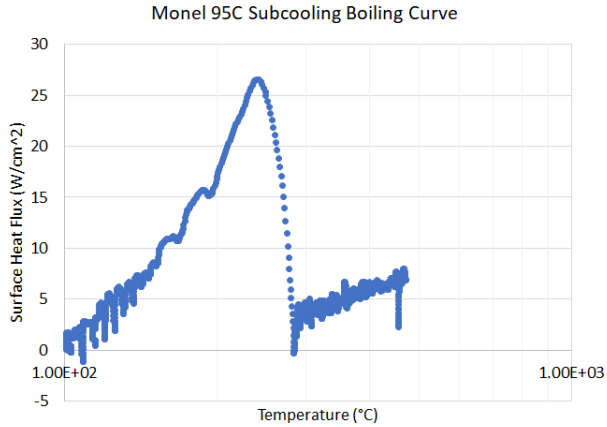
Monel 95C Subcooling Boiling Curve
Surface Heat Flux (W/cm^2)
30
25
20
15
10
5
0
-5
1.00E+02
1.00E+03
Temperature (°C)

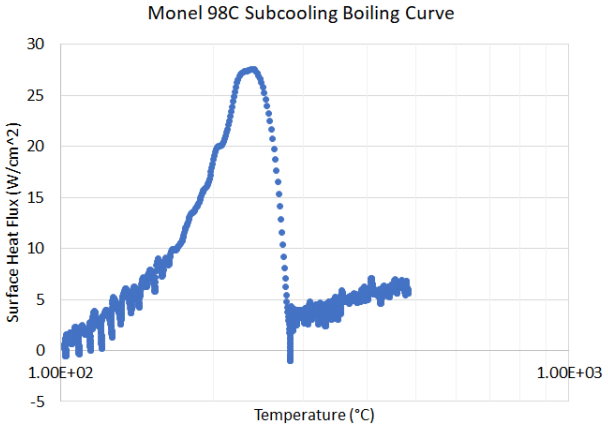
Monel 98C Subcooling Boiling Curve
Surface Heat Flux (W/cm^2)
30
25
20
15
10
5
0
-5
1.00E+02
1.00E+03
Temperature (°C)

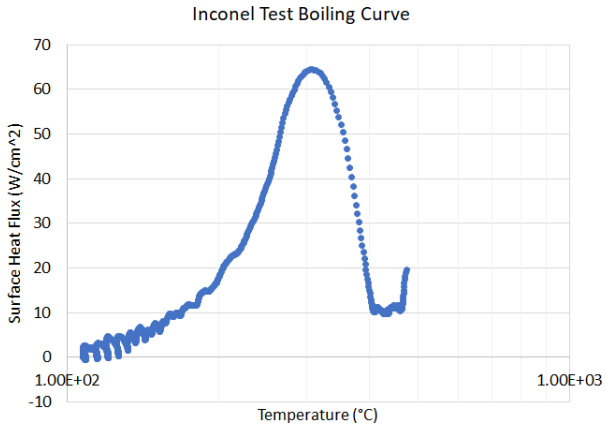
Inconel Test Boiling Curve
Surface Heat Flux (W/cm^2)
70
60
50
40
30
20
10
0
-10
1.00E+02
1.00E+03
Temperature (°C)

Appendix G

Sample Input File for INTEMP

Note: sections in code marked "..." denote that several lines of data have been skipped for the sake of brevity.

```
        ** MONEL K500 QUENCHING
C ** CARD B - CONTROL CARD
C NODES  NEL NMAT IPRIN NG  NZ ISMOO NCONV NFLUX NSTEADY NONITER   IMP  REG}
  1377  1280   4    0   40  40   0     0     0      1       3       0    0
C ** CARD C - TIME CONTROL
C  DELTA  NMAX  INC INCP
   0.032   691   1    1
C ** CARD D - NODE DEFINITION
C N    X       Y      NT  NINC  DX     DY
C GAP (0 - 0.0265 CM)
   1  0.0       0.0    81   1    0.0    0.25
  82  0.01325   0.0   162   1    0.0    0.25
 163  0.0265    0.0   243   1    0.0    0.25
C SS CAPILLARY TUBE (0.0265 - 0.1525 CM)
 244  0.058     0.0   324   1    0.0    0.25
 325  0.0895    0.0   405   1    0.0    0.25
 406  0.121     0.0   486   1    0.0    0.25
```

```
 487  0.1525    0.0   567   1    0.0    0.25
C BORON NITRIDE (0.1525 - 0.386 CM)
 568  0.1992    0.0   648   1    0.0    0.25
 649  0.2459    0.0   729   1    0.0    0.25
 730  0.2926    0.0   810   1    0.0    0.25
 811  0.3393    0.0   891   1    0.0    0.25
 892  0.386     0.0   972   1    0.0    0.25
C CLADDING (0.386 - 0.475 CM)
 973  0.4038    0.0  1053   1    0.0    0.25
1054  0.4216    0.0  1134   1    0.0    0.25
1135  0.4394    0.0  1215   1    0.0    0.25
1216  0.4572    0.0  1296   1    0.0    0.25
1297  0.475     0.0  1377   1    0.0    0.25
 -1
C ** CARD E - ELEMENT DEFINITION
C N  ID     I     J     K     L  NT NINC  TH   NDIM
C GAP ELEMENTS
  1   1     1    82    83     2  80   1   1.     1
 81   1    82   163   164    83  80   1   1.     1
C CAPILLARY TUBE ELEMENTS
161   2   163   244   245   164  80   1   1.     1
241   2   244   325   326   245  80   1   1.     1
321   2   325   406   407   326  80   1   1.     1
401   2   406   487   488   407  80   1   1.     1
C BN ELEMENTS
481   3   487   568   569   488  80   1   1.     1
```

```
561   3   568   649   650   569  80   1   1.     1
641   3   649   730   731   650  80   1   1.     1
721   3   730   811   812   731  80   1   1.     1
801   3   811   892   893   812  80   1   1.     1
C CLADDING ELEMENTS
881   4   892   973   974   893  80   1   1.     1
961   4   973  1054  1055   974  80   1   1.     1
1041  4  1054  1135  1136  1055  80   1   1.     1
1121  4  1135  1216  1217  1136  80   1   1.     1
1201  4  1216  1297  1298  1217  80   1   1.     1
 -1
C ** CARD F - INITIAL TEMPERATURES
C  N  T        NT    NINC   DT  IFIX
   1  550.00  1377  1
 -1
C ** CARD F2 - KNOWN HEAT FLUX DATA
C
C -1
C TABLE ID AND DESCRIPTION
C 1
C KNOWN HEAT FLUX VERSUS TIME
C TIME FLUX TIME FLUX TIME FLUX
C
C -1
C999
C END OF ALL TABLES DENOTED BY 999
```

```
C           K(W/CM.C)       CP(W.S/C)  RHO(KG/CM^3)  TEMP(C)
C ** CARD G - MATERIAL DATA
C      KX          KY            CP           RHO          TEMP
C GAP
    1  3.023E-5   3.023E-5     1009         1E-6          80.3
    1  3.825E-5   3.825E-5     1026      7.45E-7         200.0
    1  5.024E-5   5.024E-5     1068      5.23E-7         400.0
    1  6.114E-5   6.114E-5     1115     4.043E-7         600.0
C SS CAPILLARY TUBE
    2  0.1562     0.1562        486      7.92E-3          80.3
    2  0.1714     0.1714        528      7.88E-3         200.0
    2  0.1968     0.1968        560      7.80E-3         400.0
    2  0.2222     0.2222        580      7.71E-3         600.0
C BORON NITRIDE
    3  0.2503     0.2503        900     2.002E-3          80.3
    3  0.2473     0.2473       1088     2.002E-3         200.0
    3  0.2424     0.2424       1350     2.002E-3         400.0
    3  0.2375     0.2375       1560     2.002E-3         600.0
C MONEL CLADDING
    4  0.1961     0.1961        448     8.453E-3          93.3
    4  0.2250     0.2250        477     8.453E-3         204.4
    4  0.2856     0.2856        502     8.453E-3         426.7
    4  0.3461     0.3461        553     8.453E-3         648.9
 -1
C ** CARH H - LUMPED CAPACITANCE DATA (REQUIRES A -1)
 -1
```

```
C ** CARD H1 - THERMAL RESISTANCE DATA (REQUIRES A -1)
 -1
C ** CARD I - UNKNOWN HEAT FLUX DATA
C FLUX     I    J  K  L  NT  NINC  NDIM   AREA
   1    1297 1298  0  0   2   1      1    1.0
   2    1299 1300  0  0   2   1      1    1.0
   3    1301 1302  0  0   2   1      1    1.0
   4    1303 1304  0  0   2   1      1    1.0
   5    1305 1306  0  0   2   1      1    1.0
   6    1307 1308  0  0   2   1      1    1.0
...
  33    1361 1362  0  0   2   1      1    1.0
  34    1363 1364  0  0   2   1      1    1.0
  35    1365 1366  0  0   2   1      1    1.0
  36    1367 1368  0  0   2   1      1    1.0
  37    1369 1370  0  0   2   1      1    1.0
  38    1371 1372  0  0   2   1      1    1.0
  39    1373 1374  0  0   2   1      1    1.0
  40    1375 1376  0  0   2   1      1    1.0
 -1
c ** CARD J - DATA WEIGHTING MATRIX A
C  I  J  FACTOR
   1  1  1.0
   2  2  1.0
   3  3  1.0
   4  4  1.0
```

```
   5  5  1.0
   6  6  1.0
...
  33 33  1.0
  34 34  1.0
  35 35  1.0
  36 36  1.0
  37 37  1.0
  38 38  1.0
  39 39  1.0
  40 40  1.0
 -1
C ** CARD J1 - FLUX WEIGHTING MATRIX B
C  I  J  FACTOR
   1  1  1.E-2
   2  2  1.E-2
   3  3  1.E-2
   4  4  1.E-2
   5  5  1.E-2
   6  6  1.E-2
...
  33 33  1.E-2
  34 34  1.E-2
  35 35  1.E-2
  36 36  1.E-2
  37 37  1.E-2
```

```
  38 38  1.E-2
  39 39  1.E-2
  40 40  1.E-2
 -1
C ** CARD KA - TEMPERATURE DATA LOCATIONS
C   1   2   3   4   5   6   7   8   9  10
    2   4   6   8  10  12  14  16  18  20
C  11  12  13  14  15  16  17  18  19  20
   22  24  26  28  30  32  34  36  38  40
C  21  22  23  24  25  26  27  28  29  30
   42  44  46  48  50  52  54  56  58  60
C  31  32  33  34  35  36  37  38  39  40
   62  64  66  68  70  72  74  76  78  80
C ** CARD KB - TEMPERATURE DATA
C DATA TAKEN FROM MONEL QUENCHING EXPERIMENT (FIBERS - CELSIUS)
1   455.1399058 457.6535048 461.8587528 463.5524647 466.5671336
    467.8887809 471.5539532 474.0410923 474.1141791 476.8157803
    479.5122324 479.8762178 481.3311971 483.4381573 484.5266686
    484.6717361 484.6717361 484.5266686 485.3243434 485.3968354
    483.9462398 485.1068434 483.0025044 482.784625 481.5493105
    479.8034284 477.4721515 475.2830651 473.3100209 471.7735767
    468.0355597 464.4354142 459.8681674 454.1778093 450.8431898
    443.7074913 438.8594956 431.3755682 425.0656258 414.9561576
2   454.7699348 458.0228259 462.2271061 464.5089707 467.3749432
    468.5491733 471.7735767 474.0410923 473.6024937 475.8671511
    479.6578381 480.4583947 481.5493105 484.8167878 484.5992043
```

```
    484.5266686 484.7442639 484.4541288 484.8893077 486.0490835
    484.7442639 484.6717361 483.1477378 484.0188073 480.7493907
    480.167337 477.982451 476.7428314 473.9680017 471.5539532
    468.6225324 463.5524647 460.7531791 455.3618487 450.1754742
    443.4840287 438.5607281 431.300575 424.7646242 415.1830716
3   455.8056448 457.2102089 461.5640085 465.0237687 467.1546739
    467.8887809 470.8216391 474.3334175 474.0410923 476.6698786
    479.2209752 480.167337 480.7493907 484.5266686 484.8167878
    484.6717361 484.8167878 485.1068434 485.7592355 485.7592355
    484.5992043 485.3243434 482.4214143 483.0025044 480.82213
    480.0217851 476.8157803 475.5021253 473.0174893 472.7980521
    467.5217717 463.773249 460.7531791 453.6595265 450.9173643
    443.1115281 438.8594956 430.6254994 424.4635747 415.4855821
4   455.0659182 457.9489684 461.9324304 464.2882907 466.7140399
    468.3290745 470.8948868 474.7717943 474.1872623 476.8887255
    479.1481513 479.7306352 481.6947001 483.2929554 484.8893077
    484.1639303 484.8167878 485.0343355 485.6142874 485.4693234
    484.1639303 484.5992043 483.6559306 483.5107523 480.8948655
    480.167337 477.5450628 475.8671511 472.7980521 472.1395429
    467.3749432 463.773249 460.7531791 454.1778093 451.2881877
    443.6330069 438.187199 431.075577 424.2377563 414.9561576
...
688 101.5472672 102.7820504 106.4722072 107.187286 108.3093817
    108.9206129 110.0397047 110.8523761 110.2429682 111.0553848
    112.0694762 111.8667847 113.1831504 114.5978017 115.707163
    114.7996442 115.5056012 116.613422 118.7231567 121.1260036
```

120.7261384 122.0248137 122.324145 124.9126841 124.6145229
126.5997377 126.4014831 126.6988428 126.5006178 127.3921653
125.0120414 123.5201147 124.6145229 122.324145 123.2213252
121.9250064 122.5236237 122.4238919 123.9182907 123.2213252
689 102.2678466 102.0620495 106.3699882 108.2074536 109.2260118
108.9206129 109.6329862 110.7508479 109.9380491 111.3597787
112.6771714 111.7654151 113.284299 115.2031418 115.0014242
115.3039772 114.5978017 115.707163 119.124242 120.7261384
121.825184 121.2259319 121.825184 125.7071259 125.310024
126.4014831 126.5006178 127.0951155 126.5006178 127.2931634
126.4014831 122.9224005 124.1172889 122.6233405 123.5201147
121.825184 122.0248137 121.6254939 123.2213252 122.5236237
690 101.8561863 102.5764184 106.3699882 107.5955466 108.6150696
109.6329862 110.4461679 111.25833 109.0224286 110.0397047
112.4746695 111.9681383 113.688736 113.4865489 115.404797
114.6987308 115.404797 116.4121397 118.92373 120.9261014
121.3258451 121.825184 122.0248137 124.1172889 125.1113838
126.4014831 127.4911524 127.3921653 126.4014831 127.3921653
125.310024 123.7192327 123.8187692 122.7230422 123.0220571
123.0220571 122.4238919 120.9261014 122.9224005 121.9250064
691 101.3412383 103.7065791 105.3469053 107.79958 108.8187812
108.8187812 109.9380491 110.7508479 110.1413444 111.0553848
112.7783987 112.2721044 113.3854318 113.5876503 115.2031418
115.1022908 115.2031418 115.8079206 118.321826 120.5261147
120.5261147 121.0260601 121.9250064 124.813312 124.5151059
125.7071259 126.1039904 127.1941469 126.4014831 126.7979331

```
    126.3023337 123.3209367 123.5201147 122.6233405 122.5236237
    122.0248137 122.4238919 121.825184 121.825184 123.0220571
END
```